THESIS ON NATURAL AND EXACT SCIENCES B187

Application of Modulation Spectroscopy Methods in Photovoltaic Materials Research

TAAVI RAADIK

TUT PRESS

TALLINN UNIVERSITY OF TECHNOLOGY
Faculty of Chemical and Materials Technology
Department of Material Science
Chair of Semiconductor Materials Technology

Dissertation was accepted for the defence of the degree of Doctor of Philosophy in Natural and Exact Sciences on May 26, 2015

Supervisors: Professor Jüri Krustok, Department of Materials Science, Tallinn University of Technology, Estonia

Dr Maarja Grossberg, Senior Research Scientist, Department of Materials Science, Tallinn University of Technology, Estonia

Opponents: Dr. Sergiu Levcenco, Helmholtz-Zentrum Berlin, Department Complex Compound Semiconductor Materials for Photovoltaics, Berlin, Germany

Dr. Raivo Jaaniso, Institute of Physics, University of Tartu, Estonia

Defense: June 30, 2015, at 11.00
Lecture hall: VIa-201
Tallinn University of Technology,
Ehitajate tee 5, Tallinn

Declaration:
Hereby I declare that this doctoral thesis, my original investigation and achievement, submitted for the doctoral degree at Tallinn University of Technology, has not been submitted for any academic degree.

Taavi Raadik

ISSN 1406-4723
ISBN 978-9949-23-799-9 (publication)
ISBN 978-9949-23-800-2 (PDF)

LOODUS- JA TÄPPISTEADUSED B187

Modulatsioonspektroskoopia meetodite rakendamine päikeseenergeetika materjalide uurimiseks

TAAVI RAADIK

TTÜ
KIRJASTUS

TABLE OF CONTEST

LIST OF PUBLICATIONS

The present doctoral thesis is based on the following papers, which are referred to in the text by their Roman numerals **I-V:**

I **T. Raadik**, J. Krustok, M.V. Yakushev. Photoreflectance study of $AgGaTe_2$ single crystals. *Physica B*: *Physics of Condensed Matter,* 406 (2011) 418-420.

II **T. Raadik**, J. Krustok, R. Josepson, J. Hiie, T. Potlog, N. Spalatu. Temperature dependent electroreflectance study of CdTe solar cells. *Thin Solid Films,* 535 (2013) 184-187.

III **T.Raadik**, M. Grossberg, J. Raudoja, J. Krustok. Temperature dependent photoreflectance study of SnS crystals. *Journal of Physics and Chemistry of Solids*, 74 (12) (2013) 1683-1685.

IV M.V. Yakushev, P. Maiello, **T. Raadik**, M.J Shaw, P.R. Edwards, G. Zoppi, J. Krustok, A.V. Mudryi, I. Forbes and R.W. Martin. Electronic and Structural Properties of Cu_3BiS_3 Thin Films. *Thin Solid Film,* 562 (2014) 195-199.

V J. Krustok, **T. Raadik**, M. Grossberg, S. Giraldo, M. Neuschitzer, S. López-Marino, E. Saucedo. Temperature dependent electroreflectance study of $Cu_2ZnSnSe_4$ solar cells. *Materials Science in Semiconductor Processing,* (in press).

In Appendix A, copies of the following papers are included.

AUTHOR´S OWN CONTRIBUTION

The contribution of the author to the papers included in the thesis is as follows:

I Characterization of $AgGaTe_2$ crystals by Raman and photoreflectance spectroscopy: analysis of results and major part of writing.

II Characterization of CdTe solar cells by electroreflectance spectroscopy: analysis of results and major part of writing.

III Characterization of SnS crystals by Raman, photoluminescence and photoreflectance spectroscopy: analysis of results and major part of writing.

IV Characterization of Cu_3BiS_3 thin films by photoreflectance spectroscopy: analysis of results.

V Characterization of $Cu_2ZnSnSe_4$ solar cells by electroreflectance spectroscopy: analysis of results.

LIST OF ABBREVIATIONS AND SYMBOLS

AC	Alternative current
AGT	$AgGaTe_2$
CER	Contactless electroreflectance
CP	Critical point
C.B. min	Conduction band minimum
CZTSe	$Cu_2ZnSnSe_4$
DC	Direct current
E_g	Bandgap energy
E_F	Fermi level
E_{Fn}	Quasi-Fermi level for electron
E_{Fp}	Quasi-Fermi level for holes
ER	Electroreflectance
FKO	Franz-Keldysh oscillations
FF	Fill factor
IR	Infra-red
I-V	Current-voltage characteristics
J_{SC}	Short circuit current
MS	Modulation spectroscopy
PR	Photoreflectance
PV	Photovoltaic
Si	Silicon
V.B. max	Valence band maximum
V_{OC}	Open circuit voltage
XRD	X-ray diffraction

INTRODUCTION

Solar cell is an optoelectronic device that converts solar radiation directly to electricity. Solar cells are based on the photoelectric effect that was discovered by Alexandre Edmond Becquerel in 1839. In 1905, Albert Einstein explained the mechanism behind the photoelectric effect and received the Nobel Prize in physics for the work. If a photon of light that has higher energy than the binding energy of an electron is absorbed in material, it could eject electrons from the material (photoelectric effect) or make them free to move in a semiconductor (internal photovoltaic effect).

Photovoltaic solar cell operates by exploiting the photovoltaic effect, in which separated photo-generated charge carriers are carried out through an external circuit. As a semiconductor absorbs a photon, an electron-hole pair can be generated, which normally recombine and generate a small amount of heat or photoluminescence radiation. However, in a PV solar cell, a built in electric field is used to separate the electron-hole pair before recombination. This is achieved by formation of a semiconductor p-n junction, as illustrated in Fig. 1 a). The p-n junction is formed between the n-type semiconductor buffer layer and the p-type semiconductor absorber layer, which works as a light absorber in solar cells. The band structure at the junction bends in order to align the Fermi level energies E_F of the different layers and generates an electric field in this region. Now, when an absorbed photon generates an electron-hole pair, these charge carriers will be separated by the field and run outside of the device into an external circuit shown in Fig. 1 b) [1]. At the same time, two quasi-Fermi levels are created, E_{Fp} and E_{Fn} in the p-type and n-type region, respectively. The gap between the quasi-Fermi levels eV_f, determines the solar cell open circuit voltage. With the higher light intensity, more quasi-Fermi levels split and V_{OC} increases.

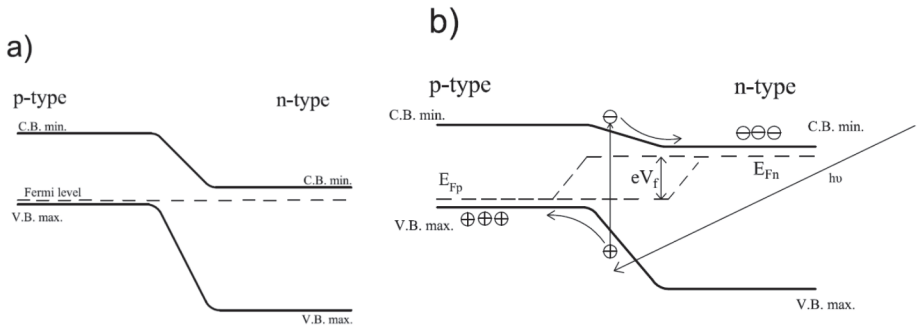

Figure 1. Band structure of the solar cell in thermal equilibrium a) and under illumination b).

According to the technologies used, solar cells can be divided into three main generations [3]:

- **First generation -** solar cells from this generation are based mainly on crystalline silicon wafers, either single crystalline or multicrystalline and have reached efficiencies of approximately 15-25 % [4].
- **Second generation –** is based on the thin film PV technology and includes three main families: 1- amorphous or also microamorpohous silicon; 2- Cadmium Telluride (CdTe) and 3- Copper-Indium- Gallium –Selenide (CIGS).
- **Third generation –** includes novel technologies and materials, such as epitaxial thin films, multijunction and organic PV cells that are still in the development phase or have not yet been widely commercialized similar to novel concepts under study. The aim is to increase also the efficiency of semiconductor solar cells close to the Shockley-Queisser theoretical limit, which is the maximum theoretical efficiency of a solar cell with single p-n junction, according to the absorber bandgap energy value [5].

Solar cell structure is formed between different layers and consists of a front contact, window layer, buffer layer, absorber layer, back contact, and the substrate [2]. Focus in this thesis is mainly on the absorber layer and p-n junction. Absorber layers have a number of parameters that are extremely crucial for solar cell performance. A good absorber material has preferably p-type conductivity; high absorption coefficient, usually 10^4 to 10^5 cm^{-1}; earth abundant constituents, and it should be easy and economical to manufacture. Additionally, it should have a bandgap in the range of 1-1.5 eV for optimal solar energy absorption, low recombination velocity and sufficiently long diffusion length of minority charge carriers [6]. So far, monocrystalline silicon is the most widely spread, studied and manufactured absorber for PV solar cells. In contrast to previously described desired requirements for a good absorber, Si is an indirect bandgap semiconductor with a poor absorption coefficient (10^2 cm^{-1}) [4]. Nevertheless, it held about 80% of the market share in 2014 [8] and the cost of 0.45-0.65 EUR/W [9]. However, it is needed to lower the price of solar power, thus new absorber materials and concepts are under study.

One possibility to achieve the reduction of solar cell prices is to develop and implement new materials for the absorber layer or significantly improve existing devices. Recent research of thin film solar cells is focused on the new and auspicious materials, such as kesterites Cu_2ZnSnS_4, $Cu_2ZnSnSe_4$, $Cu_2ZnSn(SSe)_4$ and binary/ternary compounds like SnS, $AgGaTe_2$, Cu_3BiS_3 . Nevertheless, in order to implement these materials in the solar cell fabrication process, comprehensive knowledge of the physical, optical and electrical properties of the materials is needed.

To gain the necessary knowledge, modulation spectroscopy (MS) is used as a valuable tool to study some of the important fundamental parameters of semiconductors. The basic idea of modulation spectroscopy is to measure an optical spectrum of the sample and at the same time apply external modulation to one of the system parameters. The resulting optical response spectrum has a derivative nature in respect to the perturbing parameter. The first study of modulation spectroscopy was reported by Moss et al. [10] who used transmission configuration. Moss applied the electric field modulations through the contacts to the GaAs sample with a voltage amplifier. It was discovered that operating in reflection rather than in transmission configuration would give much higher resolution than was previously obtained [11]. The focus shifted to the reflectance application in the use of MS and soon the first electroreflectance study was performed and reported by Seraphin et al. [12]. Further, Wang et al. [13] developed photoreflectance spectroscopy in order to find a nondestructive method to study the energy band structure in solids. With different types of modulation spectroscopy techniques we are able to evaluate the bandgap energy, crystal quality, surface/interface electric field, alloy composition etc. One important parameter that describes semiconductors is the bandgap energy, especially in the perspective to use them in solar energy conversion. Bandgap value of an absorber determines absorption edge of the material and also defines the maximum theoretical efficiency of a single junction solar cell. Therefore, determining the precise bandgap value of semiconductors is very important and one possibility is to use MS techniques.

In this thesis, different solar cell absorber materials are characterized by temperature dependent photo- and electroreflectance spectroscopy. Materials under study were: $AgGaTe_2$ [I], CdTe [II], SnS [III], Cu_3BiS_3 [IV], and $Cu_2ZnSnSe_4$ [V]. In papers [I, III, IV] temperature dependent photoreflectance measurements were performed on single crystals [I, III] and thin polycrystalline film [IV]. To evaluate a material bandgap energy and its behavior from a temperature, also give feedback on material quality. In papers [III, V] we used temperature dependent electroreflectance spectroscopy to study p-n junction properties and absorbers' bandgap energy of CdS/CdTe and CdS/$Cu_2ZnSnSe_4$ solar cells, respectively.

1. LITERATURE REVIEW AND THE AIM OF THE STUDY

1.1 Introduction to modulation spectroscopy

The main idea behind different kinds of optical spectroscopy techniques is to study light interaction with material. As a result of the measurement, optical response intensity as a function of the wavelength or energy of the light is obtained. A number of different spectroscopy techniques are available for electrical and optical study, the choice depending on the features of interest. One of them is photoluminescence spectroscopy that provides information about defect structure but not so much about valence – and conduction band edges and transitions above the bandgap. In order to study the wider area of the material energetic structure, other optical characterization techniques need to be used, like spectroscopic ellipsometry, absorption or reflectivity. These are relatively good techniques but with rather limited sensitivity. The sensitivity problems often appear in the studies of novel low-dimensional structures where the material to be investigated is of nanometer size (as in quantum wells, quantum wires or quantum dots) and very often buried inside many other layers of a semiconductor [14]. One possibility to cope with the sensitivity problems is to use modulation spectroscopy methods. This means investigation of a derivative of an optical (i.e. the reflectivity) response with respect to some parameter that is periodically changed, i.e. modulated. Principally, one parameter inside the sample is changed to call out a change in the optical reflectance spectrum of the material [15]. The measured optical signal depends on the joint density of states, making this method sensitive to transitions at the critical point in the Brillouin zone of the studied material. The resulting modulated reflectance spectrum has sharp, derivative–like features on a featureless background even at room temperature [14]. In Fig. 2, a comparison of electroreflectance and reflectivity spectra of GaAs monocrystal is shown. Both spectra were measured over the same photon energy region at room temperature. From the reflectivity spectrum, we can see very broad features with very strong background signal. However, in the electroreflectance spectrum, there are several very well pronounced sharp lines corresponding to the changes in the reflectance spectrum and a negligible background signal [16]. The weak features that are relatively difficult to observe in the reflectivity spectrum are enhanced in the electroreflectance spectrum. These sharp derivatives like features correspond to the interband transitions which are also seen from the band diagram of GaAs in Fig. 3. The modulation mechanism can easily be applied to the sample by varying some parameter related to the sample or the experimental system, such as the wavelength of the light, the applied stress, the temperature, or the electric field. The electromodulation techniques are based on the modulation of the internal or surface electric field. Most common electromodulation techniques are

photoreflectance (indirect electric field modulation) and electroreflectance (direct electric field modulation) spectroscopy where the varying parameter is the internal (built in) electric field. [17]

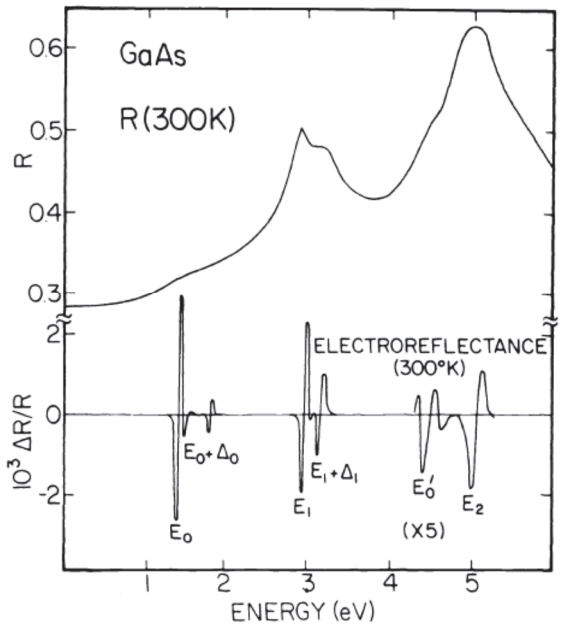

Figure 2. Reflectance and electroreflectance spectra of GaAs at room temperature [16].

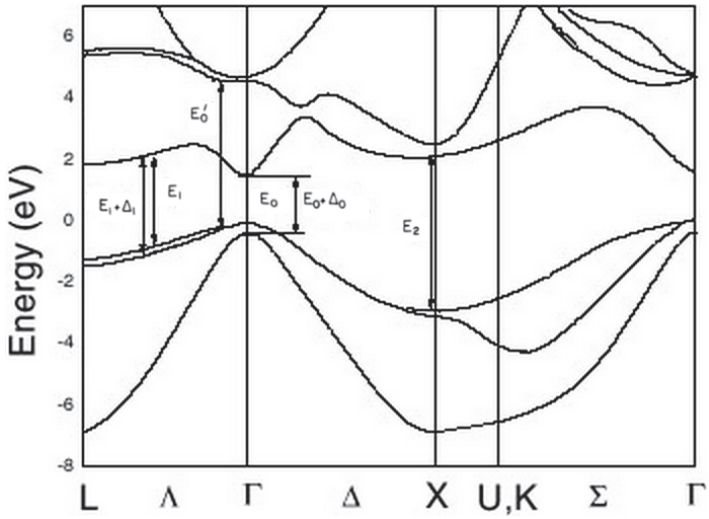

Figure 3. Band diagram of GaAs with the main critical points - E_o , $E_o+\Delta_o$, E_1, $E_1+\Delta_1$, E_o', E_2 [18].

In the case of photoreflectance, the incident pump light (usually laser) that is periodically chopped with given frequency generates carriers in the sample if the energy of the photons is higher than the bandgap energy of the material. The schematic mechanism of photo induced modulation of the internal electric field (F_{DC}) in the case of n-type semiconductors can be seen in Fig. 4. The Fermi-level (E_F) pinning at the surface of the sample produces a space charge region and the surface states are occupied by electrons from the bulk; it is the cause of built-in electric field appearance (F_{DC}) and band bending near the surface. After photon absorption in the sample, the photo-excited carriers (electron-hole pairs) generated close to the surface are separated by the electric field. The minority carriers (in our case holes) are able to move to the surface and neutralize the trapped charges there. As a result, it causes the reduction of the built-in field from F_{DC} to F_{DC} - F_{AC}, where F_{AC} is change in the field [19]. After the laser is turned off, the equilibrium is restored. Change in the electric field causes band bending in the sample. This in turn causes a change in the dielectric function, which is closely related to the optical properties of the material, like the reflectivity coefficient R. Material reflectivity R is different under or without laser illumination and the change between the reflectivity coefficients is visible in the measured reflectance spectrum as a sharp derivative feature near the critical points. A more detailed theoretical approach is described in Section 2. For the heterostructures, the externally generated charge carriers can also move to interfaces and modulate the electric field there. In the case of electroreflectance, external AC-voltage is applied to the heterostructure through the attached contacts with a pulse generator, in order to modulate the electric field within the region of the junction. The applied voltage leads to a carrier redistribution, which influences the internal electric field inside the sample and causes a change of the dielectric function in the space charge region. Therefore, the reflectivity R of the studied heterostructure varies with the applied AC-voltage [19, 20].

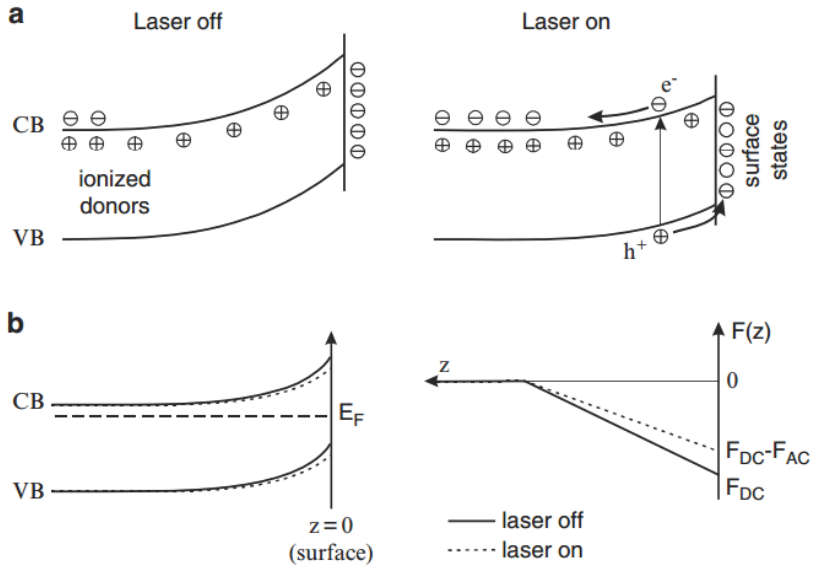

Figure 4. Modulation mechanism in photoreflectance with the n-type semiconductor, a) band bending b) Fermi level position and electric field along the z-direction [19].

The aim of this work was to study various prospective solar cell absorber materials by temperature dependent photo- and electroreflectance spectroscopies. The task was to clarify some open questions related to the electro-optic properties of the studied materials that are still unclear or under discussion. Absorbers under the study were $AgGaTe_2$, CdTe, SnS, Cu_3BiS_3 and CZTSe. One of them is already being used for commercial thin film solar cell production (CdTe) and others are under study or manufactured only on a laboratory scale. However, there is a long way to go to improve the material quality and junction properties of the solar cells to reach the Shockley-Queisser limit.

As a result of these studies, adjusted bandgap energies for the studied absorbers were found and their behavior depending on the temperature was determined; material crystal quality was evaluated and the magnitude of surface/interface electric field was estimated. Additionally, for CdTe solar cells, the p-n junction properties were studied and solid solution of CdS_xTe_{1-x} was detected in the depletion region. Finally, modulation spectroscopy proves its advantages and implemental simplicity in the semiconductor material research in a wide temperature range.

1.2 Prospective materials for solar energy conversion

1.2.1 $AgGaTe_2$

$AgGaTe_2$ is one of the chalcopyrite tellurides that belongs to the group of I-III-VI_2 semiconductor family. Chalcopyrite tellurides' unique optical, magnetic, and electrical properties have raised not only fundamental interest; in addition, they offer an excellent possibility in technological applications [21]. The most well-known chalcopyrite ternary is $CuInSe_2$. It is used mainly in solar energy conversion. Thin film solar cells with the $CuInSe_2$ absorber have shown an efficiency as high as 20.9% [22]. $AgGaTe_2$ is also a potential absorber material for solar energy conversion, electro-optical modulators, narrow-band filters in the visible and IR spectra ranges [23]. It has high absorption coefficient $>10^4$ cm^{-1} and bandgap energy close to the optimal value for solar energy conversion. It is reported that $AgGaTe_2$ has a direct bandgap with energy around 1.3 eV at room temperature [24, 25].

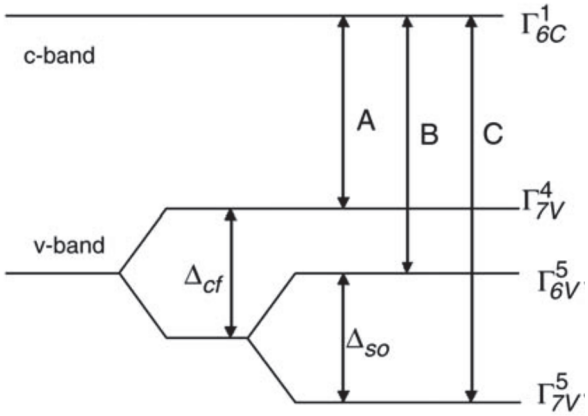

Figure 5. Schematic band structure of chalcopyrite ternary, showing splitting of the valence band due to the crystal field splitting (Δ_{cf}) and spin-orbit coupling (Δ_{so}). $\Gamma^{\ 4}_{7V}$, $\Gamma^{\ 5}_{6V}$ and $\Gamma^{\ 5}_{7V}$ are three split valence bands and $\Gamma^{\ 1}_{6C}$ conduction band; A, B, C show three different bandgaps [26].

$AgGaTe_2$ lattice type is tetragonal like for all chalcopyrite ternaries. Photovoltaic solar cell with an $AgGaTe_2$ absorber layer has shown an efficiency of 2.1% [27]. According to the referred paper, the relatively low efficiency is caused by the poor p-n junction formation between the used p-type $AgGaTe_2$ and n-type Si [27]. Due to valence band splitting caused by the combined effect of crystal field splitting (Δ_{cf}) and spin-orbit coupling (Δ_{so}), chalcopyrite ternaries have up to three energy gaps, see Fig. 5 [26]. Tell et al. [24] have reported

$AgGaTe_2$ bandgaps with energy 1.316 eV, 1.472 eV and 2.26 eV, measured using optical absorption. Although $AgGaTe_2$ is a prospective material for solar energy conversion and different electro-optic devices, fundamental studies published about this semiconductor are scarce, especially about bandgap engineering. Majority of the published studies include photoluminescence properties of a material and its defect structure [21]. At the same time, there is wide variation in the actual value of its bandgap energy and its electronic band structure has different interpretations. The most common method to measure bandgap energy is an optical absorption. However, it is known that in chalcopyrite ternaries large potential fluctuations are usually present and therefore the density of states function near band edges is quite complex [28]. That is why absorption spectra have strong dependence on the depth of these potential fluctuations. Deeper fluctuations usually give additional absorption at lower energies and thus the absorption tail is formed. The shape of this tail is not always known and therefore the bandgap energy calculated from the absorption spectrum could be incorrect [29]. Therefore, modulation spectroscopy techniques could give us more accurate bandgap energy and clarify the discrepancy about its real value.

1.2.2 CdTe

CdTe is one of the most widely investigated semiconductors used in solar energy conversion. CdTe has high absorption coefficient $> 5 * 10^5$ cm^{-1}, which means that roughly 99% of photons that have energy greater than bandgap can be absorbed within 2 μm of CdTe thin film. It has a direct bandgap around 1.5 eV that is nearly optimally matched to the solar spectrum for PV applications [30]. P-type CdTe is widely used as an absorber material in thin film solar cells and it holds the second place in the world after silicon as the most utilized solar cell material. However, the record efficiency of CdTe solar cells 21.7% [31] is far from its theoretical maximum (Shockley-Queisser limit) 29.7% [5]. On the one hand, some authors believe that the efficiency is limited by the graded bandgap in junction. In CdS/CdTe solar cells sulphur diffuses into CdTe and Te diffuses into the CdS and CdS_xTe_{1-x} solid solution is formed in the junction area. Substitutional Te impurities in CdS form isovalent defect levels inside the band gap. These isovalent defects form electron traps and are responsible for large bandgap reduction and low photocurrent in the CdS layer [32, 33]. On the other hand, the CdS_xTe_{1-x} layer is thought to be important because it relieves strain at the CdS/CdTe interface that would otherwise exist due to the 10% lattice mismatch between these two materials [34]. As far as there is uncertainty in this field, every study which tries to clarify the effect of the CdS_xTe_{1-x} layer between CdS and CdTe is valuable. Also, it is clear that one limiting factor of CdTe solar cell efficiency is a back contact barrier. It is often detected from I-V measurements where light curve crosses dark curve at positive voltages,

commonly referred to as ”rollover“. It has been shown that it is relatively difficult to form ohmic contact between CdTe and a metal, for the back contact of a solar cell [33]. Although CdTe is a well-known material for solar energy conversion, there are no temperature dependent electroreflectance studies conducted in order to investigate the depletion region, changes in the internal electric field and its behavior depending on the temperature.

1.2.3 SnS

SnS, a group IV–VI semiconductor, is a cheap and abundant material with low toxicity. SnS is a binary compound semiconductor with a high absorption coefficient of 10^4–10^5 cm^{-1} and a bandgap energy of about 1.3 eV, it also has appropriate carrier concentration ((p)~10^{16} cm^{-3}) [35]. It has been reported that with Ag doping it is possible to increase carrier concentration in SnS up to 10^{18} cm^{-3} [36]. According to the listed parameters, we can conclude that SnS is a prospective material to be used in solar energy conversion. Theoretical calculations predict a conversion efficiency of up to 25% for SnS photovoltaic devices [37]. However, recent world record of SnS solar cell is only 4.46% [38]. The available amounts of tin and sulfide are large enough to supply entirely the world’s photovoltaic production demand [36].

SnS crystal structure belongs to the orthorhombic space group *Pbnm* where six sulphur atoms surround each tin atom with three short Sn-S bonds within the layer and three long bonds connecting two neighboring SnS layers [47]. SnS has additionally hexagonal and cubic structures. Due to the easy formation of additional phases such as SnS_2 and Sn_2S_3 [35], the growth of polycrystalline SnS thin film or SnS monocrystal must be very carefully controlled. Even small deviation in temperature, time or vapor pressure causes the deviation from a narrow monophase region. These secondary phases cause bandgap shifting to higher values and a decrease of solar cell performance [39]. SnS bandgap values in the range of 1.1-1.87 eV at room temperature are reported in the literature [35, 37]. The use of modulation spectroscopy would help to clarify this mismatch and give more precise value of bandgap energy.

1.2.4 Cu_3BiS_3

Ternary compound Cu_3BiS_3 is a new semiconductor for photovoltaic applications with non-toxic elements that have sufficient margin in the earth crust. Its fundamental bandgap energy is estimated to be 1.5 - 1.7 eV [40]; it has a high absorption coefficient and p-type conductivity. The analysis has revealed that Cu_3BiS_3 has a much higher absorption coefficient (>10^5 cm^{-1}) than other Cu-S based materials like $CuInS_2$ and Cu_2ZnSnS_4 [40]. Some authors claim that Cu_3BiS_3 is an indirect bandgap material [40]; at the same time, Cu_3BiS_3 is reported to be a direct bandgap material [41]. There are still some issues related

to fundamental physical properties of Cu_3BiS_3 that are not well understood. As already described, there is no common consensus which type of bandgap material it is - direct or indirect. Furthermore, the bandgap energies reported vary in the range of 1.15 to 2.75 eV [40, 41, 51], different types of measurements give different values of the bandgap energy. Although many studies have covered the fabrication of Cu_3BiS_3 thin films, no reports of a working Cu_3BiS_3 solar cell are available. However, according to the material properties, research interest on this compound and demand of new solar cell materials, fabrication of the Cu_3BiS_3 solar cell is predicted to be reported in the near future. As long as there are uncertainties in the bangap energy values of Cu_3BiS_3, every work is valuable and the use of MS techniques could clarify these mismatches.

1.2.5 $Cu_2ZnSnSe_4$

Kesterite $Cu_2ZnSnSe_4$ (CZTSe) is a potential material for solar energy conversion. It has p-type conductivity, high absorption coefficient 10^4 cm^{-1} and direct bandgap around 1.0 eV [2]; additionally, it is attractive due to the Earth abundant constituents [42]. Due to the similar crystalline lattice of $Cu(InGa)Se_2$ (CIGS) and CZTSe, kesterite is believed to have similar optical and electronic properties. Solar cells made with a CIGSe absorber have shown very good solar cell performances and hold the conversion efficiency record as high as 21.7% [43]. However, the main disadvantage with CIGS is the use of expensive In and Ga, which are replaced with cheap Zn and Sn in kesterite. The reported conversion efficiency record for CZTSe-based solar cells exceeds 11.6% [44], making them potential candidates for the large-scale production of a thin film PV [42]. Many issues occur during the growth of kesterite and affect the fundamental material properties. One of them is the problem with the formation of different binary and ternary phases, such as ZnSe, $Cu_{2-x}Se$, SnSe, $SnSe_2$, and Cu_2SnSe_3 [28]. Additionally, CZTSe can exist as an ordered - or disordered kesterite crystal structure, which is related to the nature of intrinsic defects that causes structural disorder in the cation sublattice of the host lattice. The degree of disorder depends on the cooling rate after sample synthesis, rapid cooling usually gives the highest degree of disorder [45]. It was found that the critical temperature is 200±20 ^oC where the order-disorder transition takes place [42]. Ray *et al.* [42] have reported that the bandgap energy could vary up to 110 meV between fully ordered and - disordered material. Based on this knowledge, the bandgap energy value is a good parameter to describe the material order-disorder ratio. In this perspective, the use of MS to find bandgap energy could be very useful.

2. THEORY OF MODULATION SPECTROSCOY

As described in Section 1, in modulation spectroscopy, a periodic perturbation produces a sharp derivative –like features in the optical response of the sample [46]. The optical response is measured using either a reflectance or transmission configuration. The derivative nature of the spectra enhances the features in the energy region of interband transitions at the critical point in the Brillouin zone. Depending on the modulation source, we can classify modulation spectroscopy into two general categories. The first type of perturbation maintains the translation invariance of the crystal, however it can change the symmetry of the lattice. This type of modulation includes changes in the sample temperature or its lattice constant through applied temperature or stress modulation, respectively. In this case, the modulated optical reflectance spectrum has a nature of first derivative with respect to a perturbing variable [16]. The second type of perturbation breaks the translational invariance of the studied crystal along an appropriate direction, therefore electrons and/or holes are being accelerated. The resulting modulated optical reflectance spectra have a nature of the third derivative with respect to photon energy [16]. An applied electric field modulation is one of the causes of acceleration of electrons and holes in the opposite direction in bulk semiconductor that results as the third derivative like the spectra of the modulated optical reflectance function [16]. The resulting spectrum has a sharp derivative – like features on a featureless background.

In electromodulation, the relative change in the reflectivity coefficient can be defined as:

$$\frac{\Delta R}{R} = \frac{R_{off} - R_{on}}{R_{off}} , \qquad (1)$$

where R_{on} and R_{off} are the reflection coefficients at the application of electromodulation and without it. The electromodulation can be applied indirectly with a pump beam (laser) in the case of PR and directly with a voltage generator in the case of ER. It is known that electrical and optical properties of a material are described by the complex dielectric function:

$$\varepsilon = \varepsilon_1 + i\varepsilon_2 , \qquad (2)$$

where ε_1 is the real part of the function and ε_2 the imaginary part of the function. The value ε_1 shows the degree of polarization of a material when an electric field (oscillating light wave) is applied due to the creation of electric dipoles in the material. Variable ε_2 is related to light absorption in a material. The real and imaginary parts of the complex dielectric function are related to each other by Kramers-Kronig relation [48]. If there is an applied external modulation on the sample, the differential change in the reflectance is related to the perturbation of

the complex dielectric function and the effect of the modulation parameter on these properties must appear as a change in the real and imaginary parts of it [49]. According to this, the relative change in the reflectivity coefficient can be written as expressed by Seraphin and Bottka [50]:

$$\frac{\Delta R}{R} = \alpha(\varepsilon_1, \varepsilon_2)\Delta\varepsilon_1 + \beta(\varepsilon_1, \varepsilon_2)\Delta\varepsilon_2 \,, \tag{3}$$

where R is the reflectivity, $\Delta\varepsilon_1$ and $\Delta\varepsilon_2$ are changes in the real and imaginary part of the dielectric function, α, β are the Seraphin coefficients related to the unperturbed dielectric function ε_1 and ε_2 [50] and can be written as:

$$\alpha = \frac{1}{R}\frac{dR}{d\varepsilon_1} \tag{4}$$

and

$$\beta = \frac{1}{R}\frac{dR}{d\varepsilon_2} \tag{5}$$

[48]. Seraphin coefficients have a characteristic variation in semiconductors: below the bandgap, the imaginary part of the dielectric function can be neglected, because usually light absorption does not take place below the bandgap and the equation is formed as:

$$\Delta R/\Delta R = \alpha(\varepsilon_1, \varepsilon_2)\Delta\varepsilon_1 \,. \tag{6}$$

Above the bandgap energy and its vicinity, both parts, real and imaginary, should be taken into account [52].

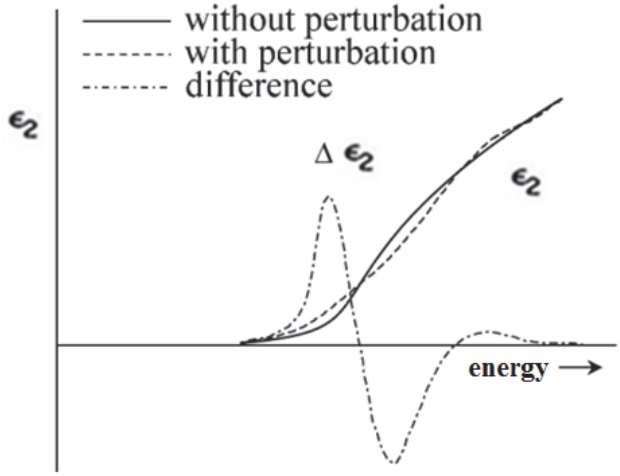

Figure 6. Schematic diagram of the imaginary part of the dielectric function in the vicinity of the absorption edges with the third derivative modulation process (PR) [53].

Fig. 6 shows the imaginary part of the dielectric function in the vicinity of the absorption edge [53] at electric field modulation. The imaginary part (ε_2) of the dielectric function vary marginally with the electric field, however its influence is more clearly seen in the change of the imaginary part ($\Delta\varepsilon_2$) and it has a shape of the third derivative at the energy of the optical transition.
There are additional parameters that also affect the calculation of the dielectric function whether the ε has a nature of a derivative or additional oscillations appear. When the electric field is applied to the semiconductor, the resulting characteristic energy, so called "electro-optic energy"- $\hbar\theta$, of a charged particle with mass μ can be found with the equation by Aspnes [53]:

$$\hbar\theta = \sqrt[3]{\frac{e^2\hbar^2F^2}{2\mu}} \quad , \tag{7}$$

where, F is the strength of the electric field, μ is the reduced interband mass of the charge particle in the direction of the field, $\hbar$ is reduced Planck`s constant, e is the electron charge. According to the relative strengths of electro-optic energy, electromodulation can be classified into three categories: low, intermediate, and high field [53]. To estimate the strength of the field, we have to bring in additional three parameters: eFa_0 - potential drop across the unit cell (where a_0 is the lattice constant), E_g - bandgap energy, and Γ-broadening parameter due to lifetime-induced uncertainty in perturbed levels. The broadening parameter, in other words linewidth, Γ is often used as a measure of crystal quality since its magnitude is primarily determined by lattice defects such as disorders, vacancies, and impurities [33]. The previously described three field categories, together with parameters and their requirements are summarized in Table 1[53].

Table 1. Three ranges of ER spectra

	Perturbation energy	Potential drop vs. bandgap energy
Range	Interband	Interband
High	$\lvert\hbar\theta\rvert \gg \Gamma$	$eFa_0 \sim E_g$
Intermediate	$\lvert\hbar\theta\rvert \geq \Gamma$	$eFa_0 \ll E_g$
Low	$\lvert\hbar\theta\rvert \leq \Gamma$	$eFa_0 \ll E_g$

In a low electric field where the requirement $|\hbar\theta| \leq \Gamma$ is satisfied, the electromodulation destroys the translation symmetry of the material and can cause acceleration of free electrons and/or holes in the crystal. In this case, we can use the approach developed by Pollak and Glembocki [16]. As it is known, an electric field has influence on the dielectric function; in this regard, it is needed to find the energy gained by the free particle if it is in an electric field. For that, Aspnes and Rowe [54] have replaced the wave vector k with $k +$

$qFt/\hbar$ in the time dependent Schrodinger equation. As a result, they found that energy gained by the free particle is equal to

$$E(F) = \frac{q^2F^2t^2}{2\mu}. \quad (8)$$

If we consider an optical structure near a critical point with energy E_g, the dielectric function has the general form [16]:

$$\varepsilon = \varepsilon(E - E_g, \Gamma), \quad (9)$$

where E is photon energy.
The change in the dielectric function induced by an electric field is given by

$$\Delta\varepsilon = \varepsilon\left(E - E_g + E(F)\right) - \varepsilon\left(E - E_g\right). \quad (10)$$

If the field is sufficiently small (low field regime), Eq. (10) can be expanded in a Taylor series to yield [16]:

$$\Delta\varepsilon = E(F)\left(\frac{d}{dE}\right)\varepsilon\left(E - E_g, \Gamma\right) = \left(\frac{q^2F^2t^2}{2\mu}\right)\left(\frac{d}{dE}\right)\varepsilon\left(E - E_g, \Gamma\right). \quad (11)$$

In quantum mechanics, the time t is also an operator:

$$t = i\hbar\left(\frac{d}{dE}\right), \quad (12)$$

Eq. (11) becomes

$$\Delta\varepsilon = \left(\frac{q^2F^2\hbar^2}{2\mu}\right)\left(\frac{d^3}{dE^3}\right)\varepsilon\left(E - E_g, \Gamma\right) = (h\theta)^3\left(\frac{d^3}{dE}\right)\varepsilon(E - E_g, \Gamma) \quad (13)$$

It can be seen from Eq. (13) that $\Delta\varepsilon$ is proportional to the square of the electric field since $\Delta\varepsilon \sim (h\theta)^3 \sim F^2$ [16]. If we assume uniform broadening, the dielectric function has a generalized Lorentzian form for solids [55] and $\Delta\varepsilon$ from Eq. (13) can be computed. Then, according to Eqs. (3) and (13), the change in reflectivity can be expressed generally as:

$$\frac{\Delta R}{R} = Re\left[Ae^{i\varphi}\left(E - E_g + i\Gamma\right)^{-m}\right]. \quad (14)$$

After converting Eq. (14) we obtain:

$$\frac{\Delta R}{R} = A \times \left[\left(E - E_g\right)^2 + \Gamma^2\right]^{-\frac{m}{2}} \times cos(\varphi - m\psi), \quad (15)$$

and

$$\psi = cos^{-1}\left(\frac{E-E_g}{\sqrt{\left(E-E_g\right)^2+\Gamma^2}}\right), \tag{16}$$

where E is the photon energy and A, φ, E_g, and Γ are the amplitude, phase, energy, and broadening parameter of the spectrum. The amplitude and phase factors A and φ determine the amplitude and asymmetry of the lineshape respectively, E_g and Γ determine the energy location and width of lineshape [49]. Variable m is a parameter that depends on the critical point type. For 2D critical point, one-electron transition $m=3$; for 3D critical point, one-electron transition $m=2.5$; for 1D excitonic transition $m=2$. Additionally, m shows an order of the derivative. Regularly, low field electromodulation spectra exhibit one positive and one negative extrema for each critical point. It can be seen in Fig. 7 how parameters interact in determining the lineshape for 2D and 3D simple parabolic critical point models. The amplitude factor only scales the lineshape determined by φ, m, E_g , and Γ and thus does not enter into the actual lineshape determination. Only the phase φ is the dominant factor determining the lineshape, nevertheless, disregarding the magnitude of φ, the critical point energy always situates between the two extrema and the energy separation between the two extrema is nearly constant. [49].

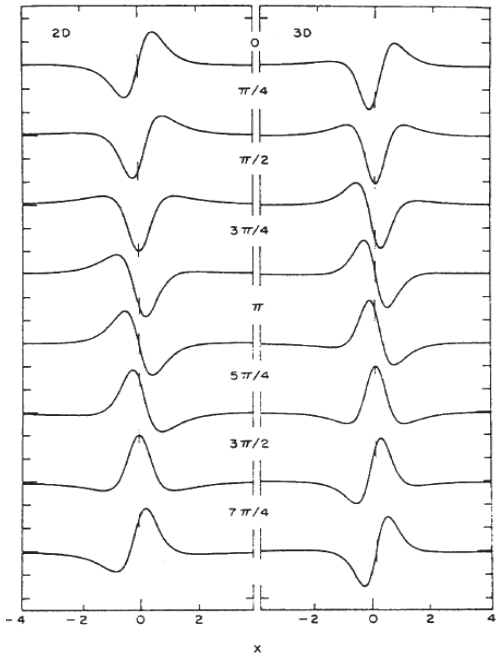

Figure 7. Lineshape of $\Delta R/R$ depending on the phase φ variation for 2D- and 3D critical point models, critical point is at x=0 [49].

In the intermediate electric field approach, where$|\hbar\theta| \geq \Gamma$ and $eFa_0 \ll E_g$, the dielectric function can exhibit Franz-Keldysh oscillations (FKO) [17], see Fig. 8.

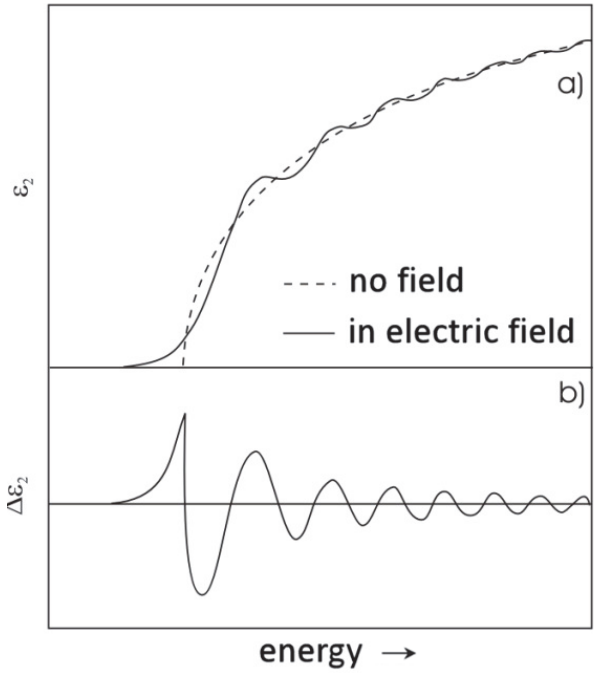

Figure 8. Schematic diagram of dielectric function imaginary part (ε_2), in the intermediate electric field, with electromodulation and without a), FKO are clearly seen in the change of the imaginary part ($\Delta\varepsilon_2$) [56].

Beyond the low field regime, the Franz-Keldysh effect causes a more complicated lineshape that can be presented with the Airy function *Ai* and *Bi* with their derivatives [46], the change in the dielectric function can be expressed as:

$$\Delta\varepsilon \propto \frac{1}{E^2}\sqrt{\hbar\theta}[G(\eta) + iH(\eta)] \tag{17}$$

where

$$G(\eta) = \pi\left[Ai'(\eta)Bi'(\eta) - Ai(\eta)Bi(\eta) + \sqrt{\eta}u(\eta)\right], \tag{18}$$

$$H(\eta) = \pi\left[Ai'^2(\eta) - \eta Ai^2(\eta) - \sqrt{-\eta}u(-\eta)\right], \tag{19}$$

$$\eta = \frac{E-E_g}{\Gamma}, \tag{20}$$

and *u* is a Heaviside unit step function.

It can be seen from Eqs. (17)-(19) that the exact form of $\Delta R/R$ is quite complicated in the intermediate field regime. However, Aspnes and Studna have developed the expression in [17] and have derived a relatively simple formula:

$$\frac{\Delta R}{R} \propto \frac{1}{E^2(E-E_g)} exp\left[-2\left(E-E_g\right)^{\frac{1}{2}} \frac{\Gamma}{(\hbar\theta)^{\frac{3}{2}}}\right] \times cos\left(\frac{4}{3}\frac{(E-E_g)^{\frac{3}{2}}}{(\hbar\theta)^{\frac{3}{2}}} + \chi\right) \quad (21)$$

From the expression above, position of the n[th] extreme in the FKO is given by:

$$n\pi = \frac{4}{3}\frac{(E_n-E_g)^{\frac{3}{2}}}{(\hbar\theta)^{\frac{3}{2}}} + \chi\,, \quad (22)$$

where E_n is the photon energy of the n[th] extreme and χ is an arbitrary phase factor [17]. Fig. 9 represents the electromodulation spectra of a GaAs monocrystal, as it can be seen, spectra exhibit FKO, indicating the intermediate electric field.

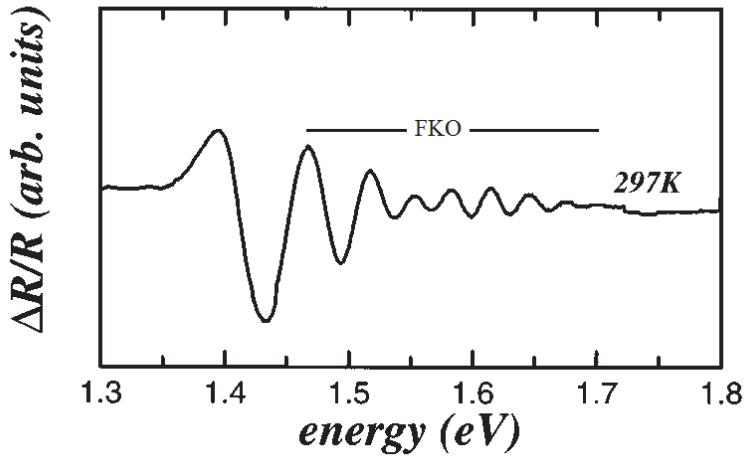

Figure 9. PR spectrum of GaAs, FKO is exhibited in the spectrum, indicating the intermediate field regime [57].

The high electric field case is rather similar to that of the intermediate field where FKO will appear into the spectrum above the bandgap energy. However, the electro-optic energy must fulfill the requirements $|\hbar\theta| \gg \Gamma$ and $eFa_0 \sim E_g$ and additionally Stark shifts are produced, where energy levels in the crystal are shifted due to the strong electric field [58].

3. EXPERIMENTAL DETAILS

3.1 Photoreflectance and electroreflectance measurements

Photoreflectance (PR) measurements were made with a traditional setup where the f=40 cm grating monochromator together with a 250 W halogen bulb was used for a primary beam and the 80 mW semiconductor laser diode (λ=405 nm) as a secondary beam. The reflectance signal at 85 Hz was detected using a Si detector and a lock-in amplifier. For PR measurements, the samples were mounted inside the closed-cycle He cryostat that enables us to measure in the temperature range from 10 K to 325 K. The samples were mounted inside the cryostat on a vertical surface of the cold finger using silicon grease as an adhesive material. The schematic view of the experimental setup is shown in Fig. 10 a).

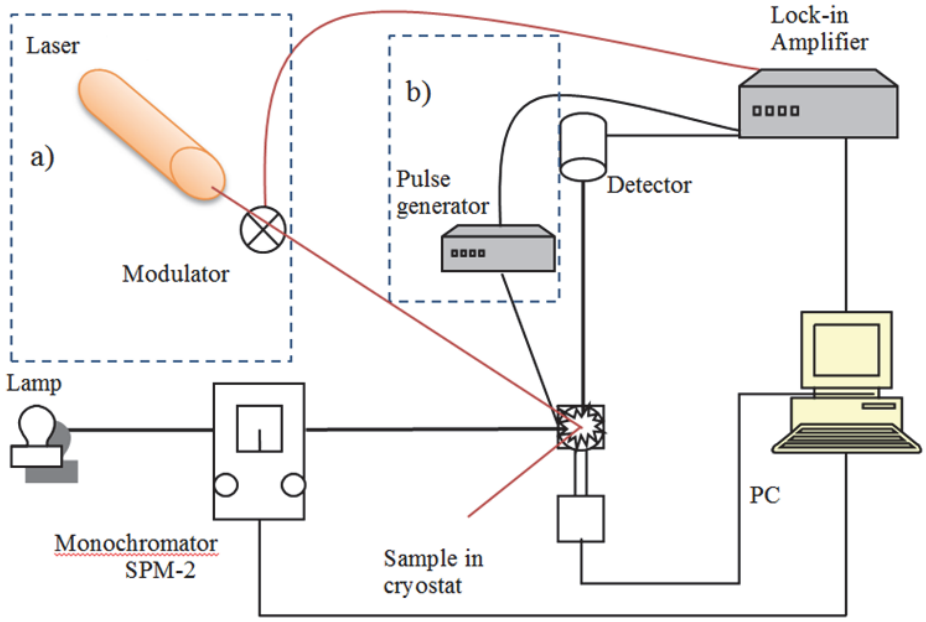

Figure 10. Schematic view of a) photoreflectance and b) electroreflectance setups.

In the electroreflectance measurements, DC- and AC-voltages were applied to the solar cell under study via back and front contact in order to modulate internal electric field in the depletion region. Voltage was generated by a pulse generator with the frequency of 275 Hz, AC value was ±0.8 V and DC component -0.8 V. Computer controlled grating monochromator SPM-2 (f=40

cm) together with a 250W halogen bulb was used for illumination. The ER signal was detected using a Si or Ge detector and a lock-in amplifier (SR 810). Solar cells under study were mounted into a closed-cycle He cryostat to perform temperature dependent ER measurements in the range of T=100-300 K. Schematic view of the experimental setup is shown in Fig. 10 b) and Fig. 11.

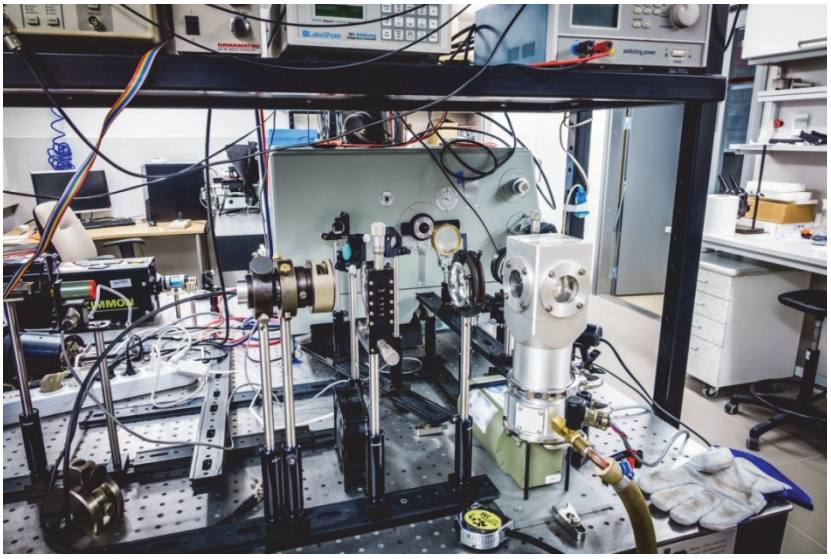

Figure 11. Experimental setup of photoreflectance measurements at Tallinn University of Technology.

3.2 Sample preparation

3.2.1 $AgGaTe_2$

An ingot of $AgGaTe_2$ (AGT) has been grown by the vertical Bridgman technique often used for fabrication of $CuInSe_2$ and the other chalcopyrite ternary compounds [59]. A pseudobinary phase diagram for $AgGaTe_2$ has been determined by Palatnik and Belova [60], establishing the melting point at 725.7 ^oC [61]. First, a near stoichiometrical mixture of high (99.999%) purity Ag, Ga and Te was sealed under vacuum of 10^{-5} mbar in a thick wall (3mm) quartz ampoule of 10 mm inner-diameter. Then, this mixture was prereacted at 900 ^oC for two hours in a rocking furnace and solidified in horizontal position. After cooling down, the ampoule was introduced into the upper (hot) zone of a two zone vertical furnace. The material was melted again and held at a temperature 900 ^oC for six hours. Then, the temperature in the upper part of the furnace was reduced to 800 ^oC and the lower part to 700 ^oC. The furnace was slowly moved

up, translating the ampoule into the lower (cold) zone with the speed of 2 cm a day through temperature gradient. Solidified material was cooled at the rate of 3 ^{o}C/h down to 200 ^{o}C. In the middle part, the grown ingot had a 2 cm long cylindrical shape single grain of $AgGaTe_2$. The elemental composition of the resulted crystals was confirmed by EDX and RBS measurements. The elemental composition was varying along the ingot gradually becoming Ag rich close to the end of freeze (top) zone. The middle part from ingot was sliced and chosen for our investigation. Phase analysis was performed with Raman spectroscopy (Fig. 12) where the main peaks are clearly seen; the most intensive is at 130 cm^{-1} and the other peaks are at 94, 201, and 221cm^{-1}. These peaks are typical of an AgGaTe2 crystal [62] and these spectra confirm that we have a pure AgGaTe2 single crystal without additional phases.

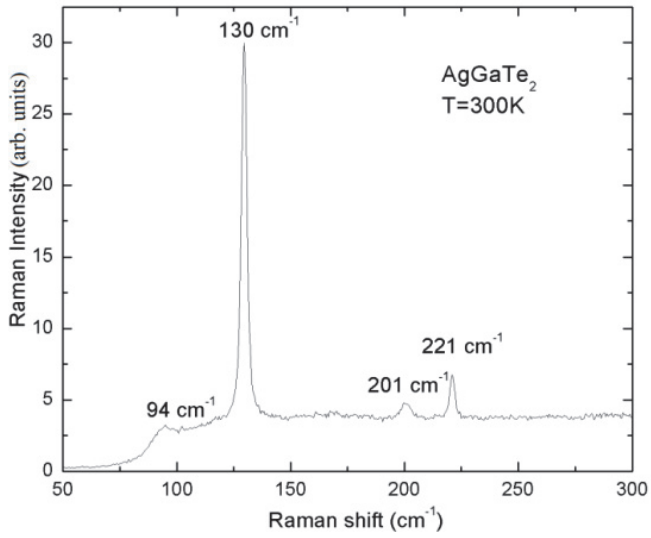

Figure 12. Raman spectra of $AgGaTe_2$ at room temperature. Typical AGT peaks are seen in the figure.

3.2.2 CdTe

We studied two types of CdS/CdTe solar cell samples. Thin film CdS/CdTe solar cells were fabricated on glass substrates with an area of 2x2 cm^2, covered with a SnO_2 layer with a sheet resistivity of about 10 Ω/□. SnO_2 served as the transparent front contact to CdS. Both undoped CdS and CdTe layers were grown sequentially without intermediate processing by the close-space-sublimation (CSS) method. CdS had the resistivity of 2-3 Ω·cm and transparency over 80%. The CdTe layers had the resistivity in the range of

~$5 \cdot 10^5$ Ω·cm. After the CdTe layer was deposited, the structures were held in $CdCl_2$:H_2O saturated solutions and then annealed in the air at 410 ºC for ~30 min. To minimize the back contact barrier, an additional layer (~300nm) of Te for one cell (**Cell 1**) or Cu for the other cell (**Cell 2**) was used. In Cell 1 the CdTe was deposited at a substrate temperature of 440 °C, in Cell 2 at the temperature of 430 ºC. The CdTe source temperature in both cases was 580 °C. All cells were completed with a Ni metal contact thermally deposited in vacuum.

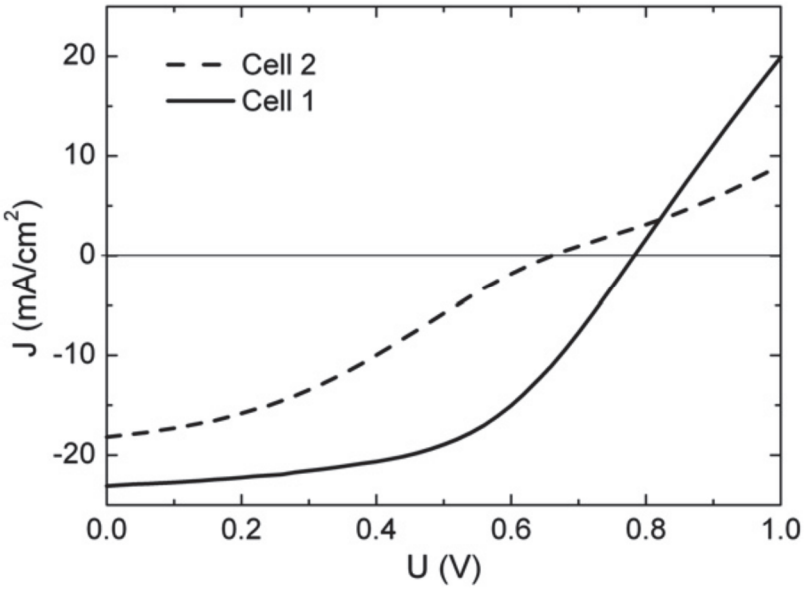

Figure 13. The room temperature I-V curves of studied solar cells under illumination.

Table 2. Solar cell performances under AM 1.5 illumination conditions

Sample	Buffer	V_{OC} (mV)	J_{SC} (mA/cm^2)	FF (%)	Efficiency (%)
Cell 1	Te	783	23.1	53.1	9.6
Cell 2	Cu	661	18.2	34.5	4.1

Typical I–V curves of thin film CdS/CdTe heterojunction solar cells under the illumination are presented in Fig. 13. As it can be seen from Fig. 13 and Table 2, Cell 1 shows better solar cell parameters, however both solar cells were fabricated nearly in the same conditions. Cell 2 has shortcomings in all parameters characteristic of a solar cell, however the largest drop is in the fill factor, which indicates higher series resistance that probably is related to the buffer between CdTe and the metallic back contact. However, drop in V_{OC} indicates changes in the junction.

Also, it can be seen in Fig. 14 that in comparison with the external quantum efficiency measurements, Cell 1 has much steeper QE spectrum at the long wavelength side than Cell 2. The steeper shape of Cell 1 QE spectrum at

the long wavelength side leads to the steeper bandgap edge and could be one reason for better junction properties and higher solar cell performances.

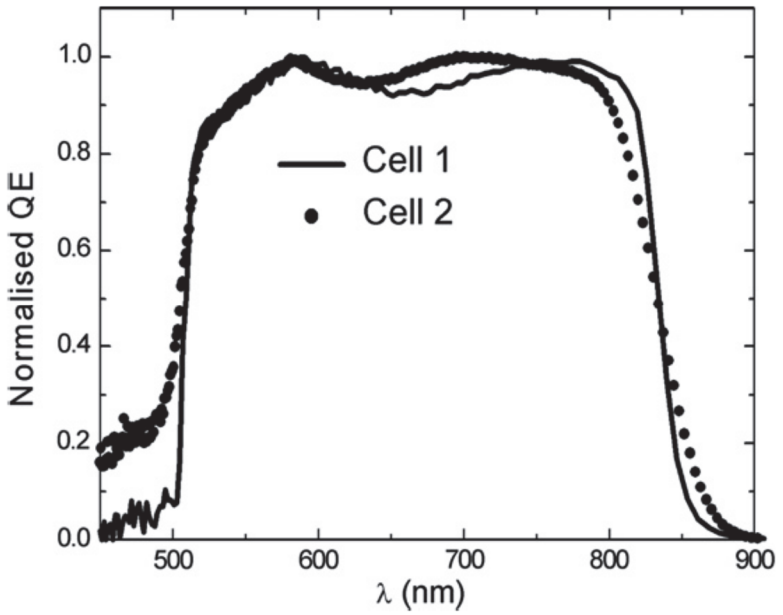

Figure 14. Normalized QE curves of the studied solar cells.

3.2.3 SnS

The SnS was synthesized from "pro analysi" quality Sn and 3N purity S. Precursors were mixed and sealed into an evacuated quartz ampoule and inserted into the furnace. The furnace was slowly heated up to 700 ^{o}C for about 100 hours and kept at that temperature for 24 h. After that the furnace with the ampoule was cooled to the room temperature. Later the same polycrystals were sealed into the evacuated ampoule to perform sublimation. Hot part of the ampoule where the SnS powder was located was kept at around 650 ^{o}C and SnS single crystals grew at low temperature zone at 620 ^{o}C, sublimation process was running for three weeks. Single crystals of SnS had platelike shape with good reflecting surface and sized at approximately 3x3 mm. Raman spectra of the SnS monocrystal are shown in Fig. 15. All these four peaks belong to the orthorhombic SnS, as reported in [63]. Additionally, Fig. 15 shows the full width of the measured Raman peaks at half maximum (W), relatively thick pikes, indicating comparatively good crystal quality. Orthorhombic crystal structure was additionally proved by XRD measurements presented in Fig. 16.

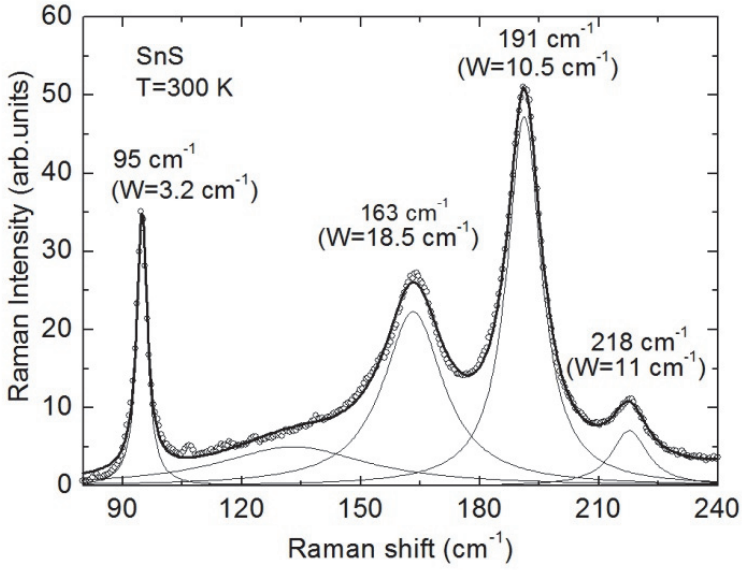

Figure 15. Room-temperature Raman spectrum for single-crystal SnS together with peak position and peak full width at half maximum (W).

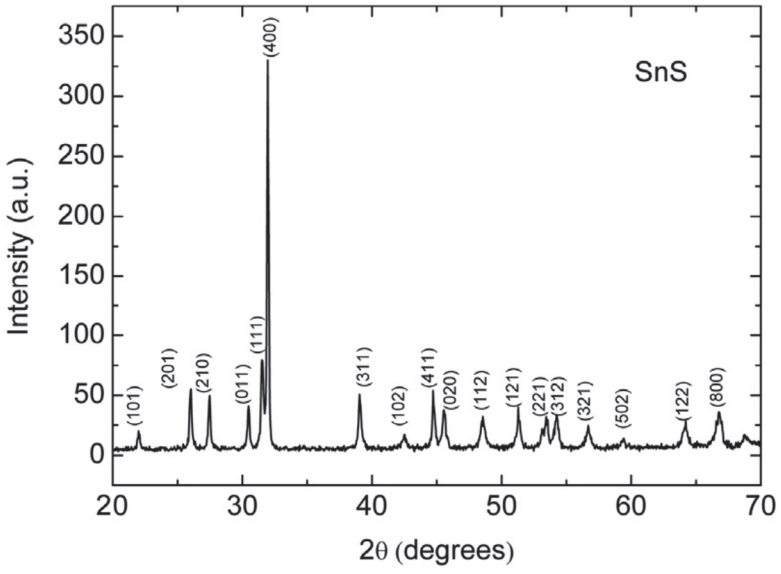

Figure 16. XRD pattern for SnS single crystals.

3.2.4 Cu_3BiS_3

Thin films of Cu_3BiS_3 were fabricated using a two stage process. First, 0.3 μm thick precursor layers of Cu and Bi were magnetron sputtered on Mo-coated soda-lime glass from 5N-purity elemental targets. 1.5 μm thick films of 4N-purity sulphur were thermally evaporated on these precursor layers. Then such structures were heated for 30 min at a temperature of 250 ^oC in Ar atmosphere at a pressure of 1 mbar. An excess of sulphur was provided in order to ensure full sulphurization of the precursor layer during the heating process. Hot probe measurements revealed *p*-type conductivity of the synthesized Cu_3BiS_3 material. The XRD pattern of the film along with the standard (pdf: 043-1479) orthorhombic pattern shown in Fig. 17 reveals the formation of a wittichenite lattice structure (with the lattice parameters a =0.7661 nm, b = 1.0388 nm, c = 0.6712 nm), peaks associated with metallic molybdenum and bismuth, implying the presence of Bi clusters.

Raman spectra measured at different points of the films at room temperature consistently reveal four modes at 96, 125, 264 and 292 cm^{-1}, as shown in Fig. 18. The dominant peak at 292 cm^{-1} has a full width at half maximum (FWHM) of 12 cm^{-1}, which is a relatively low value, indicating rather good crystal quality. Because of no references found in the literature about Cu_3BiS_3 Raman spectra, we have to rely on the XRD pattern of Cu_3BiS_3 that confirms the existence of single phase Cu_3BiS_3.

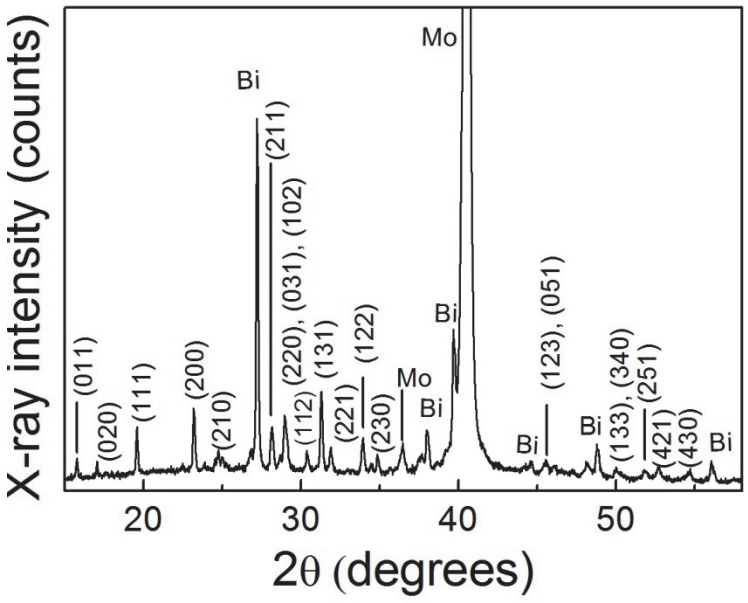

Figure 17. XRD pattern of Cu_3BiS_3/ Mo/ glass.

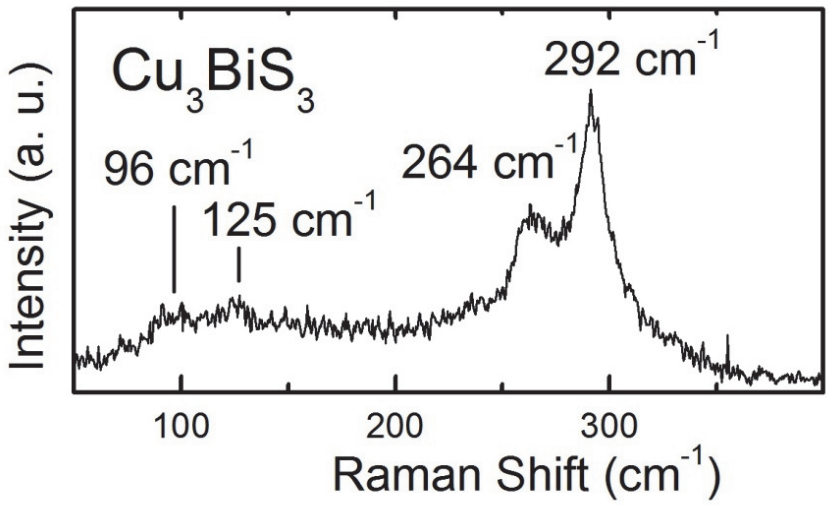

Figure 18. Raman spectra of Cu_3BiS_3 thin film.

3.2.5 $Cu_2ZnSnSe_4$

CZTSe absorber for this study was prepared by reactive thermal annealing of metallic precursor stack deposited by DC magnetron sputtering onto Mo coated soda lime glass substrates, as described elsewhere in more detail [64]. The CZTSe absorber composition was measured by X-ray florescence spectroscopy, showing relative cation composition of Cu=38.0%, Zn=36.7% and Sn=25.3%, which results in cation ratios of Cu/(Zn+Sn)=0.61, Zn/Sn= 1.45, Cu/Zn=1.04, and Cu/Sn=1.5. Highest device performance is reported in this Cu poor Zn rich compositional range and recently even for very Cu poor absorber layers performant devices with especially high Voc values are reported in [84]. Solar cells were finished by depositing a CdS buffer layer by chemical bath deposition followed by DC-pulsed sputtered ZnO (50nm) and In_2O_3 :SnO_2 (90/10 wt.%; 350 nm, $R_{\square}$=50 Ωcm^{-1}) window layer. Prior to CdS deposition, the CZTSe absorber was etched using an oxidizing etching to remove possible ZnSe secondary phases from the surface, as reported in [64]. The compositional values presented here were measured prior to the specific surface etching because the time between surface etching and buffer layer deposition is crucial to avoid surface contamination. Thus, a reduction in Zn composition is expected in the final CZTSe absorber layer. The individual solar cell used for this study shows a power conversion efficiency of η = 6.6% with J_{sc} = 28.3 $mAcm^{-2}$, V_{oc} = 368 mV, and FF = 63%.

4. RESULTS AND DISCUSSION

4.1 Photoreflectance of $AgGaTe_2$ single crystal

The detailed growth procedure of monocrystalline $AgGaTe_2$ was described in Section 3. Raman spectra confirm the monophase of $AgGaTe_2$ single crystal. Single crystal surfaces sized about 2x2 mm were freshly cleaved from the ingot for PR measurements.

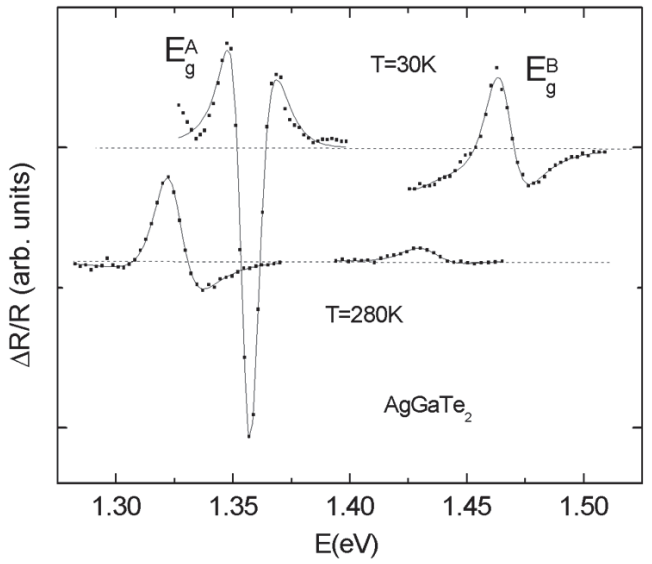

Figure 19. Photoreflectance spectra of the $AgGaTe_2$ crystal at different temperatures. Continuous lines represent the fitting results. A and B bandgaps are clearly resolved.

At low temperature T=30 K, we detected very strong derivative like a lineshape in the recorded PR spectra of AGT around 1.35 eV and not so well pronounced but still relatively strong spectra around 1.46 eV, see Fig. 19. The two photoreflectance transitions obtained indicate two bandgap energies of the studied crystals. It has been reported that in $AgGaTe_2$ valence band splitting up to three subzones appears [24], the splitting of valence band is common to the ternary I-III-VI semiconductor compounds with a chalcopyrite structure [24]. After fitting these results with Lorenzial third derivative functional form Eq. (14), we obtained bandgap energies at low temperature of 1.355 and 1.466 eV; unfortunately, the third bandgap did not appear, which has been reported by other authors [23, 24].

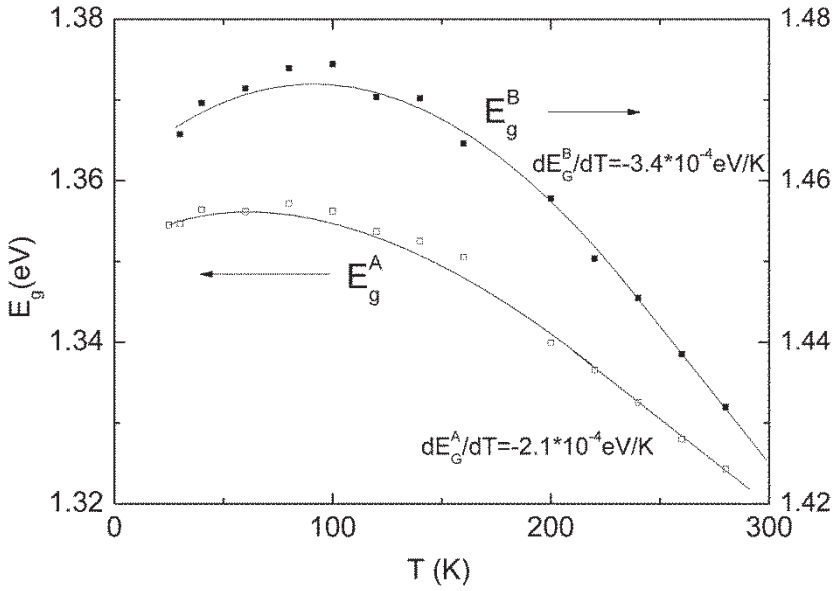

Figure 20. Temperature dependence of A and B bandgap energies of $AgGaTe_2$ crystal obtained from photoreflectance spectra. At higher temperatures, nearly linear dependence can be observed.

All PR measurements were made at T=25–295 K. From these measurements, after fitting with Eq. (14), E_g^A and E_g^B were found and the results are presented in Fig. 20. It can be seen that both bandgap energies have a maximum at about T=90 K. This behavior is typical of ternary compounds containing Ag and the same kind of behavior in AGT was also observed by Bodnar et al. [25]. It is suggested that this trend can be due to the effects of lattice dilation and electron–phonon interaction. At the same time, the temperature dependence of bandgap energies found by Arai et al. [65] showed no maximum. At higher temperatures, the temperature dependence of bandgap energies shows a nearly linear trend, but the rate of this trend is different for different bandgaps (see Fig. 20). The lowest bandgap energy at room temperature E_g^A=1.320 eV shows a temperature coefficient dE_g^A/dT= -2.1x10^4 eV/K, which is very close to the value 2.02x10^4 eV/K found by Bodnar et al. [25]. The next bandgap energy was E_g^B=1.425 eV and the temperature coefficient dE_g^B/dT= -3.4x10^4 eV/K. The temperature coefficients found by Arai et al. [65] for their A–C bandgaps are all in the range dE_G/dT=-(2.4–2.6)x10^4 eV/K. The bandgap energy maximum was around T=90 K with values E_g^A=1.357 eV and E_g^B=1.474 eV.

4.2 Electroreflectance of CdTe solar cells

The fabrication procedure and conditions of thin film CdS/CdTe solar cells are described in Section 3. It was surprising that the solar cells fabricated in similar conditions showed huge differences in their performance. One of the reasons probably lies in the p-n junction formation.

Temperature dependent ER measurements are shown in Figs. 21 and 22 for Cell 1 and Cell 2, respectively. Dots represent experimental data and the continuous line fitting with Eq. (14). A good blueshift of the spectrum related to the bandgap energy shift from the temperature is seen. In addition to the temperature decrease, the intensity of the ER signal increases, see scale factors from Figs. 21 and 22; it is related to the change in magnitude of the electric field in the junction.

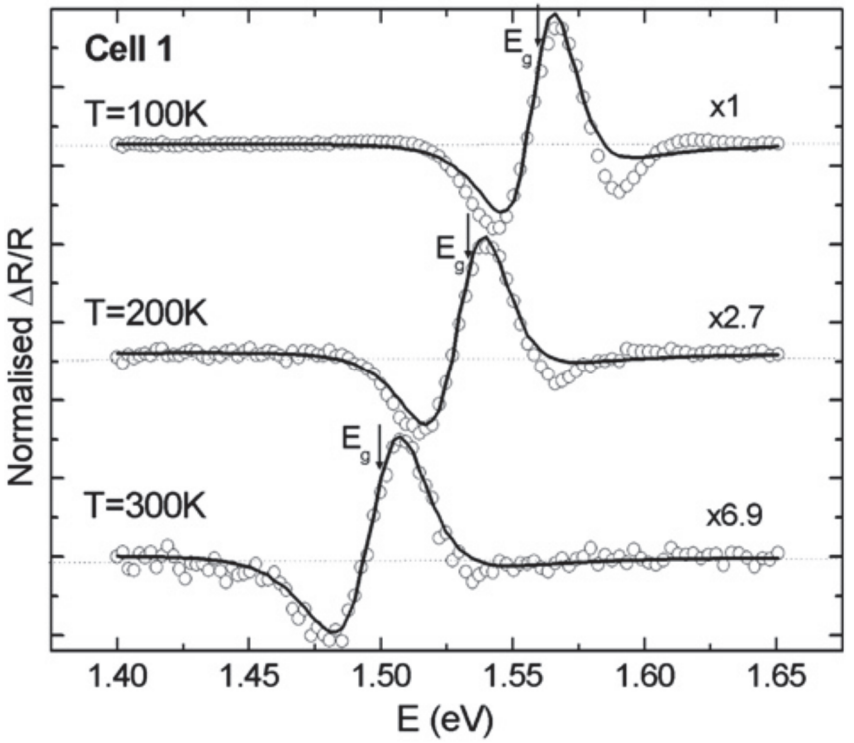

Figure 21. ER spectra of sample Cell 1 at 100 K, 200 K and 300 K. Dots show experimental results and continuous lines are the fitting results with Eq. (14).

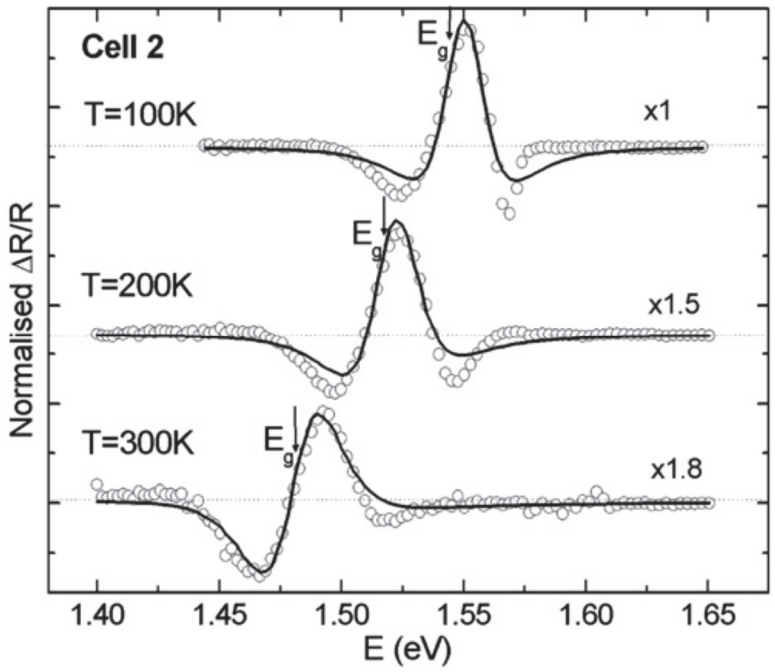

Figure 22. ER spectra of sample Cell 2 at 100 K, 200 K and 300 K. Dots show experimental result and continuous lines are the fitting results with Eq. (14).

Temperature dependence of bandgap energies obtained from the fittings with Eq. (14) is plotted in Fig. 23. E_g values are considerably lower than the reported reference values of monocrystalline CdTe, see Fig. 23 [66]. Temperature coefficients were found to be $dE_g/dT = -3.1\times10^{-4}$ eV/K for Cell 1 and $dE_g/dT = -3.5\times10^{-4}$ eV/K for Cell 2. These values are in good agreement with the results obtained by Mathew et al. [67].

The bandgap energies obtained are smaller than those found for monocrystalline CdTe in other papers [66, 68]. Smaller bandgap energies in our cells can be explained by assuming that $CdTe_{1-x}S_x$ solid solution was formed in the p–n junction region. Sulfur has incorporated into CdTe during the thermal treatment. Hädrich et al. [69] have found that the dependence of the bandgap energy of the $CdTe_{1-x}S_x$ solid solution is expressed by the following empirical equation:

$$E_G(x) = 2.4x + 1.51(1-x) - 1.8x(1-x) \ . \qquad (23)$$

The equation enables us to calculate sulfur value in $CdTe_{1-x}S_x$ solid solution from the values of room temperature bandgap. We found bandgap energies at

room temperature E_g=1.499 eV and E_g=1.481 eV for Cell 1 and Cell 2, respectively. According to Eq. (23), we have a $CdTe_{1-x}S_x$ solid solution with an average sulfur content of x=0.01 for Cell 1 and x=0.03 for Cell 2. It is obvious that the solid solution layer has no abrupt edge and probably we have a layer with varying concentration of sulfur. Cell 1 with lower sulfur content in the solid solution showed a better solar cell performance, as shown by I–V measurements in Section 3. Similar behavior was described also by Hädrich et al. [69].

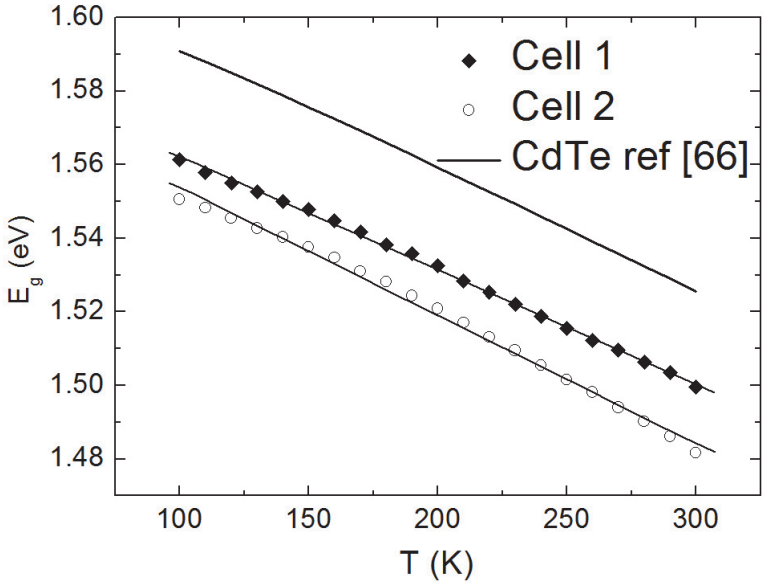

Figure 23. CdTe bandgap energy values as a function of temperature found from ER fittings. The upper curve represents the bandgap energy of monocrystalline CdTe from [66].

The broadening parameter Γ is often used as a measure of crystal quality since its magnitude is primarily determined by lattice defects such as disorders, vacancies, and impurities [33]. In our experiment, as shown in Fig. 24, Γ was found to be 29 meV for Cell 1 and 27 meV for Cell 2 at room temperature and it is decreasing with the temperature falling. From the comparison of our results with those of other authors, it can be concluded that CdTe samples with a broadening parameter value around 30 meV and less can be classified into good quality sample category [70].

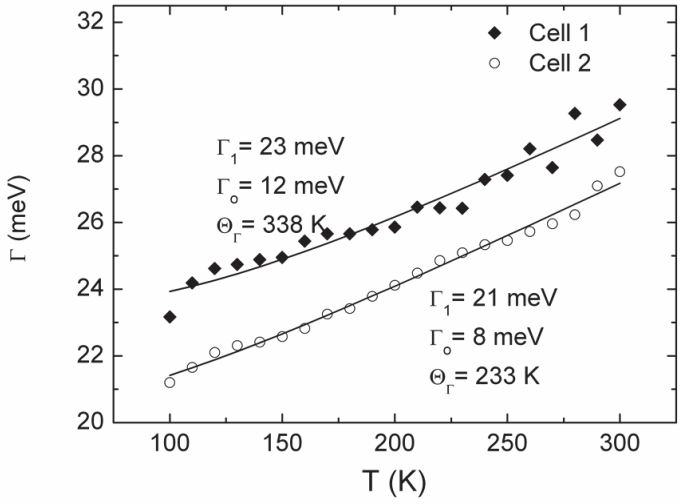

Figure 24. The temperature dependence of the broadening parameter Γ with fittings (solid curves) using Eq. (24). Fitting parameter Γ_1 represents the broadening due to the temperature-independent mechanism, Γ_0 shows the strength of electron–phonon coupling and Θ_Γ is an average phonon temperature.

The effect of temperature provides not only the shift of the bandgap energy but also the change in the broadening parameter. If we grant the electron–phonon coupling as a main broadening mechanism, its parameter value can be written by taking into account the Bose–Einstein occupation factor, as in [71]:

$$\Gamma(T) = \Gamma_1 + \left(\frac{\Gamma_0}{e^{\Theta_\Gamma / T} - 1} \right), \tag{24}$$

where Γ_1 represents the broadening due to temperature-independent mechanisms, such as crystalline imperfections and surface scattering, Γ_0 represents the strength of electron–phonon coupling, Θ_Γ is an average phonon temperature. Fig. 24 shows the ER broadening parameter Γ as a function of temperature and least-squares fit (solid curves) with Eq. (24) together with fitting parameters. The obtained Γ_1 values of 23 meV and 21 meV for samples Cell 1 and Cell 2, respectively, indicate relatively high quality of the CdTe thin film. Calculated values of Γ_0=12 meV and Θ_Γ=338 K for Cell 1 and Γ_0=8 meV and Θ_Γ=233 K for Cell 2 are comparable for both solar cells. It is interesting that a lower efficiency solar cell shows also a lower value of Γ_1. This difference between broadening parameters could also be an important factor in the properties of the respective p–n junction.

4.3 Photoreflectance of SnS monocrystals

The detailed growth procedure of monocrystalline SnS was described in Section 3. As already mentioned, the single crystals of SnS had platelike shape with a good reflecting surface, sized approximately 3x3 mm. The sample showed very well pronounced PR spectrum at low temperature and was recordable up to 200 K, at higher temperatures, the PR signal quenches.

Temperature dependent measurements of SnS single crystals show visible blueshift due to the change in the bandgap energy depending on the temperature, also intensity decreases as observed from scale factors (Fig. 25). Each PR spectrum was analyzed by fitting the data to a low-field lineshape function with a third-derivative functional form Eq. (14) from Section 2.

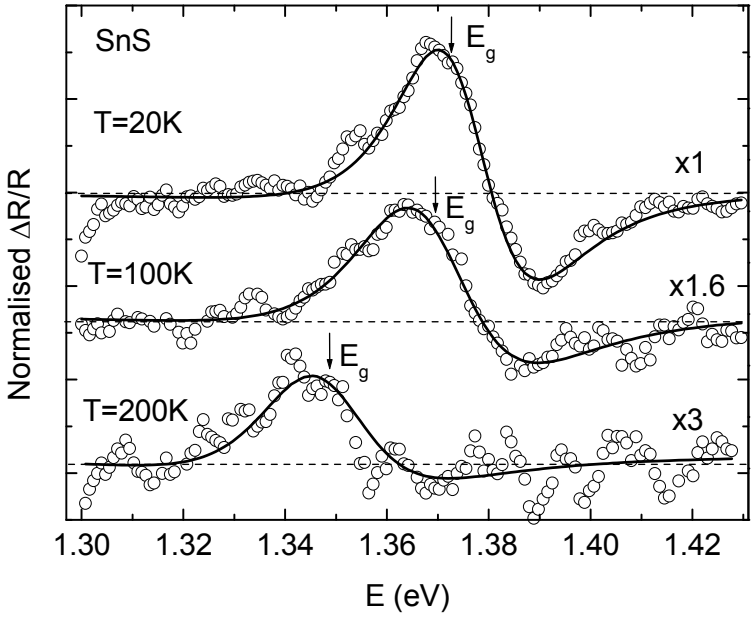

Figure 25. Temperature dependent PR spectra of a SnS single crystal. Circles show experimental results and continuous lines are fitting the results with Eq. (14).

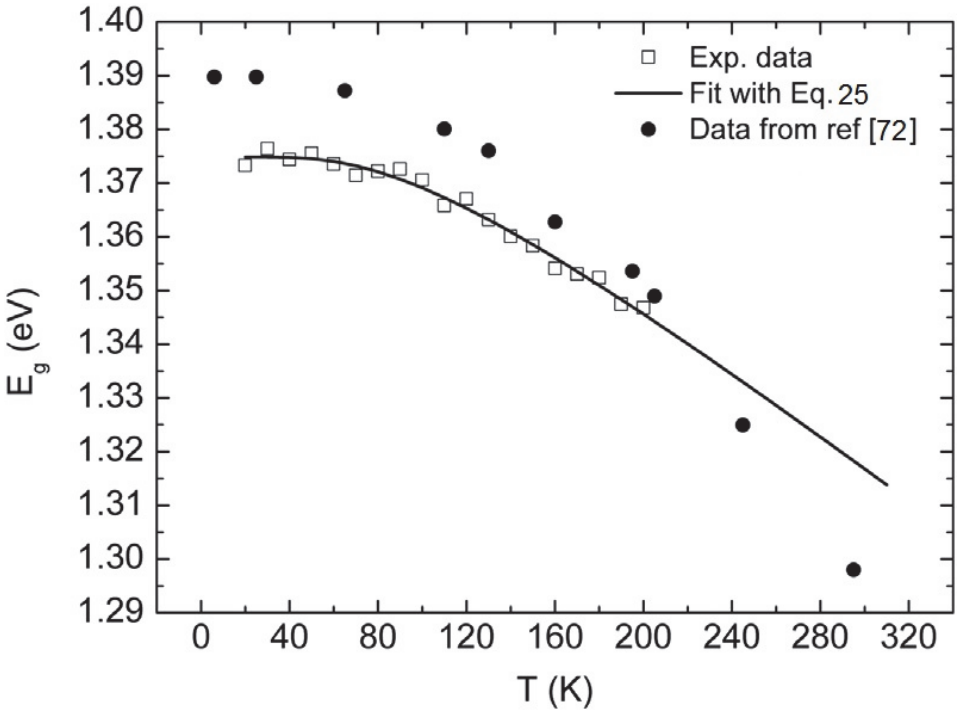

Figure 26. Bandgap energy values for single-crystal SnS determined by fitting the PR spectra as a function of temperature, the data fit to Eq. (25), and data reported by Parenteau and Carlone [72].

Temperature dependence of the SnS bandgap energies obtained by fitting PR spectra are plotted in Fig. 26. Obtained experimental data were fitted to the O´Donell expression [73]:

$$E_g(T) = E_g(0) - S < \hbar\omega > \left[\coth(< \hbar\omega > / 2kT) - 1\right] \qquad (25)$$

where $E_g(0)$ is the bandgap energy at 0 K, S is a dimensionless coupling constant and $<\hbar\omega>$ represents an average phonon energy. Obtained fitting parameters were $E_g(0)$ = 1.375 eV, S = 1.86 and $<\hbar\omega>$ = 24.3 meV. By extrapolating the fitting result to the O′Donnell equation for higher temperatures it is possible to estimate the bandgap energy at room temperature, resulting in E_g =1.317eV. The average phonon energy of $\langle\hbar\omega\rangle$= 24.3 meV =196 cm^{-1} is very close to the value of 191 cm^{-1} measured by Raman spectroscopy in Section 3.

Fig. 26 also shows the temperature dependence of the bandgap energy for SnS obtained by Parenteau and Carlone [72] for comparison. The comparison reveals differences in the bandgap energy values and their temperature-dependent behavior. The reason for this discrepancy may lie in the different samples and measurement methods. Parenteau and Carlone applied optical absorption for bandgap studies [72], while we used PR.

4.4 Photoreflectance of Cu_3BiS_3 thin film

The detailed growth procedure of polycrystalline Cu_3BiS_3 was described in Section 3. XRD spectra confirm the existence of a single phase Cu_3BiS_3.

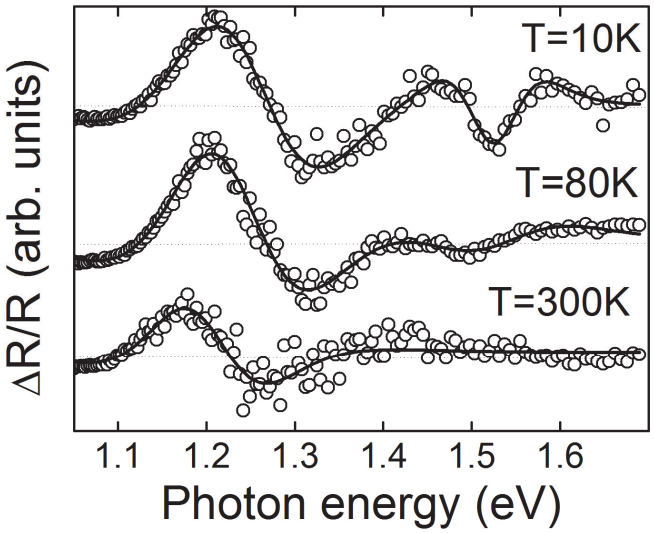

Figure 27. Temperature dependent PR spectra of Cu_3BiS_3 single crystal. Circles show experimental results and continuous lines are fitting the results with Eq. (14).

Fig. 27 shows room temperature PR spectra, which demonstrate a strong resonance at 1.2 eV. Decreasing the temperature down to 80 K shifts this resonance towards higher energies and reveals a second resonance at 1.5 eV. Further decrease of temperature, down to 10 K, shifts the resonances further towards higher energies and makes both resonances sharper, as shown in Fig. 27. The experimental PR spectra were fitted with Eq. (14). The fitted curves for the temperature 10, 80 and 300 K are shown by solid lines in Fig. 27.

Values for E_g for different temperatures determined using the best fits are shown in Fig. 28. The presence of two band gaps can be associated with splitting of the valence band. Such splitting has been reported for ternary I–III–IV_2 semiconductor compounds with chalcopyrite structure [74]. Measurements on $AgInS_2$, a semiconductor compound, which crystallizes in two different phases, chalcopyrite and orthorhombic, reveal a splitting of the valence band into three sub-bands for both of them [75]. In the chalcopyrite phase, splitting into A, B and C sub-bands occurs due to the simultaneous influence of the crystal field and spin orbit interaction whereas in the orthorhombic one splitting into X, Y and Z sub-bands is considered to be solely due to the influence of the crystal field. In the orthorhombic structure of Cu_3BiS_3, we use the notations X and Y for the top two bands.

The temperature dependencies of E_g^X and E_g^Y were fitted with the expression introduced by O'Donnell and Chen [73]:

$$E_g(T) = E_g(0) - S<\hbar\omega>\left[\coth(<\hbar\omega>/2kT) - 1\right] \quad (26)$$

where $E_g(0)$ is the bandgap energy at 0 K, S is a dimensionless coupling constant and $<\hbar\omega>$ represents an average phonon energy. The solid curves in Fig. 28 are the best fits of the $E_g(T)$ values using Eq. (26) with the fitting parameters shown in Table 3. The determined average phonon energies are in the range of the measured energies of the Raman modes, reported in Section 3. Fig. 28 demonstrates a strong decrease of both energy gaps with an increasing temperature, so at room temperature E_g^X = 1.18 eV. A reduction in the splitting of the valence bands from 0.28 eV at 10 K to 0.27 eV at 100 K can also be observed. Low temperature T=10 K values for bandgap energies were E_g^X =1.24 eV and E_g^Y =1.53 eV.

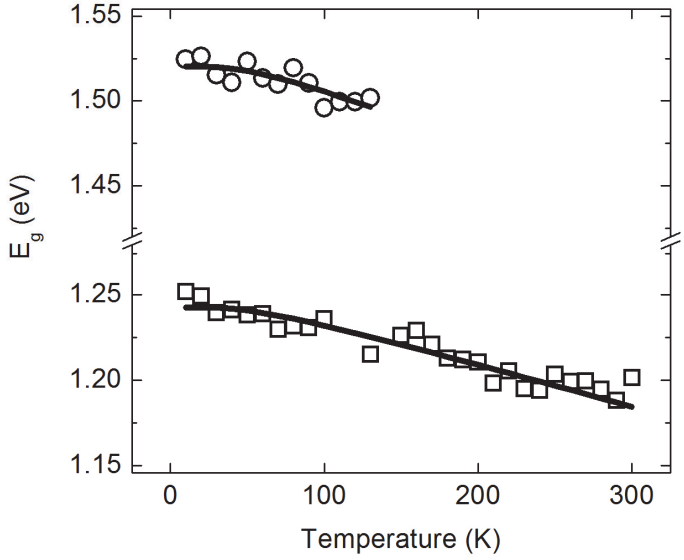

Figure 28. Bandgap energy values of Cu_3BiS_3 single crystal found from PR fittings as a function of temperature, together with fittings.

Table 3. The bandgap E_g, coupling constant S and average phonon energy $<\hbar\omega>$ for the X and Y valence bands determined by fitting the experimental temperature dependencies of E_g using Eq.(26).

Valence band	**E_g (0), eV**	**S**	**$<\hbar\omega>$, meV**
X	1.24	0.54	6
Y	1.53	0.70	20

4.5 Electroreflectance of $Cu_2ZnSnSe_4$ solar cells

The CZTSe solar cell fabrication procedure was described in detail in Section 3.

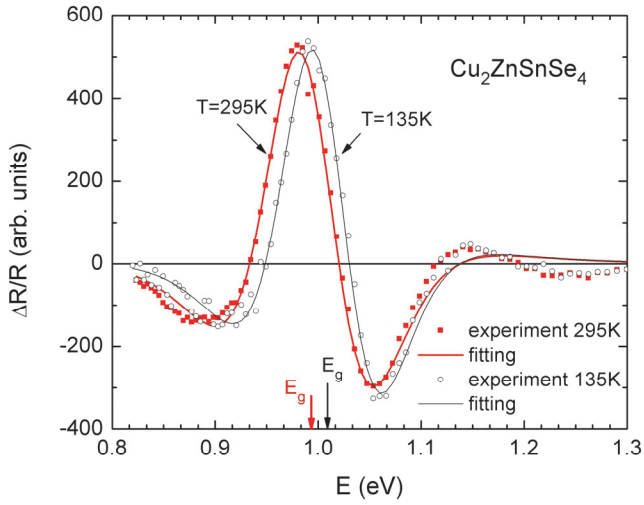

Figure 29. ER spectra of CZTSe solar cell at 135 K and 295 K. Dots show the experimental data and continuous lines are the fitting results with Eq. (14).

Temperature dependent ER spectra together with Aspnes fit (Eq. (14)) of CZTSe cell are presented in Fig. 29. It is clearly seen that the spectrum shifts towards higher energies with decreasing temperature, but the shift is very small and the shape of ER peak remains relatively unaffected. This means that the linewidth is determined by the inhomogeneous broadening. Although the spectral fit with Eq. (14) gives good results near the critical point, we still notice some deviation at higher energies, see Fig. 29. This deviation could be an indication of a second critical point at higher energy. For example, in [76] the room temperature $E_0(C)$ bandgap of CZTSe due to spin-orbit splitting of valence band was found at 1.272 eV. However, our ER signal was too low near this energy and therefore we fitted only the main peak. The overall shape of the main peak is determined by a high concentration of charged defects and spatial fluctuations of the band edge in this compound. As a result, the dielectric function will be affected and inhomogeneous broadening mechanisms start to dominate. Moreover, the best fit was achieved using remarkably high m values $m \geq 3$. However, according to our calculations, the exponent m mostly determines the line-shape of the ER spectrum far from a critical point and does

not affect the spectrum near the bandgap energy E_g. An average value of the broadening parameter $\Gamma \approx 125$ meV is practically constant over the whole temperature range. One of the possible explanations is that not only potential fluctuations, but also the bandgap energy fluctuations due to presence of ordered and disordered structures and/or different defect clusters [77, 78, 79] are affecting the inhomogeneous broadening. Very similar bandgap energy fluctuations were discovered by PL in the ternary compound $CuGa_3Se_5$ [28] and, as a rule, they lead to an abnormal widening of PL and ER bands. Therefore, the bandgap energy E_g obtained from ER fittings always represents some average value. Very wide room temperature ER spectra were measured also in CZTSSe by Krämmer et al. [80]. They noticed that due to inhomogeneous broadening mechanisms, the resulting modulus spectra calculated from ER experiments could be better fitted with a Gaussian lineshape instead of Lorentzian. It seems that this inhomogeneous broadening due to spatial bandgap energy and potential fluctuations is a typical feature in all kesterites and does not depend on the bandgap energy. Unfortunately, ER measurements were not possible at $T <$ 100K because the ER signal dropped significantly. At low temperatures, holes start to localize in the valence band potential wells and as a result, the series resistance of the solar cell increases considerably [81, 82]. This leads to a reduction of an external electric field on a junction and accordingly, the ER signal drops.

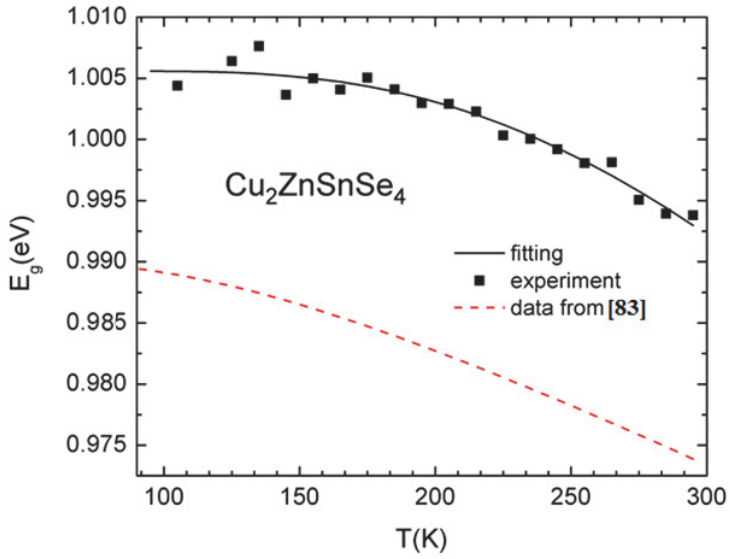

Figure 30. Bandgap energy values found from ER fittings as a function of temperature. Solid curve is a fitting result with Eq. (27). The dashed curve represents the bandgap energy of CZTSe according to data from [83].

The resulting band gap values for the CZTSe cells are shown in Fig. 30. The temperature dependence of E_g was fitted with the expression introduced by O'Donnell and Chen [73]:

$$E_g(T) = E_g(0) - S < \hbar\omega > \left[\coth(< \hbar\omega > / 2kT) - 1\right], \qquad (27)$$

where $E_g(0)$ is the band gap energy at 0 K, S is a dimensionless coupling constant and $<\hbar\omega>$ represents an average phonon energy. The solid curve in Fig. 30 is the best fit of the $E_g(T)$ values using Eq. (27) with the fitting parameters $E_g(0)$=1.006 ± 0.001 eV, S=2.0 ± 0.6 and $<\hbar\omega>$ = 85 ± 13 meV. The overall shift of E_g is only about 13 meV from room temperature to T= 0 K. Somewhat greater shift was found by Choi et al. [83], see Fig. 30. Bandgap value of the CZTSe absorber at room temperature was 0.993 eV.

CONCLUSION

Different types of new and prospective solar cell absorbers were studied using temperature dependent modulation spectroscopy techniques, namely photoreflectance and electroreflectance. These methods prove their advantages in the study as simple and nondestructive techniques, while the obtained information is relatively wide. We found precise bandgap energies to the studied samples from the measured spectra and clarified some mismatches about the physical and optoelectronic properties of the materials.

1. Temperature dependent photoreflectance study was preformed to $AgGaTe_2$. In the studied $AgGaTe_2$ monocrystal valence band, splitting was detected, however only two bandgaps were identified; unfortunately, we were unable to detect the third bandgap reported in the literature. At room temperature, the lowest bandgap energy was found to be E_g^A= 1.320 eV with the temperature coefficient $dEg_A/dT = -2.1x10^4$ eV/K. Higher room temperature bandgap energy was detected at E_g^B=1.425 eV with the temperature coefficient $dEg_B/dT=3.4x10^4$ eV/K. The bandgap energies showed maximum around T=90 K with values E_g^A=1.357 eV and E_g^B=1.474 eV. This kind of behavior is quite usual to the Ag containing ternaries.

2. Two CdS/CdTe solar cells were studied with temperature dependent electroreflectance spectroscopy. Room temperature bandgap energies were E_g=1.499 eV for Cell 1 (efficiency 9.6%) and E_g=1.481 eV for Cell 2 (efficiency 4.1%). The low value of the broadening parameter Γ for both solar cells shows a good quality of CdTe absorber layers. The formation of $CdTe_{1-x}S_x$ solid solution in the p–n junction region was detected for both solar cells. The sulphur value was found to be x=0.01 and x=0.03 for Cell 1 and Cell 2, respectively. However, Cell 2 had smaller broadening parameter value, but Cell 1 showed a better solar cell performance

3. Monocrystalline SnS was investigated with photoreflectance spectroscopy in the temperature range of 20–200 K. The temperature dependence of the bandgap energy was fitted using the O′Donnell expression. The O′Donnell model gave a room-temperature bandgap estimate of 1.317 eV.

4. Temperature dependent photoreflectance study was preformed to thin film Cu_3BiS_3. At low temperature T=10 K, two bandgap energies were detected with the values of E_g^X=1.24 eV and E_g^Y=1.53 eV, which are attributed to the valence band splitting. At room temperature, only one bandgap energy was detected E_g^X=1.18 eV.

5. Temperature dependent electroreflectance analysis was done to the $CdS/Cu_2ZnSnSe_4$ solar cell. The bandgap energy shift was very small from room temperature to 0 K only 13 meV, from 0.993 to 1.006 eV, respectively. High values of the broadening parameter Γ=125 meV are related to the high concentration of charged defects and spatial fluctuations of the bandgap energy caused by the presence of both ordered and disordered structures and/or different defect clusters in CZTSe.

ACNOWLEDGEMENT

I would like to express my greatest gratitude to my supervisors Professor Jüri Krustok and Senior Research Scientist Maarja Grossberg for their support, guidance and useful discussions over the years of my studies.

I would also like to thank Prof. Enn Mellikov, Head of the Department and Materials Science and Dr. Marit Kauk-Kuusik for the opportunity to join and work in the research group at the Chair of Materials Science; and Prof. Andres Öpik, the Director of the Doctoral school ”Functional materials and technologies” for providing the opportunity to participate in the PhD school.

I am very thankful to all colleagues in the lab for their support and guidance, especially PhD students Mati Danilson, Maris Pilvet, Erkki Kask, scientists Dr. Kristi Timmo, Dr. Mare Altosaar, Dr. Tiit Varema, Dr. Liina Kaupmees, Dr. Valdek Mikli, Dr. Erki Kärber, Dr. Rainer Traksmaa, Dr. Jaan Hiie, Dr. Raavo Josepson, and Dr. Vello Valdna for useful discussion and help.

My special thanks go to Dr. Jaan Raudoja and PhD student Nickolae Spalatu from TUT and Dr. Mike V. Yakushev from the University of Strathclyde, Glasgow and Dr. Edgardo Saucedo from Catalonia Institute for Energy Research for providing me with samples for studies.

This work was financially supported by Estonian Ministry of Education and Research IUT19-28 and SF0140099s08; Estonian Science Foundation grants G-8282, G-9369 and G-9425; Estonian Center of Excellence in Research “High-technology Materials for Sustainable Development” (´project TAR 11059) and TK117T; Estonian national program in new energy technologies (project AR 12128 and AR 10128); graduate school “Functional materials and technologies”. This project has received funding from the European Union’s Seventh Programme for research, technological development and demonstration under grant agreement No 609788.

My warmest gratitude is due to my family, my wife Tiia and sons Alfred and Hans Harald for their encouragement and support. Also, my parents Mall and Peeter are gratefully acknowledged.

ABSTRACT

This thesis is focused on the application of temperature dependent photo- and electroreflectance spectroscopy in order to study novel and potential materials in solar energy conversion. Photoreflectance and electroreflectance belong to the modulation spectroscopy techniques, where during reflectance measurements, the external modulation is applied in respect to one system parameter. Within the techniques used in this thesis, the periodically modulated parameter was the built-in surface/internal electric field. Changes in the electric field cause changes in the complex dielectric function and this in turn is directly related to the material reflectance ability. The recorded modulated reflectance spectra had a nature of a third derivative near the interband transitions. These methods allowed us to estimate the bandgap energy of studied materials with relatively high precision, and additionally to evaluate the quality of crystals. The main advantage of photo- and electroreflectance spectroscopies over other optical characterization techniques is that they are nondestructive, simple, applicable at room temperatures and high precision. My study included $AgGaTe_2$, SnS and Cu_3BiS_3 materials with photomodulation and CdTe and CZTSe solar cells with electromodulation. As a result, proper bandgap energies of the materials were found and their behavior depending on thetemperature was described.

In $AgGaTe_2$ monocrystal valence band splitting was detected and two bandgap energies were found with room temperature values E_g^A= 1.320 eV and E_g^B=1.425 eV. Maximum energies were around T=90K E_g^A=1.357 eV and E_g^B=1.474 eV.

Monocrystalline SnS bandgap energy value was found from PR spectra in the temperature range of 20–200 K. Above 200 K, PR signal vanished and O′Donnell's model was used to estimate a room-temperature bandgap value that was found to be 1.317 eV. Highest measured bandgap energy 1.377 eV was detected at T=30 K.

In a polycrystalline Cu_3BiS_3 thin film, valence band splitting at low temperature T=10 K was detected and two bandgap energies were found atvalues of E_g^X=1.24 eV and E_g^Y=1.53 eV. At room temperature, only lower bandgap energy was found E_g^X=1.18 eV.

Room temperature bandgap energies for CdS/CdTe solar cells were found to be E_g=1.499 eV and E_g=1.481 eV for Cell 1 and Cell 2, respectively. The formation of $CdTe_{1-x}S_x$ solid solution in the p–n junction region was detected for both solar cells. The sulphur value was found to be x=0.01 and x=0.03 for Cell 1 and Cell 2, respectively.

Kesterite $Cu_2ZnSnSe_4$ solar cell showed very small bandgap energy shift from temperature, only about 13 meV from room temperature to 0 K. The value of broadening parameter $\Gamma=125\ meV$ was relatively high, indicating a high concentration of charged defects and spatial fluctuations of the bandgap energy.

KOKKUVÕTE

Antud töö on keskendunud uute ja perspektiivsete päikesepatareides kasutatavate pooljuhtmaterjalide uurimisele fotopeegeldus- ja elektropeegeldusspektroskoopia meetoditel. Need meetodid kuuluvad modulatsioonspektroskoopia valdkonda, kus mingi parameetri mõõtmise ajal moduleeritakse välismõjutajat. Antud töös kasutati sisseehitatud elektrivälja modulatsiooni materjali dielektrilise funktsiooni muutmiseks, mis otseselt mõjutab uuritava materjali peegeldusvõimet. Elektrivälja modulatsiooni mõju avaldub peegeldusspektri kolmanda tuletise kujus kohal, kus toimuvad tsoonidevahelised üleminekud. Kasutatud meetodid võimaldavad suhteliselt täpselt määrata uuritavate pooljuhtmaterjalide keelutsooni laiuse väärtusi ja hinnata uuritavate materjalide kvaliteeti. Fotopeegeldus- ja elektropeegeldusspektroskoopia meetodite eeliseks on nende suhteline lihtsus, suur täpsus ja rakendatavus toatemperatuuril mõõtmisobjekti kahjustamata.

Antud töös uuriti hõbegalliumtelluriidi ($AgGaTe_2$), tinasulfiidi (SnS) ja vaskvismutsulfiidi (Cu_3BiS_3) fotopeegeldusspektroskoopia meetodil ja kaadmiumtelluriidi (CdTe) ning vasktsinktinaseleniidi ($Cu_2ZnSnSe_4$) elektropeegeldusspektrosoopia abil. Töö tulemusena leiti täpsustatud keelutsooni laiuste väärtused ja nende muutused sõltuvalt temperatuurist. $AgGaTe_2$ monokristalle uurides leiti kinnitus asjaolule, et selle materjali keelutsoon on lõhenenud ja nende kahe keelutsooni laiuseks määrati toatemperatuuril E_g^A=1,320 eV ja E_g^B=1,425 eV. Avastati, et keelutsoonide laiused suurenevad temperatuuri vähenemisel allapoole toatemperatuuri kuni 90K-ni, kus nad saavutavad kõrgeimad väärtused vastavalt E_g^A=1,357 eV ja E_g^B=1,474 eV. Edasisel temperatuuri langusel keelutsoonide väärtused vähenevad taas.

Monokristalse tinasulfiidi keelutsooni väärtuse muutust uuriti fotopeegeldusspektroskoopia meetodil temperatuuride vahemikus 20-200K. Kõrgematel temperatuuridel fotopeegelduse signaal kadus ja SnS keelutsooni laiuse hindamiseks kõrgematel temperatuuridel kasutati O'Donelli lähenduse mudelit, mille abil leiti tinasulfiidi toatemperatuurseks keelutsooni väärtuseks 1,317 eV. Tinasulfiidi keelutsooni laius oli kõige suurem 30K juures: 1,377 eV.

Polükristalses Cu_3BiS_3-s avastati valentstsooni lõhenemine madalatel temperatuuridel, kasutades fotopeegeldusspektroskoopia meetodit. Keelutsoonide laiuse väärtus 10K juures leiti E_g^X=1,24 eV ja E_g^Y=1,53 eV. Toatemperatuuril oli võimalik määrata vaid ühe keelutsooni laiuse väärtus - E_g^X=1,18 eV.

CdTe keelutsooni laius määrati kahes CdS/CdTe päikesepatarei struktuuris elektropeegeldusspektroskoopia abil, kusjuures CdTe keelutsooni laiuseks toatemperatuuril saadi nendele erinevad tulemused: E_g=1,499 eV ja E_g=1,481. Kuna saadud väärtused on väiksemad kui kirjandusest leitud monokristallilise CdTe keelutsooni laius, siis järeldati, et CdS/CdTe struktuurides olid *p-n* siirde piirkonnas tekkinud erineva koostisega CdS_xTe_{1-x} tahked lahused x väärtustega x=0,01 ja x=0,03. Madaltemperatuursed

keelutsooni laiused mõlemale päikesepatareile olid vastavalt 1,561 eV ja 1,551 eV.

Kesteriitse päikesepatarei absorbermaterjali $Cu_2ZnSnSe_4$ keelutsooni laiuse muutus toatemperatuurilt kuni temperatuurini T = 0 K oli kõigest 13meV. Lähendusparameetri Γ võrdlemisi suur väärtus 125meV viitab suurele laetud defektide hulgale ja keelutsooni ruumilistele fluktuatsioonidele.

REFERENCES

1. Adrew Fairbrother, PHD theses. Development of $Cu_2ZnSn(SSe)_4$ based solar cells (2014).
2. K. Muska, PhD Thesis. Study of Compostion and Thermal Treatments of Quaternary Compounds for Monograin Layer Solar Cells (2012).
3. IRENA Volume 1: Power sector Issue 4/5.
4. M.A. Green, The path to 25% silicon solar cell efficiency: History of silicon cell evolution, Prog. Photovolt: Res. Appl.,17 (2009) 183-189.
5. William Shockley and Hans J. Queisser, Detailed Balance Limit of Efficeiency of p-n Junction Solar Cells, *Journal of Applied Physics*, Volume 32 (March 1961) 510-519.
6. Solan Chetan Singh, Solar photovoltaic: Fundamental, Technology and Application, New Dehli PHI Learning 2011.
7. P. A. Nwofe, PhD Thesis. Deposition and Characterisation of SnS Thin Films for Application in Photovoltaic Solar Cell Devices (2013).
8. IEA International Energy Agency, "Trends 2014 In photovoltaic application" (2014).
9. PV Magazine, Modul price Index, 2014. [Online] Available http://www.pv-magazine.com/investors/module-price-index/#axzz3ZvKElTC6.
10. T. S. Moss, Optical Absorption Edge in GaAs and Its Dependence on Electric Field, J. Appl. Physics 32 (10) (1961) 2136-2139.
11. B. O. Seraphin, Electroreflectance, Journal de Physique 28 (C3) (1967) 73-80.
12. B. O. Seraphin, Proceedings of the International Conference on the Physics of Semiconductors, Paris, 1964 (Dunod, Paris, 1964) 165-.
13. E.Y. Wang, T Nohara, H Ishii, H Hoshino, K Takahashi, II-VI Semiconducting Compounds 1967 International Conference, (1967) 136-141.
14. Photoreflectance spectroscopy of low dimensional semiconductor structures (2012) Available: http://nano.if.pwr.edu.pl/materialy_do_zajec/instrukcja_pr_s.pdf.
15. A. Patane, N. Balkan, Semiconductor Research, Springer Series in Material Science 150, (2012) 95-124.
16. F. H. Pollak, O. J. Glembocki, Modulation spectroscopy of semiconductor microstructures: an overview, SPIE 946 (1988) 2-35.
17. J. Misiewicz, P. Sitarek, G. Sek, Photoreflectance spectroscopy of low dimensional semiconductors structures, Opto-electronics review 8 (1), (2000) 1-24.
18. C. Skierbiszewski, Experimental studies of the conduction –band structure of GaInNAs alloys, Semiconductor Science and Technology 17 (8) (2002) 803-814.

19. A. Patane, N. Balkan, Semiconductor Research. Experimental Techniques, Springer Series in Material Science 150 (2012) 95-124.
20. R. Henninger, J. Klaer, K. Siemer, J. Bruns, D. Bräunig, Electroreflectance of $CuInS_2$ thin film solar cells and dependence on process parameters, J. Appl. Phys. Vol. 89 (5) (2001) 3049-3054.
21. Andri Jagomägi, PhD Thesis. Photoluminescence of Chalcopyrite Tellurides (2006).
22. "Solar Froniter," (2014) [Online]. Available: http://www.solar-frontier.com/eng/news/2014/C031367.html
23. I. V. Bodnar, V. F. Gremenok, R. V. Martin, O. N. Obraztsova, M. V. Yakushev, A.E. Hill, R. D. Pilkington, R. D. Thomlinson, Photoluminescence of $AgGaTe_2$ single crystals, J. of App. Spec. 67 (2) (2000) 303-309.
24. B. Tell, J.L. Shay, H.M. Kasper, Some properties of $AgAlTe_2$, $AgGaTe_2$, $AgInTe_2$. Phys. Rev. B 9, 12 (1974) 5203-5208.
25. I. V. Bodnar, V. F. Gremenok, I. A. Viktorov, O. N. Obraztsova, Investigation of the optical properties of $AgGaTe_2$ films obtained by lased deposition, J. of App. Spec. 64 (6) (1997) 809-813.
26. J. Krustok, M. Grossberg, A. Jagomägi, M. Danilson, J. Raudoja, Analysis of the edge emission of highly conductive $CuGaTe_2$, Thin Solid Films 515 (2007) 61926195.
27. Krishna C. Mandal, Anton Smirnov, Thermally Evaporated $AgGaTe_2$ Thin Films For Low-Cost p-$AgGaTe_2$/n-Si Heterojunction Solar Cells, MRS Proceeding, 744 (2002).
28. M. Grossberg, J. Krustok, A. Jagomägi, M. Leon, E. Arushanov, A. Nateprov, I. Bodnar, Investigation of potential and compositional fluctuations in $CuGa_3Se_5$ crystals using photoluminescence spectroscopy, Thin Solid Films 515 (2007) 6204-6207.
29. T. Raadik, J.Krustok, M.V. Yakushev, Photoreflectance study of $AgGaTe_2$ single crystals, Physica B 406 (2011) 418-420.
30. Xuanzhi Wu, High-efficient polycrystalline CdTe thin-film solar cells, Solar Energy 77 (2004) 803-814.
31. NREL, "Best Research –Cell Efficiencies," 2015. [Online] Available: http://www.nrel.gov/ncpv/images/efficiency_chart.jpg [Accessed 11 05 2015]
32. S.-H. Wei, S. B. Zhang, A. Zunger, First-principles calculation of band offsets, optical browings, and defects in CdS, CdSe, CdTe and their alloys, J. of Appl. Phys. 87 (3) (2000) 1304-1311.
33. T. Raadik, J. Krustok, R. Josepson, J. Hiie, T. Potlog, N. Spalatu, Temperature dependent electroreflectance study of CdTe solar cells, Thin Solid Films 535 (2013) 279-282.
34. J.N. Duenow, R.G. Dhere, H. R. Moutinho, B. To, J.W. Pankow, D. Kuciauskas, T.A. Gessert, CdS_xTe_{1-x} Alloying in CdS/CdTe Solar Cells, MRS Proceedings 1324 (6) (2011)

35. P. Sinsermsuksakul, K. Hartman, S. B. Kim, J. Heo, L. Sun, Enhancing the efficiency of SnS solar cells via band-offset engineering with a zinc oxysulfide buffer layer, Appl. Phys. Lett. 102 (2013) 053901-1-5.
36. S. Bhattacharyya, N. S. H. Gunda, R. Stern, S. Jacobs, R. Chmielowski, G. Dennlerb, G. K. H. Madsen, Achieving optimum carrier concentrations in p-doped SnS thermoelectrics, Phys. Chem. Chem. Phys. 17 (2015) 9161-9166.
37. T.Raadik, M.Grossberg, J.Raudoja, R.Traksmaa, J.Krustok, Temperature dependent photoreflectance study of SnS crystals, J. Of Physics and Cem. Of Solids 74 (2013) 1683-1685.
38. P. Sinsermsuksakul, L. Sun, S. W. Lee, H. H. Park, S.B. Kim, C. Yang, R. G. Gordon, Overcoming Efficiency Limitations of SnS- Based Solar Cells, Adv. Energy Mater. (2014) 1400469 1-7.
39. S. Cheng, G. Conibeer, Physical properties of very thin SnS films deposited by thermal evaporation, Thin Solid Films 520 (2011) 837-841.
40. M.Kumar, C. Persson, Cu_3BiS_3 as a potential photovoltaic absorber with high optical eff´iciency, Appl. Phys. Letters 102 (2013) 062109 1-4.
41. M.V.Yakushev, P. Maiello, T. Raadik, M.J Shaw, P.R. Edwards, G. Zoppi, J. Krustok, A.V. Mudryi, I. Forbes and R.W. Martin. Electronic and Structural Properties of Cu_3BiS_3 Thin Films. Thin Solid Films 562 (2014) 195-199.
42. G.Ray, A. Redinger, J. Sendler, T. P.Weiss, M. Thevenin, M. Guennou, B. El Adib, S.Siebentritt, The band gap of $Cu_2ZnSnSe_4$: effect of order-disorder ratio, Appl. Phys. Lett. 105 (2014) 112106 1-4.
43. P. Jackson, Properties of $Cu(InGa)Se_2$ solar cells with new reckord efficiency up to 21.7 %, Phys. Status Solidi RRL 9 (1) (2015) 28-31.
44. Y. S. Lee, T. Gershon, O. Gunawan, T.K. Todorov, T. Gokmen, Y. Virgus, S. Guha, $Cu_2ZnSnSe_4$ Thin-Film Solar Cells by Thermal Co-evaporation with 11.6% Efficiency and Improved Minority Carrier Diffusion Length, Adv. Energy Mater. 5 (2015) 1401372 1-4.
45. M. Grossberg, Photoluminescence study of disordering in the cation sublattice of Cu_2ZnSnS_4 , Current Applied Physics 14 (2014) 1424-1427.
46. Harry Lipsanen, PhD Thesis, Photoreflectance and X-ray Diffraction Study of Semiconductor Heterostructures and Quantum Wells (1994).
47. S.A. Bashkirov, V. F. Gremenok, V.A. Ivanov, Physical properties of SnS Thin Films Fabricated by Hot Wall Deposition, Semiconductors 45 (6) (2011) 749.
48. Peter Y. Yu, Manuel Cardona, Fundamentals of Semiconductors, Physics and Materials Properties, 4th edition, Springer 2010.
49. Rheinhardt Hendrik Sieberhagen, PhD Theses, Optical characterization of semiconductors using photo reflection spectroscopy, University of Pretoria (2002).
50. B. Seraphin, N. Bottka, Band-Structure Analysis from Electro-Reflectance Studies, Phys. Rev. 145 (1966) 628-636.

51. F. Mesa , A. Dussan , B. A. Paez-Sierra , H. Rodriguez-Hernandez, Hall Effect and transient surface photovoltage (SPV) study of Cu3BiS3 thin films, Univ. Sci. 19 (2) (2014) 99-105.
52. D.F Marron, E. Canovas, Application of photoreflectance to advanced multilayer structures for photovoltaics, Mat. Sci. & Eng. B 178 (9) (2012) 599-608.
53. D.E. Aspnes, Third derivative modulation spectroscopy with low-field electroreflectance, Surf. Sci. 37 (1973) 418-442.
54. D.E. Aspnes, J.E. Rowe, Resonant Nonlinear Optical Susceptibility: Electroreflectance in the Low Field Limit, Phys. Rev. B5 (10) (1972) 4022-4029.
55. J.T. Foley, U. Landman, Model dielectric function for semiconductors: Si, Physical Review B 14 (4) (1976) 1597-1604.
56. R. Kudrawiec, PhD Thesis, Institute of Physics, Wroclaw University of Technology (2004).
57. W. –H. Chang, T. M. Hsu, W. C. Lee, and R. S. Chuang, A study of the Franz–Keldysh oscillations in electromodulation reflectance of Si-delta-doped GaAs by a fast Fourier transformation, J. Appl. Phys. 83 (12) (1998) 7873-7878.
58. M. Courtney, N. Spellmeyer, Classic, semiclassical, and quantum dynamics in the lithium Stark system, Physical Review A 51 (5) (1995) 3604-3620.
59. R.D. Tomlinson, Fabrication of $CuInSe_2$ single crystals using melt-growth techniques, Sol. Cells 16 (1986) 17-26.
60. L.S. Palatnik, E.K. Belova, Izv. Akad. Nauk SSSR Neorg. Mater. 3 (1967) 2194-2198.
61. A. Burger, J.O. Ndap, Y. Cui, U. Roy, S. Morgan, K. Chattopadhyay, X. Ma, K. Faris, S. Thibaud, R. Milers, H. Mateen, J.T. Goldstein, C.J. Rawin, Preparation and thermophysical properties of $AgGaTe_2$ crystals, J. Cryst. Growth 225 (2001) 505-511.
62. C. Julien, I. Ivanov, A. Khelfa, F. Alapini, M. Guittard, Characterization of ternary compound $AgGaTe_2$ and $AgGa_5Te_8$, J. Mater. Sci. 31 (1996) 3315-3319.
63. H.R. Handrasekhar, R.G.Humphreys, U.Zwick, M.Cardona, Infrared and Raman spectra of the IV-VI compound SnS and SnSe, Phys. Rev. B15 (1977) 2177-2183.
64. S. López-Marino, Y. Sánchez, M. Placidi, A. Fairbrother, M. Espindola-Rodríguez, X. Fontané, V. Izquierdo-Roca, J. López-García, L. Calvo-Barrio, A. Pérez-Rodríguez, E. Saucedo, ZnSe etching of Zn-Rich $Cu_2ZnSnSe_4$: An oxidation route for improved solar-cell efficiency, Chem. – Eur. J. 19 **(**2013) 14814-14822.
65. S. Arai, S. Ozaki, S. Adachi, Optical properties and electronic badn structure of $AgGaTe_2$ chalcopyrite semiconductor, Appl. Opt. 49 (5) (2010) 829-837.

66. P. Horodyský, P. Hlídek, Free-exciton absorption in bulk CdTe: temperature dependence, Phys. Status Solidi B 243 (2006) 494-501.
67. X. Mathew, Band gap of CdTe thin films- The dependence on temperature, J. Mater. Sci. Lett. 21 (2002) 529-531.
68. G. Fonthal, L. Tirado-Mejía, J.I. Marín-Hurtado, H. Ariza-Calderón, J.G. Mendoza- Alvarez, Temperature dependence of the band gap energy of crystalline CdTe, J. Phys. Chem. Solids 61 (2000) 579-583.
69. M. Hädrich, N. Lorenz, H. Metzner, U. Reislöhner, S. Mack, M. Gossla, W. Witthuhn, CdTe-CdS solar cells – Production in a new baseline and investigation of material properties, Thin Solid Films 515 (15) (2007) 5804-5807.
70. W.S. Enloe, J.C. Parker, J. Vespoli, T. H. Myers, R. L. Harper and J. F. Schetzina, AN electroreflectance study of CdTe, J. Appl. Phys. 61 (5) (1987) 2005-2010.
71. S. Logothetidis, M. Cardona, P. Lautenschlager, M. Garriga, Temperature dependence of the dielectric function and the interband critical points of CdSe, Phys. Rev. B 34 (1986) 2458-2469.
72. M. Parenteau, C.Carlone, Influence of temperature and pressure on the electronic transitions in SnS and SnSe semiconductors, Phys. Rev. B41(1990) 5227-5234.
73. K. P. O′ Donnell, X. Chen, Temperature dependence of semiconductor band gaps, Appl. Phys. Lett. 58 (1991) 2924-2926.
74. M.V. Yakushev, F. Luckert, C. Faugeras, A.V. Karotki, A.V. Mudryi, R.W. Martin, Diamagnetic shift of the A free exciton in CuGaSe2, Appl. Phys. Lett. 97 (2010) 152110 1-3.
75. J.L. Shay, B. Tell, L.M. Schiavone, H.M. Kasper, F. Thiel, Energy bands of AgInS2 in the chalcopyrite and orthorhombic structures, Phys. Rev. B 9 (1974) 1719-1723.
76. S.G. Choi, T.J. Kim, S.Y. Hwang, J. Li, C. Persson, Y.D. Kim, S.-H. Wei , I.L. Repins, Temperature dependent band-gap energy for Cu2ZnSnSe4: A spectroscopic ellipsometric study, Solar Energy Materials & Solar Cells 130 (2014) 375-379.
77. D. Huang and C. Persson, Band gap change induced by defect complexes in Cu_2ZnSnS_4 , Thin Solid Films 535 (2013) 265-269.
78. S. Chen, A. Walsh, X.-G. Gong, S.-H. Wei, Classification of lattice defects in the kesterite Cu_2ZnSnS_4 and $Cu_2ZnSnSe_4$ earth-abundant solar cell absorbers, Adv. Mater. 25 (2013) 1522-1539.
79. M. Grossberg, T. Raadik, J. Raudoja, J. Krustok, Photoluminescence study of defect clusters in Cu_2ZnSnS_4 polycrystals, Curr. Appl. Phys. 14 (2014) 447-450.
80. C. Krämmer, C. Huber, C. Zimmermann, M. Lang, T. Schnabel, T. Abzieher, E. Ahlswede, H. Kalt, and M. Hetterich, Reversible order-disorder related band gap changes in $Cu_2ZnSn(S,Se)_4$ via post- annealing

of solar cells measured by electroreflectance, Appl. Phys. Lett. 105 (2014) 262104 1-4.
81. J. Krustok, R. Josepson, T. Raadik and M. Danilson. Potential fluctuations in $Cu_2ZnSnSe_4$ solar cells studied by temperature dependence of quantum efficiency curves, Physica B, 405 (2010) 3186–3189.
82. T. P. Weiss, A. Redinger, J. Luckas, M. Mousel and S. Siebentritt, Admittance spectroscopy in kesterite solar cells: Defect signal or circuit response, Appl. Phys. Lett. 102 (2013) 202105 1-4.
83. S.G. Choi, T.J. Kim, S.Y. Hwang, J. Li, C. Persson, Y.D. Kim, S.-H. Wei, I.L. Repins, Temperature dependent band-gap energy for Cu2ZnSnSe4: A spectroscopic ellipsometric study, Solar Energy Materials & Solar Cells 130 (2014) 375-379.
84. A. Fairbrother, M. Dimitrievska, Y. Sanchez, V. Izquierdo-Roca, A. Perez-Rodrguez, and E. Saucedo, Compositional paradigms in multinary compound systems for photovoltaic applications: a case study of kesterites, J. Mater. Chem. A, 3 (2015) 9451-9455.

Appendix A

Article I

T. Raadik, J. Krustok, M.V. Yakushev. Photoreflectance study of $AgGaTe_2$ single crystals. *Physica B: Physics of Condensed Matter* 406 (2011), pp. 418-420.

Physica B 406 (2011) 418–420

Contents lists available at ScienceDirect

Physica B

journal homepage: www.elsevier.com/locate/physb

Photoreflectance study of $AgGaTe_2$ single crystals

T. Raadik [a,*], J. Krustok [a], M.V. Yakushev [b]

[a] Department of Materials Science, Tallinn University of Technology, Ehitajate tee 5, 19086 Tallinn, Estonia
[b] Department of Physics, Strathclyde University, Glasgow G4 0NG, UK

ARTICLE INFO

Article history:
Received 17 June 2010
Received in revised form
30 September 2010
Accepted 2 November 2010

Keywords:
Solar energy materials
Photoreflectance
Semiconductors
Ternary chalcopyrite $AgGaTe_2$

ABSTRACT

The optical properties of ternary chalcopyrite $AgGaTe_2$ were studied by photoreflectance spectorscopy (PR). Due to the optimal direct energy gap and high absorption coefficient $AgGaTe_2$ is a promising material for solar energy conversion. Single crystals used in this work were grown by the vertical Bridgman technique. The PR temperature dependent spectra were measured in the range of 25–300 K. At room temperature two energy gaps in $AgGaTe_2$ were detected: $E_g^A = 1.320$ eV and $E_g^B = 1.425$ eV, with temperature coefficients $dE_g^A/dT = -2.1 \times 10^{-4}$ eV/K and $dE_g^B/dT = -3.4 \times 10^{-4}$ eV/K. At low temperature ($T = 25$ K) these bandgap energies were $E_g^A = 1.355$ eV and $E_g^B = 1.466$ eV. Temperature dependence of bandgap energies is maximum at about $T = 90$ K.

1. Introduction

Despite the fact that optical properties of $AgGaTe_2$ (AGT) have been studied for over 30 years, there are still some open questions. It is known that AGT is a member of chalcopyrite ternaries and the reported direct energy gap is suitable for solar energy conversion. At the same time there is wide variation in the actual value of this bandgap energy and the electronic band structure has different interpretations. The most common method to measure bandgap energy is optical absorption. However, it is known that in chalcopyrite ternaries usually large potential fluctuations are present and therefore the density of states function near band edges is quite complex [1–4]. This is why absorption spectra greatly depend on the depth of these potential fluctuations. Deeper fluctuations usually give additional absorption at lower energies and thus the absorption tail is formed. The shape of this tail is not always known and therefore the bandgap energy calculated from the absorption spectrum could be incorrect. Another approach to obtain the bandgap energy is to use various modulation methods like electroreflectance, photoreflectance or thermoreflectance. Tell et al. [5] measured the electroreflectance spectra of an $AgGaTe_2$ single crystal at 77 and 300 K. At room temperature they found the lowest bandgap energy $E_g = 1.316$ eV, while at 77 K the bandgap energy was $E_g = 1.356$ eV. Due to valence band splittings they also measured higher energy bandgaps at 77 K: $E_g^B = 1.472$ eV and $E_g^C = 2.26$ eV. Very similar results were published by Bodnar et al. [6] on AGT thin films using absorption measurements. At room temperature they found $E_g^A = 1.32$ eV, $E_g^B = 1.43$ eV, and $E_g^C = 2.14$ eV. Thermoreflectance spectroscopy was also recently used for single crystals of AGT by Arai et al. [7] at $T = 20$–300 K. The lowest direct bandgaps determined from thermoreflectance spectra were $E_g^A = 1.36$ eV, $E_g^B = 1.19$ eV, and $E_g^C = 2.00$ eV at $T = 20$ K. As can be seen the lowest bandgap in this paper has an energy $E = 1.19$ eV. At the same time the low temperature ($T = 15$ K) bandgap energy determined using optical absorption from the same single crystals was about 1.25 eV. It is interesting that different methods give different bandgap energies. In this paper we will present the photoreflectance data of Bridgman grown AGT measured in a wide temperature range.

2. Experimental

An ingot of AGT was grown by the vertical Bridgman technique often used for fabrication of $CuInSe_2$ and other chalcopyrite ternary compounds [8]. A pseudobinary phase diagram for $AgGaTe_2$ has been determined by Palatnik and Belova [9], establishing the melting point to be 725.7 °C [10]. At first a near stoichiometrical mixture of high (99.999%) purity Ag, Ga, and Te was sealed in vacuum of 10^{-5} mbar in a thick walled (3 mm) quartz ampoule of 10 mm inner-diameter. Then this mixture was prereacted at 900 °C for 2 h in a rocking furnace and solidified in a horizontal position. After cooling down the ampoule was introduced into the upper (hot) zone of a two-zone vertical furnace. The material was melted again and held at a temperature of 900 °C for 6 h. Then the temperature in the upper part of the furnace was reduced to 800 °C and that in the lower part to 700 °C. The furnace was slowly moved up, translating the ampoule into the lower (cold) zone at the

* Corresponding author. Tel.: +372 620 3210.
E-mail address: taavi.raadik@ttu.ee (T. Raadik).

0921-4526/$ - see front matter © 2010 Elsevier B.V. All rights reserved.
doi:10.1016/j.physb.2010.11.002

speed of 2 cm a day through a temperature gradient. The solidified material was cooled at a rate of 3 °C/h down to 200 °C. In the middle part the grown ingot had a 2 cm long cylindrical shaped single grain of $AgGaTe_2$. The elemental composition of the resulting single crystals was confirmed by EDX and RBS measurements. The elemental composition varied along the ingot, gradually becoming Ag rich close to the end of the freeze (top) zone.

Single crystal surfaces with a size of about 2×2 mm were freshly cleaved from the ingot for PR measurements.

Before PR measurements Raman measurements were made at room temperature with a micro-Raman spectrometer Horiba Yobin Yvon HR800; a Nd–YAG laser with $\lambda = 532$ nm was used for excitation. Photoreflectance (PR) measurements were made with a traditional setup, where an $f = 40$ cm grating monochromator together with a 250 W halogen bulb was used for the primary beam and the 50 mW He–Cd laser ($\lambda = 441$ nm) as a secondary beam. The reflectance signal at 225 Hz was detected using a Si detector and a lock-in amplifier. The crystals under study were glued with cryogenic grease on the cold finger of the closed-cycle He cryostat.

3. Results and discussion

From the Raman measurements in Fig. 1, 4 main peaks are clearly seen; the most intensive is at 130 cm^{-1} and the others are at 94, 201, and 221 cm^{-1}. These peaks are typical for an $AgGaTe_2$ crystal [11] and according to these spectra we can be sure that we have a pure $AgGaTe_2$ single crystal without additional phases. Photoreflectance spectra at two different temperatures are shown in Fig. 2. Despite our efforts we detected only two signals originating from A and B bandgaps. Even at low temperatures the C bandgap reported by Tell et al. [5] and Bodnar et al. [6] could not be detected.

Each PR spectrum has been analyzed by the low-field electroreflectance line-shape function, the third derivative functional form [12]

$$\Delta R/R = \mathrm{Re}\{Fe^{i\theta}(E - E_g) + i\Gamma\}^m, \quad (1)$$

where E is the photon energy and F, θ, E_g, and Γ are the amplitude, phase, energy, and broadening parameter of the spectrum, respectively; m is a parameter that depends on the critical point type and $m = 5/2$ (the three-dimensional critical point) has been used in this study. Results of this analysis are also presented in Fig. 2 as continuous lines.

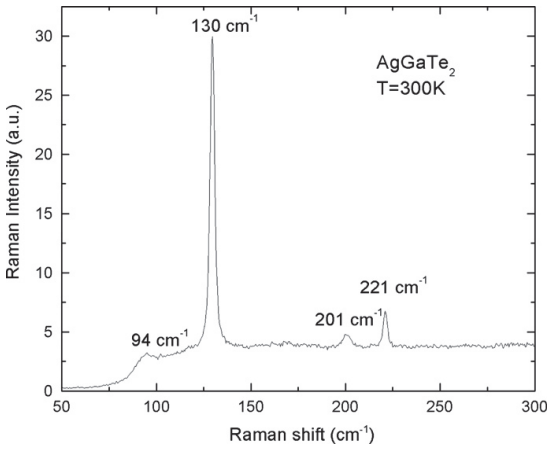

Fig. 1. Room temperature Raman spectrum of $AgGaTe_2$ crystal.

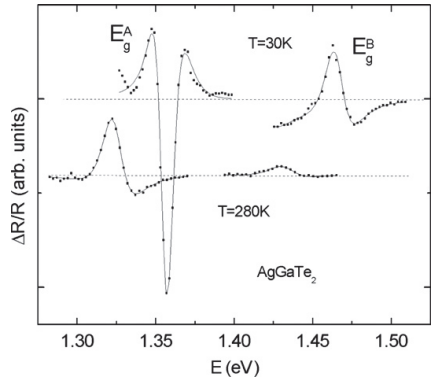

Fig. 2. Photoreflectance spectra of $AgGaTe_2$ crystal at different temperatures. Continuous lines represent the fitting results. A and B bandgaps are clearly resolved.

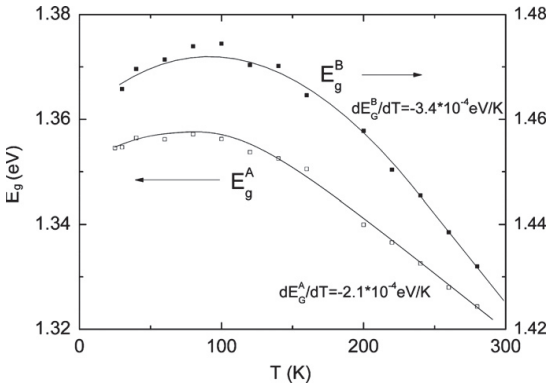

Fig. 3. Temperature dependence of A and B bandgap energies of $AgGaTe_2$ crystal obtained from photoreflectance spectra. At higher temperatures nearly linear dependence can be observed.

All PR measurements were made at $T = 25$–295 K. From these measurements, after fitting with Eq. (1), E_g^A and E_g^B were found and the results are presented in Fig. 3. It can be seen that both bandgap energies have a maximum at about $T = 90$ K. This behavior is typical for ternary compounds containing Ag and the same kind of behavior in AGT was also observed by Bodnar et al. [13]. It is suggested that this trend can be due to the effects of lattice dilation and electron–phonon interaction. At the same time the temperature dependence of bandgap energies found by Arai et al. [7] did not show any maximum. At higher temperatures the temperature dependence of bandgap energies shows a nearly linear trend, but the rate of this trend is different for different bandgaps (see Fig. 3). The lowest bandgap shows a temperature coefficient $dE_g^A/dT = -2.1 \times 10^{-4}$ eV/K and this value is very close to the value -2.02×10^{-4} eV/K found by Bodnar et al. [13]. The temperature coefficients found by Arai et al. [7] for their A–C bandgaps are all in the range $dE_g/dT = -(2.4\text{–}2.6) \times 10^{-4}$ eV/K. Thus our results support the findings made by Tell et al. [5] and Bodnar et al. [6,13].

4. Conclusion

$AgGaTe_2$ crystals were studied at different temperatures using photoreflectance spectroscopy. The lowest bandgap energy at

room temperature was found to be $E_g^A = 1.320$ eV and the temperature coefficient was $dE_g^A/dT = -2.1 \times 10^{-4}$ eV/K. The next bandgap energy was $E_g^B = 1.425$ eV and temperature coefficient $dE_g^B/dT = -3.4 \times 10^{-4}$ eV/K. The bandgap energy maximum was around $T = 90$ K with values $E_g^A = 1.357$ eV and $E_g^B = 1.474$ eV.

Acknowledgements

This work was supported by the Estonian Science Foundation Grant G-8282 and by the target financing by HTM (Estonia) no. SF0140099s08.

References

[1] J. Krustok, H. Collan, M. Yakushev, K. Hjelt, Phys. Scr. T 79 (1999) 179.
[2] J. Krustok, J. Raudoja, M. Yakushev, R.D. Pilkington, H. Collan, Phys. Status Solidi 173 (1999) 483.
[3] B.I. Shklovskii, A.L. Efros, Electronic Properties of Doped Semiconductors, second ed., Springer, Berlin, 1984.
[4] J. Krustok, A. Jagomägi, M. Grossberg, J. Raudoja, M. Danilson, Sol. Energy Mater. Sol. Cells 90 (2006) 1973.
[5] B. Tell, J.L. Shay, H.M. Kasper, Phys. Rev. B 9 (1974) 5203.
[6] I.V. Bodnar, V.F. Gremenok, I.A. Viktorov, O.N. Obraztsova, J. Appl. Spectrosc. 60 (1997) 809.
[7] S. Arai, S. Ozaki, S. Adachi, Appl. Opt. 49 (2010) 829.
[8] R.D. Tomlinson, Sol. Cells 16 (1986) 17.
[9] L.S. Palatnik, E.K. Belova, Izv. Akad. Nauk SSSR Neorg. Mater. 3 (1967) 2194.
[10] A. Burger, J.O. Ndap, Y. Cui, U. Roy, S. Morgan, K. Chattopadhyay, X. Ma, K. Faris, S. Thibaud, R. Milers, H. Mateen, J.T. Goldstein, C.J. Rawin, J. Cryst. Growth 225 (2001) 505.
[11] C. Julien, I. Ivanov, A. Khelfa, F. Alapini, M. Guittard, J. Mater. Sci. 31 (1996) 3315.
[12] D.E. Aspnes, in: M. Balkanski (Ed.), Handbook on Semiconductors II, North-Holland1980, p. 109.
[13] I.V. Bodnar, V.F. Gremenok, R.W. Martin, M.V. Yakushev, Opt. Spectrosc. 88 (2000) 377.

Appendix A

Article II

T. Raadik, J. Krustok, R. Josepson, J. Hiie, T. Potlog, N. Spalatu. Temperature dependent electroreflectance study of CdTe solar cells. *Thin Solid Films* 535 (2013), 184-187.

Thin Solid Films 535 (2013) 279–282

Contents lists available at SciVerse ScienceDirect

Thin Solid Films

journal homepage: www.elsevier.com/locate/tsf

Temperature dependent electroreflectance study of CdTe solar cells

T. Raadik [a,*], J. Krustok [a], R. Josepson [a], J. Hiie [a], T. Potlog [b], N. Spalatu [b]

[a] Tallinn University of Technology, Ehitajate tee 5, 19086 Tallinn, Estonia
[b] Moldova State University, A. Mateevici str. 60, MD-2009 Chisinau, Moldova

ARTICLE INFO

Available online 8 January 2013

Keywords:
Electroreflectance
Cadmium telluride
Thin-film
Solar cells

ABSTRACT

Cadmium telluride is a promising material for large scale photovoltaic applications. In this paper we study CdS/CdTe heterojunction solar cells with electroreflectance spectroscopy. Both CdS and CdTe layers in solar cells were grown sequentially without intermediate processing by the close-space sublimation method. Electroreflectance measurements were performed in the temperature range of T = 100–300 K. Two solar cells were investigated with conversion efficiencies of 4.1% and 9.6%. The main focus in this work was to study the temperature dependent behavior of the broadening parameter and the bandgap energy of CdTe thin film in solar cells. Room temperature bandgap values of CdTe were $E_g = 1.499$ eV and $E_g = 1.481$ eV for higher and lower efficiency solar cells, respectively. Measured bandgap energies are lower than for single crystal CdTe. The formation of $CdTe_{1-x}S_x$ solid solution layer on the surface of CdTe is proposed as a possible cause of lower bandgap energies.

1. Introduction

Cadmium telluride is a promising material for thin-film solar cells due to its direct optical bandgap with energy of about $E_g = 1.5$ eV and high absorption coefficient $> 5 * 10^5$/cm [1–4]. Record conversion efficiency of 17.3% was recently reported by First Solar for polycrystalline CdTe thin-film solar cell [5]. However, the record efficiency of CdTe solar cells is much less than its theoretical maximum (~29%). One possible reason for this could be related with problems in p–n junction between CdS and CdTe. It is proposed that the formation of $CdS_{1-x}Te_x$ solid solution layer with lower bandgap energy somehow affects the behavior of CdS/CdTe solar cells [6]. Also, the interface and bulk recombination reduces solar cell efficiency. Among other methods the electroreflectance spectroscopy (ER) is proven to be quite a powerful technique for investigation of junction properties. Room temperature ER studies were performed in several papers, mainly the bandgap energy and crystal quality were investigated [3,7,8]. Dhere et al. [9] performed room temperature ER measurements of CdTe solar cells and showed the presence of a high field region of 32 kV/cm in the CdS/CdTe interface layer. At the same time it could be interesting to study also temperature dependent electroreflectance behavior and find differences between different solar cells.

In the present work two CdS/CdTe heterojunction solar cells with different properties were studied. Differences between studied cells were in fabrication parameters and in back contact preparation. We used temperature dependent electroreflectance for characterization of CdTe solar cell junction properties. In addition to ER measurements, the results of current–voltage (I–V) curve measurements and external quantum efficiency measurements (QE) are presented.

2. Experimental details

Thin film CdS/CdTe solar cells were fabricated on glass substrates with an area of 2×2 cm^2 covered with a SnO_2 layer with a sheet resistivity of about 10 Ω/□. SnO_2 served as the transparent front contact to CdS. Both undoped CdS and CdTe layers were grown sequentially without intermediate processing by the close-space-sublimation (CSS) method. CdS had the resistivity of 2–3 Ω·cm and transparency over 80%. The CdTe layers had the resistivity in the range of $\sim 5 * 10^5$ Ω·cm. After the CdTe layer was deposited, the structures were held in $CdCl_2$:H_2O saturated solutions and then annealed in the air at 410 °C for ~30 min. To minimize the back contact barrier, an additional layer (~300 nm) of Te for one cell (Cell 1) or Cu for another cell (Cell 2) was used. In Cell 1 the CdTe was deposited at the substrate temperature of 440 °C, in Cell 2 at the temperature of 430 °C. The CdTe source temperature in both cases was 580 °C. All cells were completed with a Ni metal contact thermally deposited in vacuum. Both types of the solar cells have been fabricated in a superstrate configuration, and more details were given in [10].

Before ER measurements, I–V and QE measurements were made. I–V curves were measured at room temperature with illumination of 100 mW/cm^2 using the Oriel class A solar simulator 91159A. For electroreflectance measurements the DC- and AC-voltage was applied to a solar cell under study via back and front contact by a pulse generator with frequency of 275 Hz, AC value of ±0.8 V and DC component of −0.8 V. Computer controlled grating monochromator SPM-2 (f = 40 cm) together with a 250 W halogen bulb was used for illumination. The ER signal was detected using a Si detector and a lock-in

* Corresponding author.
E-mail address: taavi.raadik@ttu.ee (T. Raadik).

0040-6090/$ – see front matter
http://dx.doi.org/10.1016/j.tsf.2012.12.083

amplifier (SR 810). Solar cells under study were mounted into a closed-cycle He cryostat to perform temperature dependent ER measurements in the range of T = 100–300 K.

3. Results and discussion

3.1. I–V curves and QE of solar cells

Typical I–V curves of thin film CdS/CdTe heterojunction solar cells under the illumination are presented in Fig. 1. As it can be seen, Cell 1 shows better solar cell parameters with open circuit voltage V_{OC} = 783 mV, short circuit current density J_{SC} = 23.1 mA/cm^2 and conversion efficiency of 9.6%. The Cell 2 has quite different parameters, but still the open circuit voltage is V_{OC} = 661 mV and the short circuit current density is J_{SC} = 18.2 mA/cm^2, whereas the cell efficiency is lower, only 4.1%.

A comparison of the external quantum efficiency measurements, see Fig. 2, shows that Cell 1 has much steeper QE spectrum at long wavelength side than Cell 2. In the long-wavelength range the spectra restricted to the value of the CdTe bandgap energy which is equal to 1.499 eV (827 nm) for Cell 1 and 1.481 eV (837 nm) for Cell 2 at room temperature as measured by ER. The steeper shape of Cell 1 QE spectrum at long wavelength side leads to the steeper bandgap edge and could be one reason for better junction properties.

3.2. Temperature dependence of electroreflectance

Electroreflectance is a modulation spectroscopy where the external AC voltage is applied to the structure in order to modulate internal electric field.

Electroreflectance can be classified into three categories: weak, intermediate and strong field regimes, depending on the strength of a local electrical field in the junction. ER spectra with a weak field approach can be well fitted with a third derivative functional form (TDFF) given by Aspnes [11]:

$$\frac{\Delta R}{R} = \mathrm{Re}\left[Ce^{i\phi}\left(E - E_g + i\Gamma\right)^{-m}\right], \quad (1)$$

where E is the photon energy ($h\nu$), C is an amplitude parameter, ϕ phase parameter, E_g energy of the bandgap and Γ a broadening parameter, that reflects structural and compositional disorders. The exponent m depends on the type of the critical point and determining its proper value is of particular importance in analyzing ER spectra. Enloe and Parker [3] and Yu et al. [8] have improved their electroreflectance and photoreflectance fits by using m as independent variable and we used the same logic. Value m = 2.5, corresponding to a three-dimensional critical point, did not give a good fitting result. Therefore m = 3, corresponding to a two-dimensional critical point, was used for the fitting of all ER spectra since this value yielded an excellent fit for majority of our data. To use m = 3 there are two possible explanations. A better fit is expected since the electron effective mass is significantly larger in one symmetry direction than the other two near the X point. Actually, neither n = 2.5 nor m = 3 can be strictly correct since both were derived under the assumption of a parabolic-band structure. Another possibility is that excitonic effect may be contributing to the transition in high-quality CdTe samples. The influence of excitons can cause a three-dimensional transition to appear as a two-dimensional in nature [3]. Temperature dependent ER spectra together with Aspnes fit (Eq. (1)) of Cell 1 and Cell 2 are presented in Figs. 3 and 4. It is clearly seen that the spectrum shifts towards higher energies with decreasing temperature and the ER signal intensity increases as can be seen from scale factors.

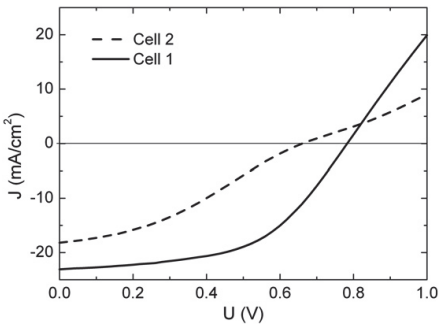

Fig. 1. I–V curves of the studied solar cells under illumination at room temperature.

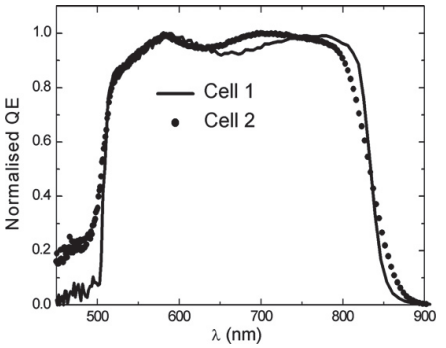

Fig. 2. Normalized QE curves of the studied solar cells.

Temperature dependence of bandgap energies obtained from the fittings with Eq. (1) is plotted in Fig. 5. E_g values are considerably lower than reported reference values of monocrystalline CdTe, see Fig. 5 [1]. Temperature coefficients were found to be $dE_g/dT = -3.1\times10^{-4}$ eV/K for Cell 1 and $dE_g/dT = -3.5\times10^{-4}$ eV/K for Cell 2. These values are in good agreement with the results obtained by Mathew et al. [12].

It is seen that the obtained bandgap energies are smaller than those found for monocrystalline CdTe in other papers [1,2]. The smaller bandgap energies in our cells can be explained by assuming a formation of $CdTe_{1-x}S_x$ solid solution in the p–n junction region. Sulfur has incorporated into CdTe during the thermal treatment. Hädrich et al. [6] have found that the dependence of the bandgap energy of the $CdTe_{1-x}S_x$ solid solution is given by the empirical equation:

$$E_g(x) = 2.4x + 1.51(1-x) - 1.8x(1-x). \quad (2)$$

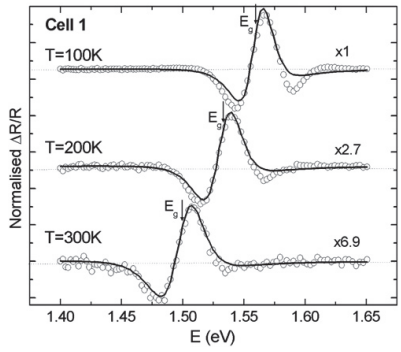

Fig. 3. ER spectra of sample Cell 1 at 100 K, 200 K and 300 K. Dots show the experimental result and continues lines are the fitting results with Eq. (1).

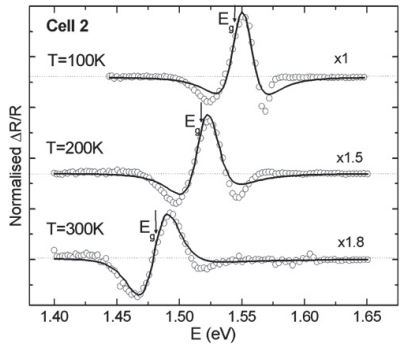

Fig. 4. ER spectra of sample Cell 2 at 100 K, 200 K and 300 K. Dots show the experimental result and continues lines are the fitting results with Eq. (1).

At room temperature we found bandgap energies $E_g = 1.499$ eV and $E_g = 1.481$ eV for Cell 1 and Cell 2, respectively. According to Eq. (2) we have a $CdTe_{1-x}S_x$ solid solution with average sulfur content of $x = 0.01$ for Cell 1 and $x = 0.03$ for Cell 2. It is obvious that the solid solution layer does not have any abrupt edge and probably we have a layer with varying concentration of sulfur. Cell 1 with smaller sulfur content in solid solution, showed a better solar cell performance, as we saw from I–V measurements. Similar behavior was described also by Hädrich et al. [6].

The broadening parameter Γ is often used as a measure of crystal quality since its magnitude is primarily determined by lattice defects such as disorders, vacancies, and impurities [3]. In our experiment, as it can be seen from Fig. 6, Γ is found to be 29 meV for Cell 1 and 27 meV for Cell 2 at room temperature and it is decreasing with decreasing temperature. Comparing our results with other authors, it can be concluded that CdTe samples with a broadening parameter value around 30 meV and less can be classified into good quality samples category [3].

The effect of temperature provides not only the shift of the bandgap energy but also the change in the broadening parameter. If we grant the electron–phonon coupling as a main broadening mechanism, its parameter value can be written, by taking into account the Bose–Einstein occupation factor, as in [13]:

$$\Gamma(T) = \Gamma_1 + \left(\frac{\Gamma_0}{e^{\Theta_\Gamma/T} - 1}\right), \tag{3}$$

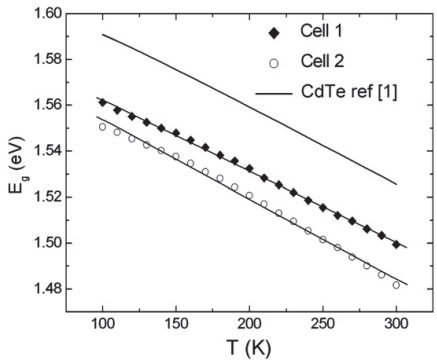

Fig. 5. Bandgap energy values found from ER fittings as a function of temperature. The upper curve represents the bandgap energy of the monocrystalline CdTe from ref. [1].

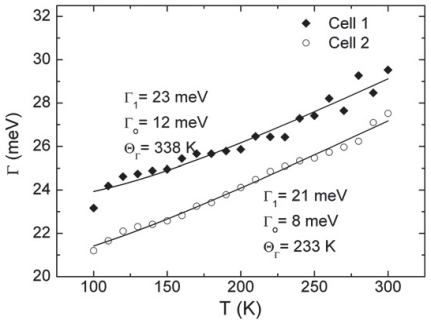

Fig. 6. The temperature dependence of the broadening parameter Γ with fittings (solid curves) using Eq. (3).

where Γ_1 represents the broadening due to temperature-independent mechanism such as crystalline imperfections and surface scattering, Γ_0 represents the strength of electron–phonon coupling, Θ_Γ is an average phonon temperature.

Fig. 6 shows the ER broadening parameter Γ as a function of temperature and least-squares fits (solid curves) with the Eq. (3) together with fitting parameters. The obtained Γ_1 values of 23 meV and 21 meV for samples Cell 1 and Cell 2, respectively, indicate relatively high quality of the CdTe thin film. Calculated values of $\Gamma_0 = 12$ meV and $\Theta_\Gamma = 338$ K for Cell 1 and $\Gamma_0 = 8$ meV and $\Theta_\Gamma = 233$ K for Cell 2 are comparable for both solar cells. It is interesting that solar cell with lower efficiency shows also a lower value of Γ_1. This difference between broadening parameters could also be an important factor in properties of the respective p–n junction. However further studies are needed in order to clarify this assumption.

4. Conclusion

Temperature dependent ER measurements (T = 100–300 K) were performed with two different CdS/CdTe solar cells. All ER spectra were fitted using Aspnes third derivative functional form. Room temperature bandgap energies $E_g = 1.499$ eV and $E_g = 1.481$ eV for Cell 1 and Cell 2, respectively, were found. The low value of the broadening parameter Γ for both solar cells shows a good quality of CdTe absorber layers. The formation of $CdTe_{1-x}S_x$ solid solution in the p–n junction region was detected for both solar cells. However, Cell 2 had smaller broadening parameter value, but Cell 1 showed a better solar cell performance. In conclusion, we showed that the temperature dependent ER measurements could give valuable information about the junction properties of solar cells.

Acknowledgment

This work was supported by the Estonian Science Foundation grants 8282 and 9369, by the target financing projects SF0140099s08 and SF0140092s08, by the Estonian Centre of Excellence Research Project TK117T, by the European Social Fund's Doctoral Studies and International Programme DoRa, and by the European Union through the 7th FP project FLEXSOLCELL GA-2008-230861. The support of the World Federation of Science National Scholarship Program is gratefully acknowledged.

References

[1] P. Horodyský, P. Hlídek, Phys. Status Solidi B 243 (2006) 494.
[2] G. Fonthal, L. Tirado-Mejía, J.I. Marín-Hurtado, H. Ariza-Calderón, J.G. Mendoza-Alvarez, J. Phys. Chem. Solids 61 (2000) 579.
[3] W.S. Enloe, J.C. Parker, J. Appl. Phys. 61 (1987) 2005.
[4] X. Wu, R.G. Dhere, D.S. Albin, T.A. Gessert, Sol. Energy 77 (2004) 803.

[5] U.S Department of Energy, Energy Efficiency & Renewable Energy, 2010 Solar Technologies Market Report, Colden, CO, http://www.nrel.gov/docs/fy12osti/51847.pdf 2011.
[6] M. Hädrich, N. Lorenz, H. Metzner, U. Reislöhner, S. Mack, M. Gossla, W. Witthuhn, Thin Solid Films 515 (2007) 5804.
[7] N.W. Duffy, L.M. Peter, R.L. Wang, J. Electroanal. Chem. 532 (2002) 207.
[8] Z. Yu, S.G. Hofer, N.C. Giles, T.H. Myers, C.J. Summers, Phys. Rev. B 51 (1995) 13789.
[9] R.G. Dhere, Y. Zhang, M.J. Romero, S.E. Asher, San Diego, U.S.A., May 11 16, 2008, 33rd IEEE PVSC Symposium Proceeding, 2008, p. 1137.
[10] T. Potlog, N. Spalatu, V. Fedorov, N. Maticiuc, C. Antoniuc, V. Botnariuc, J. Hiie, T. Raadik, V. Valdna, Seattle, U.S.A., June 19 24, 2011, 37th IEEE PVSC Symposium Proceedings, 2011, p. 1365, http://dx.doi.org/10.1109/PVSC.2011.6186211.
[11] D.E. Aspnes, Surf. Sci. 37 (1973) 418.
[12] X. Mathew, J. Mater. Sci. Lett. 21 (2002) 529.
[13] S. Logothetidis, M. Cardona, P. Lautenschlager, M. Garriga, Phys. Rev. B 34 (1986) 2458.

Appendix A

Article III

T.Raadik, M. Grossberg, J. Raudoja, J. Krustok. Temperature dependent photoreflectance study of SnS crystals. *Journal of Physics and Chemistry of Solids* , 74 (12) (2013), 1683-1685.

Journal of Physics and Chemistry of Solids 74 (2013) 1683–1685

Contents lists available at ScienceDirect

Journal of Physics and Chemistry of Solids

journal homepage: www.elsevier.com/locate/jpcs

Temperature-dependent photoreflectance of SnS crystals

T. Raadik *, M. Grossberg, J. Raudoja, R. Traksmaa, J. Krustok

Tallinn University of Technology, Ehitajate tee 5, 19086 Tallinn, Estonia

ARTICLE INFO

Article history:
Received 14 December 2012
Received in revised form
24 May 2013
Accepted 5 June 2013
Available online 15 June 2013

Keywords:
A. Photoreflectance
A. Solar cells
A. Solar energy materials

ABSTRACT

The optical properties of single-crystal SnS were studied by photoreflectance (PR) spectroscopy. Temperature-dependent PR spectra were measured in the range 20–200 K. A room-temperature bandgap energy value of $E_g = 1.317$ eV was estimated by fitting the temperature dependence of the bandgap energy obtained from the PR spectra. The vibrational properties of orthorhombic SnS were studied using Raman spectroscopy. Four vibrational modes were detected at 95, 163, 191, and 218 cm^{-1}.

1. Introduction

Orthorhombic tin monosulfide (SnS) thin films have attracted much attention because of their suitability for solar energy cells with properties such as a direct optical bandgap [1–3], p-type conductivity, and a high absorption coefficient of 10^4–10^5 cm^{-1} [2,3]. SnS, a group IV–VI semiconductor, is a cheap and abundant material with low toxicity. Theoretical calculations revealed conversion efficiency of up to 25% for SnS photovoltaic devices [4]. The highest value reported so far for an inorganic–organic heterojunction solar cell based on SnS-sensitized mesoporous spherical TiO_2 electrodes is 2.8% [5]; however, thin-film SnS solar cells have shown efficiency of only ~2.04% [6].

Although the optical properties of SnS have been studied for over 30 years, there are still some open questions. The room-temperature bandgap energy reported for SnS varies in the range 1.1–1.87 eV and the correct value is still unclear [1–3,7]. Kim and George investigated SnS epitaxial films grown by atomic layer deposition on glass substrates and found a bandgap energy of $E_g = 1.87$ eV [1]. Reddy et al. calculated bandgap energy of $E_g = 1.47$ eV from transmittance spectra for SnS films prepared by thermal evaporation [2]. SnS films deposited by chemical bath deposition had bandgap energies of 1.75 and 1.12 eV for zinc blende and orthorhombic structures, respectively [3]. Lambros et al. found bandgap energies of 1.14 and 1.10 eV for SnS single crystals from absorption and reflectance spectra, respectively [7]. Large differences in the bandgap values could be caused by other phases such as SnS_2 and Sn_2S_3 in the films, as described by Cheng and Conibeer [8], or by change in absorption edge due to an indirect transition at lower energy. Additional studies using controlled single-phase samples and different experimental methods are needed to solve these discrepancies.

Photoreflectance (PR) has been widely used as a general method for studying the optical and electrical properties of semiconductors [9]. Because it is non-destructive and requires no electrical contact, PR is one of the most useful among modulated spectroscopy techniques. Here we present PR data for monocrystalline SnS measured over a wide temperature range.

2. Experimental

SnS was synthesized from Proanalysi grade Sn and 3 N purity S. The precursors were mixed and sealed in an evacuated quartz ampoule and inserted into a furnace. The furnace was slowly heated to 700 °C over 100 h and then kept at that temperature for 24 h before cooling to room temperature. The resulting polycrystals were then sealed in an evacuated ampoule for sublimation. The part of the ampoule in which the SnS powder was located was kept at ~650 °C and SnS single crystals grew in the part at a lower temperature zone of 620 °C. The sublimation process was allowed to run for 3 weeks. The single SnS crystals obtained had a plate-like shape with a good reflecting surface and were approximately 3 mm × 3 mm in size.

Raman spectral measurements were made at room temperature on a high resolution micro-Raman spectrometer (Horiba JobinYvon HR800) equipped with a multichannel CCD detection system in the backscattering configuration. An Nd-YAG laser ($\lambda = 532$ nm) with a spot size of 10 μm in diameter was used for excitation. X-Ray diffraction (XRD) measurements were performed using a Bruker D5005 diffractometer (Bragg–Brentano geometry) with Cu $K_{\alpha 1}$ radiation ($\lambda = 1.5406$ Å) at 40 kV and 40 mA and a

* Corresponding author. Tel.: +372 620 3210; fax: +372 620 3367.
E-mail address: taavi.raadik@ttu.ee (T. Raadik).

0022-3697/$ - see front matter © 2013 Elsevier Ltd. All rights reserved.
http://dx.doi.org/10.1016/j.jpcs.2013.06.002

graphite monochromator. The ICDD PDF-4+2012 database was used for identification. The XRD pattern obtained for an SnS monocrystal is shown in Fig. 1. All the XRD peaks closely match those for orthorombic SnS. Lattice constants of $a=1.1200$ nm, $b=0.3980$, and $c=0.4320$ nm were obtained for the crystal.

PR measurements were made using a traditional setup [9] with a 40-cm grating monochromator and a 250-W halogen bulb as the primary beam and a 51-mW solid-state laser ($\lambda=405$ nm) as the secondary beam. The reflectance signal at 85 Hz was detected using a Si detector and a lock-in amplifier. The single crystals investigated were glued onto the cold finger of a closed-cycle He cryostat with cryogenic grease.

3. Results and discussion

Four main peaks are evident in the Raman spectra (Fig. 2). The most intense peak is at 191 cm^{-1} and the others are at 95, 163, and 218 cm^{-1}. According to the literature, these can be attributed to orthorombic SnS [8,10,11]. The presence of additional phases could not be detected from the Raman data. The Raman spectra were fitted using Lorentzian functions to resolve the peaks. The lattice vibrations at 95, 191 and 218 cm^{-1} correspond to the A_g modes, and the peak at 163 cm^{-1} to the $B_{3\,g}$ mode of SnS [10].

PR spectra at three different temperatures are shown in Fig. 3 for measurements in the temperature range 20–200 K. As the temperature increases, the PR signal shifts to lower energy and decreases in intensity, as observed from the scale factors.

Each PR spectrum was analyzed by fitting the data to a low-field line-shape function with a third-derivative functional form [12]:

$$\Delta R/R = \mathrm{Re}\left[Ae^{i\varphi}(E-E_g+i\Gamma)^{-m}\right], \quad (1)$$

where E is the photon energy, A is the amplitude, φ is the phase, E_g is the bandgap energy, and Γ is the spectral broadening parameter. The exponent m depends on the type of critical point and determination of a suitable value is of particular importance in analyzing PR spectra. A value of $m=3$, corresponding to a two-dimensional critical point, did not give a good fitting result. Therefore, $m=2.5$, corresponding to a three-dimensional critical point, was used for PR spectral fitting since this yielded an excellent fit for the majority of our data.

The temperature dependence of the bandgap energy obtained by fitting the PR spectra to Eq. (1) is plotted in Fig. 4. Experimental data were fitted to the O′Donnell expression [13]

$$E_g(T) = E_g(0) - S\langle\hbar\omega\rangle\left[\coth\left(\langle\hbar\omega\rangle/2kT\right)-1\right], \quad (2)$$

where $E_g(0)$ is the bandgap energy at 0 K, S is a dimensionless coupling constant, and $\langle\hbar\omega\rangle$ is the average phonon energy. The fitting parameters obtained were $E_g(0)=1.375\pm0.001$ eV, $S=1.86\pm0.21$ and $\langle\hbar\omega\rangle=24.3\pm3.0$ meV. By extrapolating the fitting result to the O′Donnell equation for higher temperatures it is possible to estimate the bandgap energy at room temperature, resulting in $E_g=1.317$ eV. The average phonon energy of $\langle\hbar\omega\rangle=$ 24.3 meV $=196\ cm^{-1}$ is very close to the value of 191 cm^{-1} measured by Raman spectroscopy (Fig. 2).

Fig. 4 shows the temperature dependence of the bandgap energy for SnS obtained by Parenteau and Carlone [14] for comparison. The comparison reveals differences in bandgap energy values and their temperature-dependent behavior. Different samples and

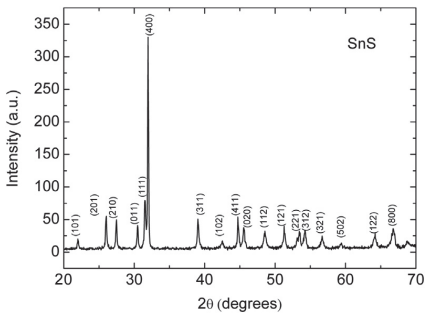

Fig. 1. XRD pattern for SnS monocrystals.

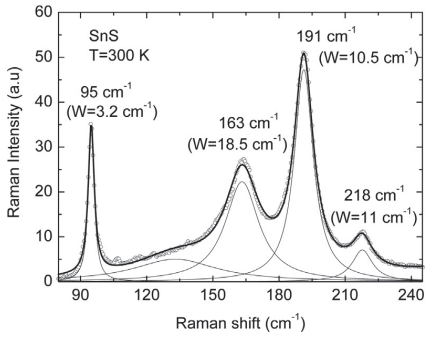

Fig. 2. Room-temperature Raman spectrum for single-crystal SnS.

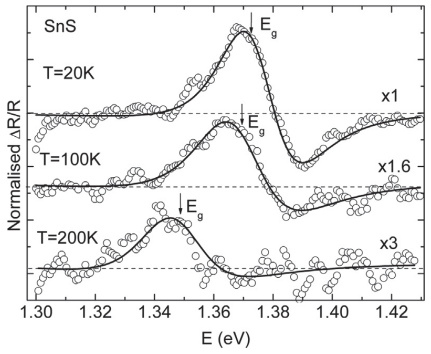

Fig. 3. Temperature-dependent PR spectra for single-crystal SnS. Circles show experimental results and continuous lines are the fitting results according to Eq. (1).

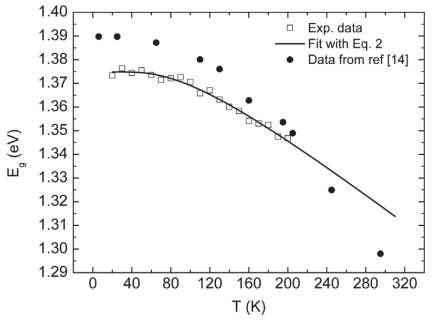

Fig. 4. Bandgap energy values for single-crystal SnS determined by fitting the PR spectra as a function of temperature, the data fit to Eq. (2), and data reported by Parenteau and Carlone [14].

measurement methods could be the reason for this discrepancy. Parenteau and Carlone used optical absorption for bandgap studies [14] while we used PR. These disparities confirm the need for further studies of the properties of SnS.

4. Conclusion

PR of monocrystalline SnS was investigated in the temperature range 20–200 K. The PR data obtained were analyzed by fitting the spectra to a low-field line-shape function, from which the bandgap energy at different temperatures was determined. The temperature dependence of the bandgap energy was fitted using the O′Donnell expression. The O′Donnell model gives a room-temperature bandgap estimate of 1.317 eV.

Acknowledgements

This research was supported by Estonian Science Foundation grants 8282 and 9369, target financing by the Estonian Ministry of Education and Research (No. SF0140099s08), the Estonian Centre of Excellence in Research "High-Technology Materials for Sustainable Development" (project TK117T), the Estonian Governmental Program for New Energy Technologies (project AR 10128), and by graduate school "Functional Materials and Technologies" funding from the European Social Fund under project 1.2.0401.09-0079 in Estonia.

References

[1] J.Y. Kim, S.M. George, J. Phys. Chem. C 114 (2010) 17597–17603.
[2] N.K. Reddy, Y.B. Hahn, M. Devika, H.R. Sumana, K.R. Gunasekhar, J. Appl. Phys. 101 (2007) 093522.
[3] C. Gao, H. Shen, L. Sun, Z. Shen, Mater. Lett. 65 (2011) 1413–1415.
[4] R.H. Bube, Photovoltaic Materials, Imperial College Press, London, 1998.
[5] W. Guo, Y. Shen, M. Wu, T. Ma, Chem. Commun. (2012) 6133–6135.
[6] P. Sinsermsuksakul, K. Hartman, R.G. Gordan, Appl. Phys. Lett. 102 (2013) 053901.
[7] A.P. Lambros, D. Geraleas, N.A. Economou, J. Phys. Chem. Solids 35 (1974) 537–541.
[8] S. Cheng, G. Conibeer, Thin Solid Films 520 (2011) 837–841.
[9] T. Raadik, J. Krustok, M.V. Yakushev, Physica B 406 (2011) 418–420.
[10] H.R. Chandrasekhar, R.G. Humphreys, U. Zwick, M. Cardona, Phys. Rev. B 15 (1977) 2177–2183.
[11] S. Sohila, M. Rajalakshmi, C. Gosh, A.K. Arora, C. Muthamizhchelvan, J. Alloys Compd. 509 (2011) 5843–5847.
[12] D.E. Aspnes, in: M. Balkanski (Ed.), Handbook on Semiconductors II, North-Holland, Amsterdam, 1980, p. 109.
[13] K.P. O′Donnell, X. Chen, Appl. Phys. Lett. 58 (1991) 2924–2926.
[14] M. Parenteau, C. Carlone, Phys. Rev. B 41 (1990) 5227–5234.

Appendix A

Article IV

M.V. Yakushev, P. Maiello, **T. Raadik**, M.J Shaw, P.R. Edwards, G. Zoppi, J. Krustok, A.V. Mudryi, I. Forbes and R.W. Martin. Electronic and Structural Characterisation of Cu_3BiS_3 Thin Films for the Absorber Layer of Sustainable Photovoltaics. *Thin Solid Films* 562 (2014), 195-199.

Thin Solid Films 562 (2014) 195–199

Contents lists available at ScienceDirect

Thin Solid Films

journal homepage: www.elsevier.com/locate/tsf

Electronic and structural characterisation of Cu_3BiS_3 thin films for the absorber layer of sustainable photovoltaics

M.V. Yakushev [a,b,*], P. Maiello [c], T. Raadik [e], M.J. Shaw [a], P.R. Edwards [a], J. Krustok [e], A.V. Mudryi [a,d], I. Forbes [c], R.W. Martin [a]

[a] Department of Physics, SUPA, University of Strathclyde, Glasgow G4 0NG, UK
[b] URFU and Ural Branch of RAS, 620002 Ekaterinburg, Russia
[c] Northumbria Photovoltaics Applications Centre, Northumbria University, Ellison Building, Newcastle upon Tyne NE1 8ST, UK
[d] Scientific-Practical Material Research Centre of the National Academy of Science of Belarus, P. Brovki 19, 220072 Minsk, Belarus
[e] Tallinn University Technology, Ehitajate tee 5, Tallinn 19086, Estonia

ARTICLE INFO

Article history:
Received 1 November 2013
Received in revised form 10 April 2014
Accepted 11 April 2014
Available online 26 April 2014

Keywords:
Thin films
Solar cells
Semiconductors
Electronic structure
Raman spectroscopy
Photoreflectance
Photoluminescence

ABSTRACT

Thin films of *p*-type Cu_3BiS_3 with an orthorhombic wittichenite structure, a semiconductor with high potential for thin film solar cell absorber layers, were synthesised by thermal annealing of Cu and Bi precursors, magnetron sputtered on Mo/glass substrate, with a layer of thermo-evaporated S. The elemental composition, structural and electronic properties are studied. The Raman spectrum shows four modes with the dominant peak at 292 cm^{-1}. Photoreflectance spectra demonstrate two band gaps E_{gX} and E_{gY}, associated with the X and Y valence sub-bands, and their evolution with temperature. Fitting the temperature dependencies of the band-gaps gives values of 1.24 and 1.53 eV for E_{gX} and E_{gY} at 0 K as well as the average phonon energy. Photoluminescence spectra at 5 K reveal two bright and broad emission bands at 0.84 and 0.99 eV, which quench with an activation energy of 40 meV. The photocurrent excitation measurements demonstrate a photoresponse and suggest a direct allowed nature of the band gap.

1. Introduction

Large scale fabrication of thin film solar cells requires the development of photovoltaic (PV) technologies based on cheap and non-toxic elements abundant in the Earth's crust. The current leaders for single junction thin film solar cells [1], namely $Cu(InGa)Se_2$ and CdTe-based devices, have shown major successes but their large scale manufacture faces difficulties due to the limited availability of indium (In) and gallium (Ga) as well as of selenium (Se) and tellurium (Te) [2], and also due to toxicity issues with Se, Cd and Te. There is therefore a high demand for semiconductor compounds for solar cell absorber layers containing low cost, non-toxic, and easy to mine elements with high world reserves. A prime candidate for this is $Cu_2ZnSn(SSe)_4$, which is a further development of $CuInSe_2$ where rare and expensive In/Ga are substituted with cheap and abundant Zn and Sn, alternating in the lattice on the indium site of the chalcopyrite structure [3,4]. However the complexity of this compound could be too challenging due to a very narrow single phase region in its phase diagram resulting in a variety of secondary phases present in the material [3].

Alternative ternary semiconductors based on Cu, S and Bi, a non-toxic element with an estimated reserve exceeding those of In and Ga by two orders of magnitude [5], are potential candidates. One of the leading among these is the natural mineral wittichenite Cu_3BiS_3 with an orthorhombic crystal structure and direct band gap [6,7]. This compound also has a high absorption coefficient of ~10^5 cm^{-1} and can be *p*-type doped [8,9].

However the basic electronic properties vital for development of Cu_3BiS_3 photovoltaic devices are almost unexplored, as reflected in the wide scatter of reported experimentally determined bandgap values from 1.14 [7] to 1.41 eV [8]. Theoretical studies of this compound suggested an indirect band gap of 1.69 eV while the smallest direct band gap was estimated to be of 1.79 eV [10]. A study on defect states and surface passivation of *p*-type Cu_3BiS_3 has recently been reported [11]. Theoretical studies suggest that doping Cu_3BiS_3 with oxygen can be used for the formation of an intermediate band (IB) extending theoretical limit of conversion efficiency for Cu_3BiS_3-based IB solar cell to 46% [12]. There are no publications on experimental studies of the electronic band structure. Neither photoluminescence (PL) nor Raman spectra have been reported.

The most common technique for bandgap measurement is optical absorption. However, multinary compounds can often have deep potential fluctuations [13] generating tails in the absorption spectra [14]

* Corresponding author at: Department of Physics, SUPA, University of Strathclyde, Glasgow G4 0NG, UK.
E-mail address: michael.yakushev@strath.ac.uk (M.V. Yakushev).

http://dx.doi.org/10.1016/j.tsf.2014.04.057

making such analysis difficult. Therefore the bandgap energy calculated from the absorption spectrum could often be incorrect. More reliable techniques for measuring the bandgap are electro- or photoreflectance modulation methods [15].

In this paper we report the fabrication of photosensitive thin films of Cu_3BiS_3 by thermal annealing of metal precursors with a layer of thermo-evaporated S and detailed characterisation of their structural, optical and electronic properties.

2. Experimental details

Thin films of Cu_3BiS_3 were fabricated using a two stage process. At first 0.3 μm thick precursor layers of Cu and Bi were magnetron sputtered on Mo-coated soda-lime glass from 5 N-purity elemental targets. 1.5 μm thick films of 4 N-purity sulphur were thermally evaporated on these precursor layers. Then such structures were heated for 30 min at a temperature of 250 °C in Ar atmosphere at a pressure of 100 Pa. An excess of sulphur was provided in order to ensure full sulphurisation of the precursor layer during the heating process. Hot probe measurements revealed *p*-type conductivity of the synthesised Cu_3BiS_3 material. More information on the synthesis of sulphide compound films by chalcogenisation of magnetron deposited multilayer metallic precursors with a layer of sulphur can be found in references [16–19].

The morphology of the deposited films was analysed using a low-vacuum FEI Quanta FEG 250 environmental scanning electron microscope (SEM) at an electron beam energy of 30 keV. The elemental composition and lateral homogeneity were studied by Cameca SX100 wavelength-dispersive X-ray (WDX) microanalysis at an electron beam energy of 5 keV. The structural properties and the presence of secondary phases were examined by Raman spectroscopy and X-ray diffraction. X-ray diffraction (XRD) measurements were performed using a Bruker D5005 diffractometer (Bragg–Brentano geometry) with Cu Kα1 radiation (λ1/41.5406 Å) at 40 kV and 40 mA and a graphite monochromator.

Photoresponse was measured by immersing the films in a glass cell with 0.2 M aqueous solution of $Eu(NO_3)_3$, as electron scavenging redox electrolyte, using a three electrode configuration with Ag/AgCl reference electrode, counter platinum electrode as well as the molybdenum back contact. Samples were illuminated with 75 Hz chopped monochromated light from a tungsten halogen lamp. The measured photo-current was maximised by adjusting the potential with respect to the reference electrode. Photo-current excitation spectra were recorded using a standard Bentham lock-in amplifier and then normalised against calibrated silicon and germanium photodiodes. Such normalised spectra correspond to the apparent quantum efficiency (AQE).

The photoreflectance (PR) measurements were carried out at temperatures from 10 to 300 K using a 40 cm focal length single grating monochromator, Si detector and closed-cycle helium cryostat. Monochromated light from a halogen lamp was employed as the primary beam whereas the 85 Hz modulated 405 nm line of an 80 mW solid state laser was used as the secondary, pumping beam source. The photoluminescence (PL) measurements were carried out using a 1 m focal length single grating monochromator and the 514 nm line of a 200 mW Ar^+ laser for excitation and either a closed-cycle helium cryostat for temperature resolved measurements or a liquid helium cryostat to analyse excitation intensity dependencies. The PL signal was detected by either an InGaAs photomultiplier tube (PMT) or a photodiode for measurements in the spectral ranges from 0.9 to 1.7 μm and 0.9 to 1.9 μm, respectively.

3. Results and discussion

The cross-section and surface views of the film, shown in Fig. 1(a) and (b), respectively, demonstrate a dense homogeneous layer with an average thickness of 0.7 μm. The cross-section in Fig. 1(a) demonstrates that the film structure is columnar with the column diameter of 0.1 μm.

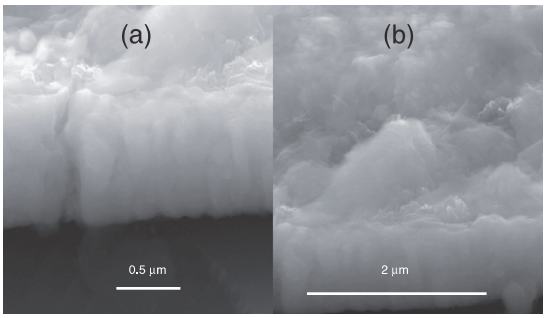

Fig. 1. Cross sectional (a) and surface (b) SEM micrograph views of the Cu_3BiS_3 films.

WDX analysis of the film indicates an elemental composition of 42.4 at.% Cu, 14.7 at.% Bi and 42.9 at.% S with a statistical uncertainty of ±0.6 at.%. This gives a formula of $Cu_{3.00}Bi_{1.04}S_{3.03}$ with uncertainties of ±0.04. A beam energy of 5 keV corresponds to a sampling depth of approximately 0.1 μm. A WDX line-scan across several millimetres of the surface demonstrates good lateral homogeneity of the films, as shown in Fig. 2.

The XRD pattern of the film along with the standard (pdf: 043-1479) orthorhombic pattern shown in Fig. 3 reveals the formation of a wittichenite lattice structure (with the lattice parameters a = 0.7661 nm, b = 1.0388 nm, c = 0.6712 nm), peaks associated with metallic molybdenum and bismuth implying the presence of Bi clusters.

Raman spectra, measured at different points of the films at room temperature, consistently reveal four modes at 96, 125, 264 and 292 cm^{-1} as shown in Fig. 4. The dominant peak at 292 cm^{-1} has a full width at half maximum (FWHM) of 12 cm^{-1}.

The electronic structure of Cu_3BiS_3 was analysed using PR. A modulation of the built-in electric field, created by the surface band bending due to the photo-injection of electron–hole pairs by a chopped incident laser beam, generates differential changes of the complex dielectric function and the amplitude of the PR signal $\Delta R/R$ [15]. Fig. 5 shows room temperature PR spectra, which demonstrate a strong resonance at 1.2 eV.

Decreasing the temperature down to 80 K shifts this resonance towards higher energies and reveals a second resonance at 1.5 eV. Further decrease of temperature, down to 10 K, shifts the resonances further towards higher energies and makes both resonances sharper as

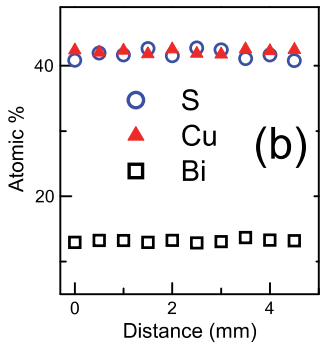

Fig. 2. WDX line-scan of the S, Bi and Cu elemental composition.

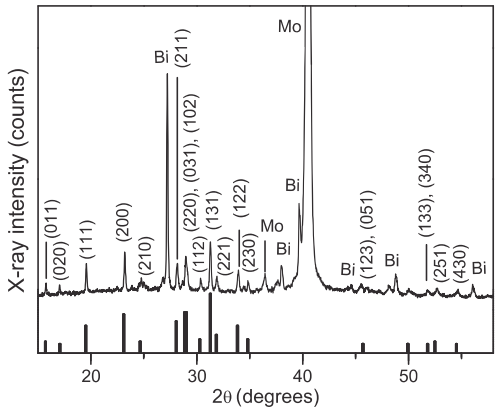

Fig. 3. XRD pattern of Cu_3BiS_3 on Mo coated glass in comparison with standard wittichenite orthorhombic pattern.

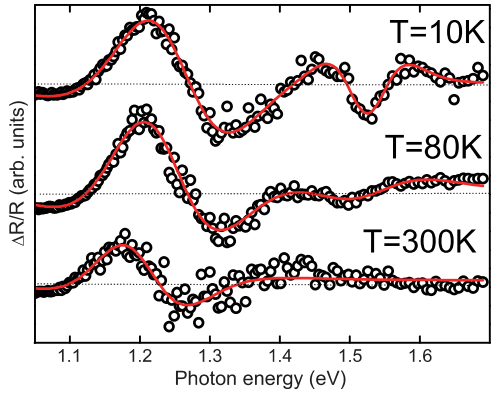

Fig. 5. PR spectra of Cu_3BiS_3 films at different temperatures (b); symbols are experimental PR spectra, and the curves are best fits using Eq. (1). Temperature dependence of the X and Y bandgap energies (c); symbols are experimental E_g, and the curves are best fits using Eq. (2).

shown in Fig. 5. The experimental PR spectra were fitted with the function [20,21],

$$\Delta R/R = \mathrm{Re}\left[\sum_{j=1}^{p} C_j e^{i\theta_j}\left(E - E_{g,j} + i\Gamma_j\right)^{-m}\right] \quad (1)$$

where E is photon energy, C_j, θ_j, $E_{g,j}$ and Γ_j are the amplitude, phase, transition energy and broadening parameter of each resonance, respectively, p is the number of resonances and i is the imaginary unit. A two resonance ($p = 2$) fit was used for low temperature PR spectra. The m parameter is defined by the type of the critical point and $m = 5/2$, corresponding to interband transitions and a three-dimensional critical point, has been assumed for the calculations. The fitted curves for the temperature 10, 80 and 300 K are shown by solid lines in Fig. 5.

Values for E_g for different temperatures, determined using the best fits, are shown in Fig. 6. The presence of two band gaps can be associated with splitting of the valence band. Such splitting has been reported for ternary I–III–IV_2 semiconductor compounds with chalcopyrite structure [22,23]. Measurements on $AgInS_2$, a semiconductor compound which crystallises in two different phases chalcopyrite and orthorhombic, reveal a splitting of the valence band into three sub-bands for both of them [24]. In the chalcopyrite phase the splitting into A, B and C sub-bands occurs due to the simultaneous influence of the crystal field and spin orbit interaction whereas in the orthorhombic one a splitting into X, Y and Z sub-bands is considered to be solely due to the influence of the crystal field. For the orthorhombic structure of Cu_3BiS_3 we use the notations X and Y for the top two bands.

The temperature dependencies of E_{gX} and E_{gY} were fitted with the expression introduced by O'Donnell and Chen [25],

$$E_g(T) = E_g(0) - S\langle\hbar\omega\rangle / \left[\coth\left(\langle\hbar\omega\rangle/2kT\right) - 1\right] \quad (2)$$

where $E_g(0)$ is the bandgap energy at 0 K, S is a dimensionless coupling constant and $\langle\hbar\omega\rangle$ represents an average phonon energy. The solid curves in Fig. 6 are the best fits of the $E_g(T)$ values using Eq. (2) with the fitting parameters shown in Table 1. The determined average phonon energies are in the range of the measured energies of the Raman modes.

Fig. 6 demonstrates a strong decrease of both energy gaps with increasing temperature so at room temperature $E_g(X) = 1.18$ eV. A reduction in the splitting of the valence bands, from 0.28 eV at 10 K to 0.27 eV at 100 K can also be observed.

PL spectra provide information on the mechanisms of radiative recombination and the nature of defects [26]. The low temperature (4.2 K) PL spectrum in Fig. 7, measured with the extended range detector, contains two non-resolved broad bands: A1 at about 0.99 eV with a full width at half maximum (FWHM) of 160 meV and (A2) at 0.84 eV with a FWHM of 140 meV. The relative intensities of the bands vary at

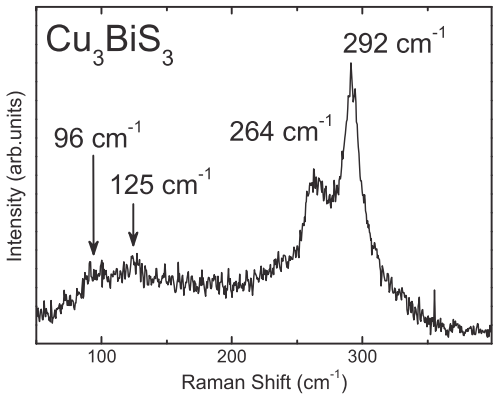

Fig. 4. Raman spectra of the Cu_3BiS_3 thin films.

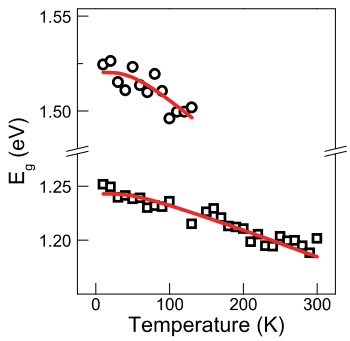

Fig. 6. Temperature dependence of the X and Y bandgap energies E_g; symbols are experimental E_g, and the curves are best fits using Eq. (2).

Table 1
The bandgap E_g, coupling constant S and average phonon energy $<\hbar\omega>$ for the X and Y valence bands, determined by fitting the experimental temperature dependencies of E_g using Eq. (2).

Valence band	E_g (0), eV	S	$<\hbar\omega>$, meV
X	1.24	0.54	6
Y	1.53	0.70	20

different points on the sample, but their spectral positions remain the same.

The dependence of the total integrated PL intensity (I) of both bands on increasing laser power P was fitted to the equation $I \sim P^{\gamma}$. A determined value of $\gamma \approx 0.71$ suggests that these bands are associated with defect related transitions [27]. No significant spectral shifts were observed as the excitation laser power density was increased from 0.26 to 2 W/cm^2.

The PL intensity of the A1 band increases at a greater rate than that of the A2 band, as clearly seen in Fig. 8 which shows spectra excited with laser power densities of 0.26, 0.78 and 2 W/cm^2 and normalised to the A2 band intensity for 2 W/cm^2. The low energy tail of the A2 band is cut-off beyond the 1.7 μm limit of the PMT used for this measurement.

The temperature dependence of the PL spectra from 5 to 90 K is shown in Fig. 9(a). These spectra reveal significant water absorption at 0.9 eV. The spectral positions of the A1 and A2 bands do not shift within this temperature range. Also the A1 band is seen to quench at a greater rate than A2. An Arrhenius plot of the temperature quenching for the integrated intensity of both bands I is shown in Fig. 9(b), revealing a straight line region between 50 and 90 K.

The best fit of the experimental data points in this region was achieved assuming one recombination channel model $I(T) = I_0 [1 + Aexp(-E_a / kT)]$, where I_0 (intensity at the lowest temperature), E_a (activation energy) and A are the fitting parameters and k is the Boltzmann constant. An activation energy of 40 ± 4 meV is determined.

The excitation intensity and temperature analysis of the bands suggests a preliminary interpretation as the recombination of electrons bound to deep donors and holes bound to deep acceptors [28]. According to this model, recombination of electrons and holes of close highly localised donors and acceptors with different spatial separations can generate several peaks each corresponding to a particular separation.

An increase in the laser intensity leads to recombination of closer located donor–acceptor pairs, which have greater Coulomb energy. This redistributes the intensity towards higher energy peaks.

For merged peaks this process results in a spectral shift of the PL band maximum towards higher energy with increasing laser power, whereas redistribution of intensities is a characteristic of non-merged

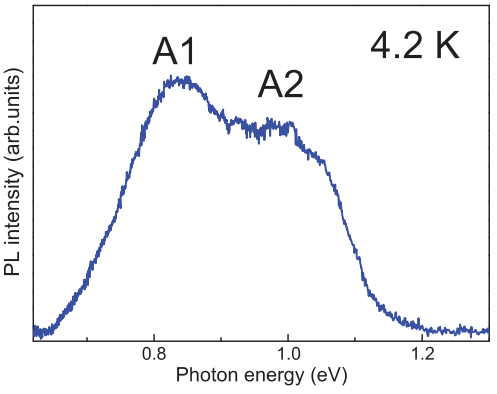

Fig. 7. Extended PL spectrum of Cu_3BiS_3.

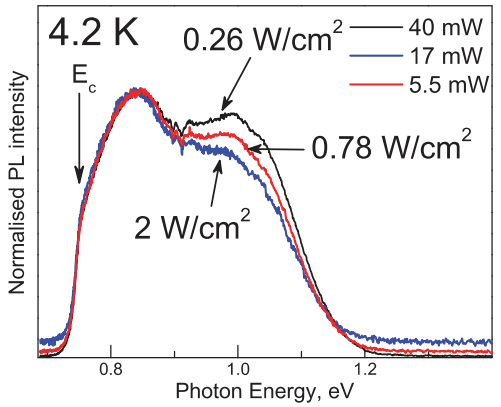

Fig. 8. Normalised PL spectra at different excitation powers (E_c is the detector cut-off energy).

peaks. Ionisation of a shallower defect, located at 40 meV from the valence or conduction band, can cause the observed temperature quenching of both bands. An AQE spectrum, shown in Fig. 10(a), demonstrates a photoresponse of about 1% in the photon range of 1.1–2.3 eV. A similar photoresponse also measured using Eu^{+3} electrolyte has been reported in [9]. Varying the potential with respect to the reference electrode the authors of [9] derived the doping density values. AQE depends on absorption coefficient α as [29],

$$AQE = 1 - \exp(-\alpha W), \tag{3}$$

where W is the width of the space charge region. For a direct allowed transition, the dependence of the absorption coefficient on the photon energy $h\nu$ should follow the relation,

$$\alpha h\nu \propto \left(h\nu - E_g\right)^{1/2}, \tag{4}$$

Therefore $[h\nu\, ln(1 - AQE)]^2$, as a function of photon energy $h\nu$, should follow a straight line. Fig. 10(b) demonstrates a clear linearity of the $[h\nu\, ln(1 - AQE)]^2$ dependence on $h\nu$ suggesting a direct allowed nature of the bandgap in Cu_3BiS_3. Extending this line to the intersection with the $h\nu$ axis, as shown in Fig. 10(b), gives an estimate of E_g = 1.22 eV which is close to that determined from PR measurements at room temperature.

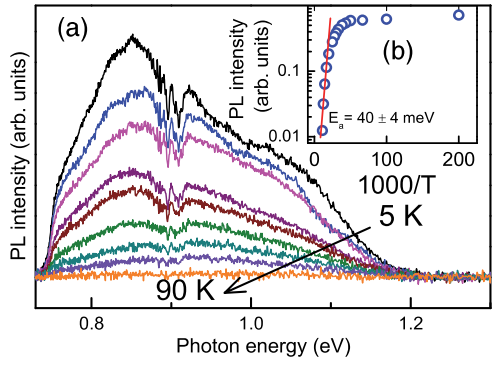

Fig. 9. Temperature dependence of the PL spectra (a), Arrhenius plot of the temperature quenching of the A1 and A2 band integrated intensity (o experimental data, – fitted straight line) (b).

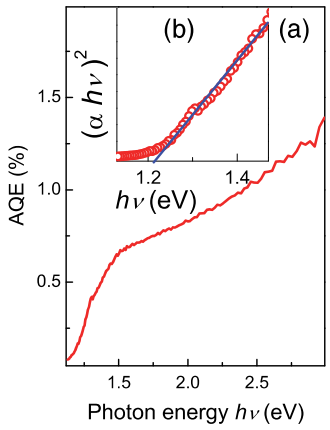

Fig. 10. Apparent quantum efficiency of the Cu_3BiS_3 film (a), the dependence of $[\alpha h\nu]^2$ on $h\nu$ and estimation of E_g (b).

4. Conclusion

Thin films of *p*-type Cu_3BiS_3 with good lateral homogeneity and wittichenite orthorhombic lattice structure have been synthesised by thermal annealing of Cu and Bi precursor, magnetron sputtered on Mo/glass substrate, with a layer of thermo-evaporated S. Photoreflectivity spectra at 10 K reveal two band gaps, at 1.24 and 1.53 eV, which were associated with the X and Y valence sub-bands, respectively, split due to the crystal field influence. Two broad emission bands at 0.99 and 0.84 eV were observed in the PL spectra at low temperatures. Excitation power changes did not shift the bands causing a redistribution of PL intensity towards the higher energy band. Both bands were quenching at a temperature of 90 K. An activation energy of 40 meV was determined by the Arrhenius analysis of the quenching. The photocurrent excitation spectra demonstrate a photoresponse of the films and suggest a direct allowed nature of the band gap.

Acknowledgements

This work was supported by the EPSRC Materials in Engineering (4.5.01), SUPERGEN programme “Photovoltaics for the 21st Century”, KTF, BCFR (F11MC-021), RFBR grants 11-03-00063, 13-03-96032, 12-U3-1006, and 14-02-00080 and Estonian Science Foundation Grant G-8282.

References

[1] M.A. Green, K. Emery, Y. Hishikawa, W. Warta, Solar cell efficiency tables (version 37), Prog. Photovolt. Res. Appl. 19 (2011) 84.
[2] B.A. Andersson, Materials availability for large-scale thin-film photovoltaics, Prog. Photovolt. Res. Appl. 8 (2000) 61.
[3] S. Siebentritt, S. Schorr, Kesterites—a challenging material for solar cells, Prog. Photovoltaics 20 (2012) 512.
[4] F. Luckert, D.I. Hamilton, M.V. Yakushev, N. Beattie, G. Zoppi, M. Moynihan, I. Forbes, A.V. Karotki, A.V. Mudryi, M. Grossberg, J. Krustok, R.W. Martin, Optical properties of high quality $Cu_2ZnSnSe_4$ thin films, Appl. Phys. Lett. 99 (2011) 062104-1.
[5] U.S.Geological survey, Mineral Commodity Summaries, January 2012.
[6] P.K. Nair, L. Huang, M.T.S. Nair, H. Hu, E.A. Meyers, R.A. Zingaro, Formation of p-type Cu_3BiS_3 absorber thin films by annealing chemically deposited Bi_2S_3–CuS thin films, J. Mater. Res. 12 (1997) 651.
[7] V. Estrella, M.T.S. Nair, P.K. Nair, Semiconducting Cu_3BiS_3 thin films formed by the solid-state reaction of CuS and bismuth thin films, Semicond. Sci. Technol. 18 (2003) 190.
[8] F. Mesa, G. Gordillo, Effect of preparation conditions on the properties of Cu_3BiS_3 thin films grown by a two-step process, J. Phys. Conf. Ser. 167 (012019) (2009) 1.
[9] D. Colombara, L.M. Peter, K. Hutchings, K.D. Rogers, S. Schäfer, J.T.R. Dufton, M.S. Islam, Formation of Cu_3BiS_3 thin films via sulfurization of Bi–Cu metal precursors, Thin Solid Films 520 (2012) 5165.
[10] M. Kumar, C. Persson, Cu_3BiS_3 as a potential photovoltaic absorber with high optical efficiency, Appl. Phys. Lett. 102 (2013) 062109-1.
[11] F. Mesa, G. Gordillo, Th. Dittrich, K. Ellmer, R. Baier, S. Sadewasser, Transient surface photovoltage of p-type Cu_3BiS_3, Appl. Phys. Lett. 96 (2010) 082113-1.
[12] C. Tablero, Photovoltaic application of O-doped Wittichenite-Cu_3BiS_3: from microscopic properties to maximum efficiencies, Prog. Photovolt. Res. Appl. 21 (2013) 894.
[13] J. Krustok, H. Collan, M. Yakushev, K. Hjelt, The role of spatial potential fluctuations in the shape of the PL bands of multinary semiconductor compounds, Phys. Scr. T79 (1999) 179.
[14] I. Dirnstorfer, Mt. Hofmann, M.D. Lampert, F. Karg, B.K. Meyer, CuIn(Ga)Se_2 solar cells: characterization of the absorber material, Inst. Phys. Conf. Ser. 152 (1998) 233.
[15] F.H. Pollak, H. Shen, Modulation spectroscopy of semiconductors: bulk/thin film, microstructures, surfaces/interfaces and devices, Mater. Sci. Eng. R10 (1993) 275.
[16] D. Colombara, L.M. Peter, K.D. Rogers, K. Hutchings, Thermochemical and kinetic aspects of the sulfurization of Cu–Sb and Cu–Bi thin films, J. Solid State Chem. 186 (2012) 36.
[17] B.M. Basol, V.K. Kapur, Deposition of $CuInSe_2$ films by a two-stage process utilizing E-beam evaporation, IEEE Trans. Electron Devices 37 (1990) 418.
[18] I. Forbes, K. Reddy, D. Johnston, R.W. Miles, D.W. Lane, K.D. Rogers, A. Chapman, R.f. sputtering of high-quality Cu/In precursor layers and conversion to $CuInS_2$ using elemental sulfidization processes, J. Mater. Sci. Mater. Electron. 14 (2003) 567.
[19] P. Maiello, G. Zoppi, R.W. Miles, N. Pearsall, I. Forbes, Chalcogenisation of Cu–Sb metallic precursors into Cu3Sb(SexS1 — x)3, Sol. Energy Mater. Sol. Cells 113 (2013) 186.
[20] D.E. Aspnes, in: M. Balkanski (Ed.), Handbook on Semiconductors II, vol. 2, North-Holland, Amsterdam, 1980, p. 109, (Chap. 4A).
[21] T. Raadik, J. Krustok, M.V. Yakushev, Photoreflectance study of AgGaTe2 single crystals, Phys. B Condens. Matter 406 (2011) 418.
[22] M.V. Yakushev, F. Luckert, C. Faugeras, A.V. Karotki, A.V. Mudryi, R.W. Martin, Diamagnetic shift of the A free exciton in CuGaSe2, Appl. Phys. Lett. 97 (2010) 152110-1.
[23] J.L. Shay, J.H. Wernick, Ternary Chalcopyrite Semiconductors-Growth, Electronic Properties, and Applications, Pergamon Press, Oxford, 1975.
[24] J.L. Shay, B. Tell, L.M. Schiavone, H.M. Kasper, F. Thiel, Energy bands of $AgInS_2$ in the chalcopyrite and orthorhombic structures, Phys. Rev. B 9 (1974) 1719.
[25] K.P. O'Donnell, X. Chen, Temperature dependence of semiconductor band gaps, Appl. Phys. Lett. 58 (1991) 2924.
[26] H.B. Bebb, E.W. Williams, in: R.K. Willardson, A.C. Beer (Eds.), Semiconductors and Semimetals, Academic, New York, 1972.
[27] T. Schmidt, K. Lischka, W. Zulehner, Excitation-power dependence of the near-band-edge photoluminescence of semiconductors, Phys. Rev. B 45 (1992) 8989.
[28] J. Krustok, J. Raudoja, M. Krunks, H. Mandar, H. Collan, Nature of the native deep localized defect recombination centers in the chalcopyrite and orthorhombic $AgInS_2$, J. Appl. Phys. 88 (2000) 205.
[29] J. Scragg, P.J. Dale, L.M. Peter, G. Zoppi, I. Forbes, New routes to sustainable photovoltaics: evaluation of Cu_2ZnSnS_4 as an alternative absorber material, Phys. Stat. Sol. (b) 245 (2008) 1772.

Appendix A

Article V

J. Krustok, **T. Raadik**, M. Grossberg, S. Giraldo, M. Neuschitzer, S. López-Marino, E. Saucedo. Temperature dependent electroreflectance study of $Cu_2ZnSnSe_4$ solar cells. *Materials Science in Semiconductor Processing,* (in press).

Materials Science in Semiconductor Processing ∎ (∎∎∎∎) ∎∎∎–∎∎∎

Contents lists available at ScienceDirect

Materials Science in Semiconductor Processing

journal homepage: www.elsevier.com/locate/mssp

Temperature dependent electroreflectance study of $Cu_2ZnSnSe_4$ solar cells

Jüri Krustok [a,*], Taavi Raadik [a], Maarja Grossberg [a], Sergio Giraldo [b], Markus Neuschitzer [b], Simon López-Marino [b], Edgardo Saucedo [b]

[a] Department of Materials Science, Tallinn University of Technology, Ehitajate tee 5, 19086 Tallinn, Estonia
[b] Catalonia Institute for Energy Research, IREC, Jadins de les Dones de Negre 1, 08930 Sant Adrià de Besòs, Barcelona, Spain

ARTICLE INFO

Keywords:
Kesterite
CZTSe
Electroreflectance
Bandgap

ABSTRACT

Electroreflectance measurements (ER) of $Cu_2ZnSnSe_4$ (CZTSe) solar cell were performed in the temperature range of $T=100$–300 K. ER spectra were fitted using the Lorentzian line shape functional form. The broadening parameter did not change with temperature and had very high value of 125 meV. High concentration of charged defects and spatial fluctuations of bandgap energy caused by the presence of both ordered and disordered crystal structures and/or different defect clusters are the main reasons for broadening of the ER spectra. The temperature dependence of the band-gap energy for CZTSe was determined from ER data. The overall shift of the bandgap energy was found to be only about 26 meV from room temperature to $T=0$ K.

1. Introduction

In recent years kesterite $Cu_2ZnSnSe_4$ (CZTSe) thin films have been intensively investigated as a potential low cost absorber for solar cells. $Cu_2ZnSn(S_xSe_{1-x})_4$ (CZTSSe) based thin film solar cells have achieved efficiencies as high as 12.6% [1] while CZTSe cells have shown efficiency of 11.6% [2]. However, compared to thin film solar cells with a similar band gap E_g but based on the related Cu(In,Ga)(S, Se)$_2$ absorber, CZTSe cells have lot of additional problems.

It is known from different experiments that kesterites exhibit a disorder in the Cu–Zn layers at $z=1/4$ and $z=3/4$ of the unit cell due to [Zn_{Cu}–Cu_{Zn}] antisite defect pairs [3,4]. The presence of Cu–Zn disorder and different defect clusters can significantly reduce the bandgap energy E_g [5,6]. The coexistence of ordered and disordered structures in Cu_2ZnSnS_4 (CZTS) was experimentally discovered using low temperature photoluminescence (PL) measurements [7]. It was found that the difference between bandgap energies of ordered and disordered structures is about 80 meV, the latter being smaller. Similar results have been obtained also in CZTSSe (S/Se-ratio of 8%), where using the electroreflectance the room temperature bandgap energy E_g of ordered and disordered CZTSSe was found to be 1.08 eV and 0.96 eV respectively [8]. In pure CZTSe the Cu–Zn ordering can increase E_g by 110 meV as compared to fully disordered material and therefore E_g can be used as an order parameter [9]. The critical temperature for the CZTSe order–disorder transition was found to be about 200 °C [9]. At equilibrium, the CZTSe is completely disordered if the temperature is above 200 °C. Below this critical temperature the equilibrium ordering degree increases continuously and the perfect order is reached only at 0 K. It was found that the room temperature bandgap energy E_g of ordered and disordered CZTSe is about 1.057 eV and 0.94 eV respectively [9]. Degree of

* Corresponding author. Tel.: +372 6203364; fax: +372 6203367.
E-mail addresses: juri.krustok@ttu.ee (J. Krustok), taavi.raadik@ttu.ee (T. Raadik), maarja.Grossberg@ttu.ee (M. Grossberg), sgiraldo@irec.cat (S. Giraldo), mneuschitzer@irec.cat (M. Neuschitzer), slopez@irec.cat (S. López-Marino), esaucedo@irec.cat (E. Saucedo).

http://dx.doi.org/10.1016/j.mssp.2015.04.055
1369-8001/

Cu–Zn ordering can be changed also by using different cooling rates near the critical temperature after the high temperature treatment [8,10].

It is expected that the total charged defect concentration is lower in ordered CZTSe, but recent PL measurements of CZTSe thin films [9] and also CZTS monograins did not confirm this hypothesis [10]. At the same time, the defect structure and the nature of defect complexes changed with a cooling rate. It is worth to mention that CZTSe with the lowest defect concentration so far and showing an excitonic photoluminescence emission has a room temperature bandgap energy of $E_g=1.01$ eV [11] and thus a significant quantity of Cu–Zn disordering. Besides Cu–Zn disordering the bandgap energy depends also on quality and composition of samples. These are the main reasons for a large discrepancy between reported E_g values of CZTSe in the literature.

Majority of measured CZTSe samples show properties of so-called heavily doped material. The conditions of heavy doping originate from the high concentration of native defects that is often observed in kesterites [12–14]. In a semiconductor with a random distribution of charged donors and acceptors spatial fluctuations of the electrostatic potential are formed. These potential fluctuations will lead to a local perturbation of the band structure, thus broadening the defect level distribution and forming band tails. As a result, the band gap in the heavily doped semiconductor is not well defined and is usually determined by the percolation levels of electrons and holes. This fact introduces additional problems when the bandgap energy is measured using common methods like the absorption or an external quantum efficiency (EQE) spectra. In [14] it was shown that the band gap of CZTSe can be estimated by extrapolation of the low-energy slope of the recorded EQE curve only at temperatures $T>250$ K. At lower temperatures EQE starts to decrease and this is related to a localization of generated holes inside deep valence band potential wells. It is obvious that EQE depends not only on the absorption coefficient but also on the ability of generated charge carriers to reach the front and back contacts. At $T<250$ K the mobility of holes rapidly decreases due to localization and the bulk recombination through these deep wells increases reducing the overall EQE.

At the same time not only a room temperature band gap is important but also a temperature dependence of E_g. Recently Choi et. al. [15] published their spectroscopic ellipsometry study of the dependence of the band-gap energy for CZTSe on temperature ranging from 50 to 350 K. Their thin film samples showed a room temperature bandgap energy of $E_g=0.97$ eV and according to [9], this low E_g must be related to high degree of Cu–Zn disordering. It was found that E_g of CZTSe decreases with increasing temperature, but the variation seems to be relatively small. However, the measurement of the absorber band gap in finished solar cells is often also interesting and probably gives additional information about solar cell properties. For example, in the CdTe/CdS solar cells a formation of CdS_xTe_{1-x} solid solution at the interface was detected in [18]. Moreover, it could be attractive to test a temperature dependence of E_g on samples with higher degree of ordering. Many experimental techniques have been applied to measure band gaps of CZTSe cells. One such technique is the electroreflectance spectroscopy (ER). Electroreflectance spectroscopy is staging an important role in determining the electronic structures and probing the optical properties of semiconductors due to its easy implementation and exhibition of relatively sharp spectra without noticeable background even at room temperature. Modulation of the electric field by an AC voltage in a space charge region of a thin film solar cell offers a convenient and non-destructive way to detect critical points within the region of the barrier. Recent room temperature ER measurements of CZTSSe solar cells [8] proved that this method can really be used for a band gap measurements even in highly doped kesterites. In CZTSe solar cells ER is not used before and no data about the temperature dependence of E_g in real solar cells is present.

In this paper, we report on temperature dependence of the bandgap energy E_g in CZTSe thin film solar cells detected by ER.

2. Experimental details

CZTSe absorber for this study was prepared by reactive thermal annealing of metallic prepursor stack deposited by DC magnetron sputtering onto Mo coated soda lime glass substrates, as described elsewhere in more detail [20]. The CZTSe absorber composition was measured by X-ray florescence spectroscopy showing relative cation composition of Cu=38.0%, Zn=36.7% and Sn=25.3% which results in cation ratios of Cu/(Zn+Sn)=0.61, Zn/Sn=1.45, Cu/Zn=1.04, and Cu/Sn=1.5. Highest device performance is reported in this Cu poor Zn rich compositional range and recently even for very Cu poor absorber layers performant devices with especially high Voc values are reported [24]. Solar cells were finished by depositing a CdS buffer layer by chemical bath deposition followed by DC-pulsed sputtered ZnO (50 nm) and In_2O_3:SnO_2 (90/10 wt%; 350 nm, $R_{\square}=50\ \Omega\ cm^{-1}$) window layer. Prior to CdS deposition the CZTSe absorber was etched using an oxidizing etching to remove possible ZnSe secondary phases from the surface as reported in [20]. The compositional values presented here were measured prior the specific surface etching because time between surface etching and buffer layer deposition is crucial to avoid surface contamination. Thus a reduction in Zn composition is expected in the final CZTSe absorber layer. The individual solar cell used for this study shows power conversion efficiency of $\eta=6.6\%$ with $J_{sc}=28.3$ mA cm^{-2}, $V_{oc}=368$ mV, and FF=63%.

For the electroreflectance measurements the DC- and AC-voltages were applied to a solar cell under study via back and front contacts by a pulse generator with frequency of 275 Hz, AC value of ± 0.8 V and DC component of -0.8 V. Computer controlled grating monochromator SPM-2 ($f=40$ cm) together with a 250 W quartz-tungsten halogen lamp was used for illumination. The change in reflectance ΔR and reflectance R were both measured using a lock-in amplifier (SR 810) and a Ge detector in the spectral range from 0.8 to 1.5 eV. The solar cell was mounted into a closed-cycle He cryostat to perform

Please cite this article as: J. Krustok, et al., Materials Science in Semiconductor Processing (2015), http://dx.doi.org/10.1016/j.mssp.2015.04.055

temperature dependent measurements in the range of $T=100$–300 K.

Electroreflectance can be classified into three categories: weak, intermediate and strong field regimes, depending on the strength of a local electrical field in the junction. In our case the weak field regime seems to be present. ER spectra near the fundamental band-gap energy with a weak field approach can be well fitted with a third derivative functional form (TDFF) given by Aspnes [16]

$$\frac{\Delta R}{R}=\mathrm{Re}\left[Ce^{i\varphi}(E-E_g+i\Gamma)^{-m}\right] \quad (1)$$

where E is the photon energy, C is an amplitude parameter, Φ phase parameter, E_g energy of the bandgap and Γ is a broadening parameter. The exponent m depends on the type of the critical point and is usually related to the line shape of the dielectric function (e.g., Lorentzian or Gaussian).

3. Results and discussion

Temperature dependent ER spectra together with Aspnes fit (Eq. (1)) of CZTSe cell are presented in Fig. 1. It is clearly seen that the spectrum shifts towards higher energies with decreasing temperature, but the shift is very small and the shape of ER peak remains relatively unaffected. This means that the linewidth is determined by the inhomogeneous broadening. Although the spectral fit with Eq. (1) gives good results near the critical point, we still notice some deviation at higher energies, see Fig. 1. This deviation could be an indication of a second critical point at higher energy. For example, in [15] the room temperature $E_0(C)$ bandgap of CZTSe due to spin-orbit splitting of valence band was found at 1.272 eV. However, our ER signal was too low near this energy and therefore we fitted only the main peak. The overall shape of the main peak is determined by a high concentration of charged defects and spatial fluctuations of the band edge in this compound. As a result the dielectric function will be affected and inhomogeneous broadening mechanisms start to dominate.

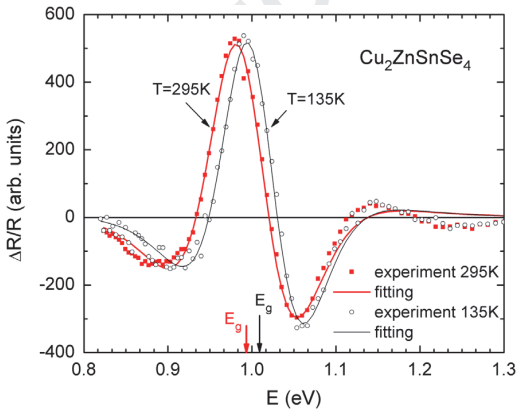

Fig. 1. ER spectra of CZTSe solar cell at temperatures 135 K and 295 K. Dots show the experimental data and continues lines are the fitting results with Eq. (1).

Moreover, the best fit was achieved using remarkably high m values $m\geq 3$. However, according to our calculations the exponent m mostly determines the line-shape of the ER spectrum far from a critical point and does not affect the spectrum near the bandgap energy E_g. An average value of the broadening parameter $\Gamma\approx 125$ meV is practically constant over the whole temperature range and one possible explanation is, that not only potential fluctuations, but also the bandgap energy fluctuations due to presence of ordered and disordered structures and/or different defect clusters [5,6,22] are affecting the inhomogeneous broadening. Very similar bandgap energy fluctuations were discovered by PL in the ternary compound $CuGa_3Se_5$ [19] and, as a rule, they lead to an abnormal widening of PL and ER bands. Therefore, the bandgap energy E_g obtained from ER fittings always represents some average value. Very wide room temperature ER spectra were measured also in CZTSSe by Krämmer et al. [8]. They noticed that, due to inhomogeneous broadening mechanisms, the resulting modulus spectra calculated from ER experiments could be better fitted with a Gaussian lineshape instead of Lorentzian. It seems that this inhomogeneous broadening due to spatial bandgap energy and potential fluctuations is a typical feature in all kesterites and does not depend on the bandgap energy. Unfortunately, ER measurements were not possible at $T<100$ K because ER signal dropped significantly. At low temperatures holes start to localize in the valence band potential wells and as a result, the series resistance of the solar cell increases considerably [14,23]. This leads to a reduction of an external electric field on a junction and accordingly ER signal drops.

The resulting band gap values for the CZTSe cells are shown in Fig. 2. The temperature dependence of E_g was fitted with the expression introduced by O'Donnell and Chen [17]:

$$E_g(T)=E_g(0)-S<\hbar\omega>\left[coth(<\hbar\omega>/2kT)-1\right], \quad (2)$$

where $E_g(0)$ is the band gap energy at 0 K, S is a dimensionless coupling constant and $\langle\hbar\omega\rangle$ represents an average phonon energy. The solid curve in Fig. 2 is the best fit of

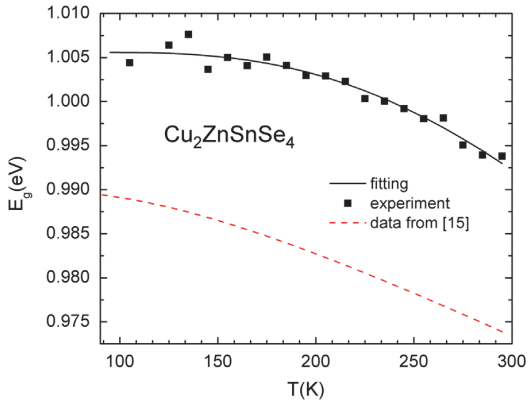

Fig. 2. Bandgap energy values found from ER fittings as a function of temperature. Solid curve is a fitting result with Eq. (2). The dashed curve represents the temperature dependence of bandgap energy of CZTSe according to data from ref. [15].

the $E_g(T)$ values using Eq. (2) with the fitting parameters E_g (0)=1.006±0.001 eV, S=2.0±0.6 and $\langle\hbar\omega\rangle$=85±13 meV. The overall shift of E_g is only about 26 meV from room temperature to T=0 K. Somewhat greater shift was found by Choi et al. [15], see Fig. 2.

4. Conclusion

In conclusion, temperature dependent ER measurements (T=100–300 K) were performed with CZTSe solar cell. All ER spectra were fitted using Aspnes third derivative functional form. High values of the broadening parameter Γ are explained by the high concentration of charged defects and spatial fluctuations of the bandgap energy caused by the presence of both ordered and disordered structures and/or different defect clusters in CZTSe. Temperature dependence of the bandgap energy of CZTSe was determined. The overall shift of the bandgap energy was found to be only about 26 meV from room temperature to T=0 K.

Q2 Uncited reference

[21].

Acknowledgment

Q3 This work was supported by the Estonian Science Foundation Grant ETF 9369, by the institutional research funding IUT 19-28 of the Estonian Ministry of Education and Research, Estonian Centre of Excellence in Research, Project TK117, by Estonian Material Technology Programme, Q4 Project AR12128 and by FP7 project CHEETAH, EC Grant agreement no. 609788, by project KESTCELLS Q5 (FP7-PEOPLE-2012-ITN-316488) and by European Regional Development Funds (ERDF, FEDER Programa Competitivitat de Catalunya 2007–2013). Authors from IREC and the University of Barcelona belong to the M-2E (Electronic Materials for Energy) Consolidated Research Group and the XaRMAE Network of Excellence on Materials for Energy of the “Generalitat de Catalunya”. E.S. thanks the Government of Spain for the “Ramon y Cajal” fellowship (RYC-2011-09212).

References

[1] W. Wang, M.T. Winkler, O. Gunawan, T. Gokmen, T.K. Todorov, Y. Zhu, D.B. Mitzi, Adv. Energy Mater. 4 (2014) 1301465.
[2] Y.S. Lee, T. Gershon, O. Gunawan, T.K. Todorov, T. Gokmen, Y. Virgus, S. Guha, Adv. Energy Mater. 12 (2014) 1401372.
[3] S. Schorr, Sol. Energy Mater. Sol. Cells 95 (2011) 1482–1488.
[4] J.S. Scragg, L. Choubrac, A. Lafond, T. Ericson, C. Platzer-Björkman, Appl. Phys. Lett. 104 (2014) 041911.
[5] D. Huang, C. Persson, Thin Solid Films 535 (2013) 265–269.
[6] S. Chen, A. Walsh, X.-G. Gong, S.-H. Wei, Adv. Mater. 25 (2013) 1522–1539.
[7] M. Grossberg, J. Krustok, J. Raudoja, T. Raadik, Appl. Phys. Lett. 101 (2012) 102102.
[8] C. Krämmer, C. Huber, C. Zimmermann, M. Lang, T. Schnabel, T. Abzieher, E. Ahlswede, H. Kalt, M. Hetterich, Appl. Phys. Lett. 105 (2014) 262104.
[9] G. Rey, A. Redinger, J. Sendler, T.P. Weiss, M. Thevenin, M. Guennou, B. El Adib, S. Siebentritt, Appl. Phys. Lett. 105 (2014) 112106.
[10] M. Grossberg, J. Krustok, T. Raadik, M. Kauk-Kuusik, J. Raudoja, Curr. Appl. Phys. 14 (2014) 1424–1427.
[11] F. Luckert, D.I. Hamilton, M.V. Yakushev, N.S. Beattie, G. Zoppi, M. Moynihan, I. Forbes, A.V. Karotki, A.V. Mudryi, M. Grossberg, J. Krustok, R.W. Martin, Appl. Phys. Lett. 99 (2011) 062104.
[12] M. Grossberg, J. Krustok, J. Raudoja, K. Timmo, M. Altosaar, T. Raadik., Thin Solid Films 519 (2011) 7403–7406.
[13] M. Grossberg, P. Salu, J. Raudoja, J. Krustok, J. Photon Energy 3 (2013) 030599.
[14] J. Krustok, R. Josepson, T. Raadik, M. Danilson, Physica B 405 (2010) 3186–3189.
[15] S.G. Choi, T.J. Kim, S.Y. Hwang, J. Li, C. Persson, Y.D. Kim, S.-H. Wei, I.L. Repins, Sol. Energy Mater. Sol. Cells 130 (2014) 375–379.
[16] D.E. Aspnes, Surf. Sci. 37 (1973) 418–442.
[17] K.P. O'Donnell, X. Chen, Appl. Phys. Lett. 58 (1991) 2924–2926.
[18] T. Raadik, J. Krustok, R. Josepson, J. Hiie, T. Potlog, N. Spalatu, Thin Solid Films 535 (2013) 279–282.
[19] M. Grossberg, J. Krustok, A. Jagomägi, M. Leon, E. Arushanov, A. Nateprov, I. Bodnar, Thin Solid Films 515 (2007) 6204–6207.
[20] S. López-Marino, Y. Sánchez, M. Placidi, A. Fairbrother, M. Espindola-Rodríguez, X. Fontané, V. Izquierdo-Roca, J. López-García, L. Calvo-Barrio, A. Pérez-Rodríguez, E. Saucedo, Chem.: Eur. J 19 (2013) 14814–14822.
[21] M. Neuschitzer, Y. Sanchez, S. López-Marino, H. Xie, A. Fairbrother, M. Placidi, S. Haass, V. Izquierdo-Roca, A. Perez-Rodriguez, E. Saucedo, Prog. Photovolt. Res. Appl. (2015), http://dx.doi.org/10.1002/pip.2589. Q6
[22] M. Grossberg, T. Raadik, J. Raudoja, J. Krustok, Curr. Appl. Phys. 14 (2014) 447–450.
[23] T.P. Weiss, A. Redinger, J. Luckas, M. Mousel, S. Siebentritt, Appl. Phys. Lett. 102 (2013) 202105.
[24] A. Fairbrother, M. Dimitrievska, Y. Sanchez, V. Izquierdo-Roca, A. Perez-Rodrguez, E. Saucedo, J. Mater. Chem. A 3 (2015) 9451–9455.

Appendix B

Curriculum Vitae

Ees- ja perekonnanimi	Taavi Raadik
Sünniaeg ja -koht	14. september 1983, Pärnu
E-post	taavi.raadik@ttu.ee
Haridus	2009- ... Tallinna Tehnikaülikool, doktorantuur, keemia- ja materjalitehnoloogia õppekava.
	2007-2009 Tallinna Tehnikaülikool, loodusteaduse magister, tehnilise füüsika õppekava.
	2002-2007 Tallinna Tehnikaülikool, loodusteaduse bakalaureus, tehnilise füüsika õppekava.
	2002-2003 Pärnu Üksik-jalaväepataljon, ajateenistus.
	1999-2002 Pärnu Koidula gümnaasium, keskharidus.
Teenistuskäik	2013 - ... Tallinna Tehnikaülikool, Keemia ja Materjaliteaduse instituut, nooremteadur.
	2012 - ... Sisekaitse Akadeemia, koosseisuväline lektor.
	2007-2011 Tallinna Tehnikaülikool, Keemia ja Materjaliteaduse instituut, insener.
	2006 – 2007 Testhouse OÜ, tarkvara testija.
Täiendõpe	2012-2014 TÜ ja TTÜ Doktorikool "Funktsionaalsed materjalid ja tehnoloogiad".

	November 2013 Helmholtz Zentrum Berlin, Tehnoloogia Instituut, külalisteadur , aeglahutus fotoluminestsents spektroskoopia meetodid. September 2012 Quantsol 2012 International Summer Shool on Photovoltaic, Hirschegg, Austria.
Tunnustused	2013, Eesti Üliõpilaste Toetusfond USAs stipendium. 2012, TTÜ Arengufondi Riigi Kinnisvara stipendium. 2010, World Federation of Scientists stipendium.
Kaitstud lõputööd	„ ZnO nanovarraste fotoluminestsentskiirguse uuringud “, magistritöö, juhendaja Prof. Jüri Krustok. „ Kaksikühendi CdTe fotoluminestsentskiirguse uuringud “, bakalaureusetöö, juhendaja Prof. Jüri Krustok.

Appendix B

Curriculum Vitae

First name and surname	Taavi Raadik
Date and place of birth	14 September 1983, Pärnu
E-mail	taavi.raadik@ttu.ee
Education	2009- ... Tallinn University of Technology, doctoral studies, Chemical and Materials Technology curriculum
	2007-2009 Tallinn University of Technology, Master of Science in Natural Sciences (Applied Physics), Engineering Physics curriculum
	2002-2007 Tallinn University of Technology, Bachelor of Science in Natural Sciences , Engineering Physics curriculum
	2002-2003 Estonian Defence Forces, Pärnu Single Infantry Battalion, military service
	1999-2002 Pärnu Koidula gymnasium, secondary education
Employment	2013 - ... Tallinn University of Technology, Department of Materials Science, early stage researcher
	2012 - ... Internal Defence Academy , external lecturer
	2007-2011 Tallinn University of Technology, Department of Materials Science, engineer
	2006 – 2007 Testhouse OÜ, software test engineer
Training	2012-2014 TU and TUT Graduate school “Functional materials and technologies “

	November 2013, Helmholtz Zentrum Berlin, Institute of Technology, visiting researcher, Time resolved PL methods
	September 2012, Quantsol 2012 International Summer School on Photovoltaic, Hirschegg, Austria
Recognitions	2013, Estonian Students´ Fund USA scholarship
	2012, TUT Development Foundation RKAS scholarship
	2010, World Federation of Scientists stipend
Defended dissertations	”Study of photoluminescence properties of binary compound ZnO nanorods“, master´s thesis, supervisor Prof. Jüri Krustok
	”Study of photoluminescence properties of binary compound CdTe“, bachelor´s thesis, supervisor Prof. Jüri Krustok

List of publications

1. Krustok J.; **Raadik T.**; Grossberg M.; Giraldo S.; Neuschitzer M.; López- Marino S.; Saucedo E. (2015). Temperature dependent electroreflectance study of $Cu_2ZnSnSe_4$ solar cells. Materials Science in Semiconductor Processing, (in press).

2. Grossberg, M.; Timmo, K.; **Raadik, T**.; Kärber, E.; Mikli, V.; Krustok, J. (2015). Study of structural and optoelectronic properties of $Cu_2Zn(Sn_{1-x}Ge_x)Se4$ (x = 0 to 1) alloy compounds. Thin Solid Films, 582, 176-179.

3. Yakushev, M.V.; Maiello, P.; **Raadik, T**.; Shaw, M.J.; Edwards, P.R.; Krustok, J.; Mudryi, A.V.; Forbes, I.; Martin, R.W. (2014). Investigation of the Structural, Optical and Electrical Properties of Cu_3BiS_3 Semiconducting Thin Films. Energy Procedia, 60, 166 - 172.

4. Spalatu, N.; Hiie, J.; Mikli, V.; Krunks, M.; Valdna, V.; Maticiuc, N.; **Raadik, T.**; Caraman, M. (2014). Effect of $CdCl_2$ annealing treatment on structural and optoelectronic properties of close spaced sublimation CdTe/CdS thin film solar cells vs deposition conditions. Thin Solid Films 582, 128 - 133.

5. Grossberg, M.; Krustok, J.; **Raadik, T.**; Kauk-Kuusik, M.; Raudoja, J. (2014). Photoluminescence study of disordering in the cation sublattice of Cu_2ZnSnS_4. Current Applied Physics, 14(11), 1424 - 1427.

6. Yakushev, M.V.; Maiello, P; **Raadik, T**; Shaw, M.J.; Edwards, P.R.; Krustok, J.; Mudryi, A.V.; Forbes, I.; Martin, R.W. (2014). Electronic and structural characterisation of Cu_3BiS_3 thin films for the absorber layer of sustainable photovoltaics. Thin Solid Films, 562, 195 - 199.

7. Spalatu, N.; Hiie, J.; Mikli, V.; Valdna, V.; Krunks, M.; Maticiuc, N.; **Raadik, T.**; Caraman, M. (2014). Effect of $CdCl_2$ vapor phase pretreatment annealing on the properties of CSS CdS and CdTe/CdS thin film solar cells. In: EMRS-2014 Spring Meeting, Lilli, France - May 26-30, Program and Book of Abstracts, Symp. A - Thin film chalcogenide photovoltaic materials: EMRS-2014 Spring Meeting, Lilli, France - May 26-30. (Eds.)European Materials Research Society, 17.

8. Grossberg, M.; **Raadik, T.**; Raudoja, J.; Krustok, J. (2014). Photoluminescence study of defect clusters in Cu_2ZnSnS_4 polycrystals. Current Applied Physics, 14(3), 447 - 450.

9. Bogatov, A.; Podgursky, V.; **Raadik, T.**; Kamjula, A. R.; Hantschel, T.; Tsigkourakos, M.; Kulu, P. (2014). Investigation of morphology changes on nanocrystalline diamond film surfaces during reciprocating sliding against Si_3N_4 balls. D. Loca (Eds.). Engineering Materials & Tribology XXII (126 - 129).Trans Tech Publications Ltd.

10. Iljina, J.; Zhang, R.; Ganchev, M.; **Raadik, T.**; Volobujeva, O.; Altosaar, M.; Traksmaa, R.; Mellikov, E. (2013). Formation of Cu_2ZnSnS_4 absorber layers for solar cells by electrodeposition-annealing route. Thin Solid Films, 537(30), 85 - 89.

11. Ganchev, M.; Loorits, M.; Revathi, N.; **Raadik, T.**; Raudoja, J.; Grossberg, M.; Mellikov, E.; Volobujeva, O. (2013). Structural and compositional properties of CZTS thin films formed by rapid thermal annealing of electrodeposited layers. Journal of Crystal Growth, 380, 236 - 240.

12. Timmo, K.; Kauk-Kuusik, M.; Altosaar, M.; Raudoja, J.; **Raadik, T.**; Grossberg, M.; Varema, T.; Pilvet, M.; Leinemann, I.; Volobujeva, O.; Mellikov, E. (2013). NOVEL Cu_2CdSnS_4 AND $Cu_2ZnGeSe_4$ ABSORBER MATERIALS FOR MONOGRAIN LAYER SOLAR CELL APPLICATION. EU PVSEC 2013, Pariis, Prantsusmaa 30.sept.-04.okt. 2013. Wiley-Blackwell, 2385 - 2388.

13. **Raadik, T.**; Grossberg, M.; Raudoja, J.; Traksmaa, R.; Krustok, J. (2013). Temperature-dependent photoreflectance of SnS crystals. Journal of Physics and Chemistry of Solids, 74(12), 1683 - 1685.

14. Bereznev, S.; Adhikari, N.; Kois, J.; **Raadik, T.**; Traksmaa, R.; Volobujeva, O.; Kouhiisfahani, E.; Öpik, A. (2013). One-source PVD of n-$CuIn_5Se_8$ photoabsorber films for hybrid solar cells. Solar Energy, 94, 202 - 208.

15. **Raadik, T.**; Krustok, J.; Josepson, R.; Hiie, J.; Potlog, T.; Spalatu, N. (2013). Temperature dependent electroreflectance study of CdTe solar cells. Thin Solid Films, 535, 279 - 282.

16. Maticiuc, N.; Hiie, J.; **Raadik, T.**; Graf, A.; Gavrilov, A. (2013). The role of Cl in the chemical bath on the properties of CdS thin films. Thin Solid Films, 535, 184 - 187.

17. Iljina, J.; Volobujeva, O.; **Raadik, T.**; Revathi, N.; Raudoja, J.; Loorits, M.; Traksmaa, R.; Mellikov, E. (2013). Selenisation of sequentially electrodeposited Cu-Zn and Sn precursor layers. Thin Solid Films, 535, 14 - 17.

18. Bollero, A; Kaupmees, L; **Raadik, T**; Grossberg, M; Fernandez, S. (2012). Thermal stability of sputtered Mo/polyimide films and formation of $MoSe_2$ and MoS_2 layers for application in flexible $Cu(In,Ga)(Se,S)_2$ based solar cells. Thin Solid Films, 520(12), 4163 - 4168.

19. Volobujeva, O.; Mellikov, E.; Bereznev, S.; Raudoja, J.; Otto, K.; Pilvet, M.; **Raadik, T.** (2012). $Cu_2ZnSnSe_4$ thin films by selenization of stacked binaries. In: E-MRS Spring Meeting 2012 - Symposium B, Program and Abstract Book, 2012: E-MRS Spring Meeting 2012, Strasbourg, France, May 14-18, 2012. (Eds.)EMRS. Strasbourg, France, 20.

20. Adhikari, N.; Bereznev, S.; Volobujeva, O.; **Raadik, T.**; Traksmaa, R.; Öpik, A. (2012). PVD of highly photosensitive n-$CuIn_5Se_8$ films for hybrid PV structures. In: Progress in Applied Surface, Interface and Thin Film Science 2012, Program and Book of Abstracts: Progress in Applied Surface, Interface and Thin Film Science 2012, Florence, Italy, June 14-19. 2012. Florence, Italy, 83.

21. Adhikari, N.; Bereznev, S.; Kois, J.; Volobujeva, O.; **Raadik, T.**; Traksmaa, R.; Dahal, R.; Tverjanovich, A.; Öpik, A. (2012). PVD OF n-$CuIn_5Se_8$ PHOTOABSORBER FILMS FOR HYBRID SOLAR CELLS. In: Baltic Polymer Symposium 2012, Liepaja, Latvia, September 19-22, 2012, Programme and Proceedings: Baltic Polymer Symposium 2012, Liepaja, Latvia, September 19-22, 2012. (Eds.)Riga Technical University. Riga, Latvia.

22. Adhikari, N.; Bereznev, S.; Kois, J.; Volobujeva, O.; **Raadik, T.**; Traksmaa, R.; Tverjanovich, A.; Öpik, A. (2012). PVD of n-$CuIn_3Se_5$ photoabsorber films. E. Hristoforou, D.S. Vlachos (Eds.). Materials and Applications for Sensors and Transducers (339 - 342). Trans Tech Publications Ltd.

23. Grossberg, M.; Krustok, J.; Raudoja, J.; **Raadik, T.** (2012). The role of structural properties on deep defect states in Cu_2ZnSnS_4 studied by photoluminescence spectroscopy. Applied Physics Letters, 101(102102), 102102-1-2.

24. Kaupmees, L.; Altosaar, M.; Volobujeva, O.; **Raadik, T.**; Grossberg, M.; Danilson, M.; Mellikov, E.; Barvinschi, P. (2012). Isothermal and two-temperature-zone selenization of Mo layers. Advances in Materials Science and Engineering, 2012, Article ID 345762.

25. Adhikari, N.; Bereznev, S.; Laes, K.; Kois, J.; Volobujeva, O.; **Raadik, T.**; Traksmaa, R.; Dahal, R.; Öpik, A. (2011). PVD OF n-$CuIn_5Se_8$ PHOTOABSORBER FILMS FOR HYBRID POLYMER SOLAR CELLS. In: Baltic Polymer Symposium 2011, Pärnu, Estonia, September 21-24, 2011, Program and Abstracts: Baltic Polymer Symposium 2011, Pärnu, Estonia, September 21-24, 2011. (Eds.)Tallinn University of Technology, Tallinn, 23.

26. Adhikari, N.; Bereznev, S.; Kois, J.; Volobujeva, O.; **Raadik, T.**; Traksmaa, R.; Tverjanovich, A.; Öpik, A. (2011). PVD of n-$CuIn_3Se_5$ Photoabsorber Films. In: Abstracts Book: International Conference on Materials and Applications for Sensors and Transducers, May 13-17, 2011, Kos Island, Greece. (Eds.)National Technical University of Athens. Athens, 105.

27. Potlog, T.; Spalatu, N.; Fedorov, V.; Maticiuc, N.; Antoniuc, C.; Hiie, J.; **Raadik, T.**; Valdna, V. (2011). The performance of thin film solar cells employing photovoltaic ZnSe/CdTe, CdS/CdTe and ZnTe/CdTe heterojunctions. In: Photovoltaic Specialists Conference (PVSC), 2011 37th IEEE: Photovoltaic Specialists Conference (PVSC), 2011 37th IEEE, Seattle, WA, USA, 19-24 June 2011. Seattle, WA, USA: IEEE, 001365 - 001370.

28. Kask, E.; **Raadik, T.**; Grossberg, M.; Josepson, R.; Krustok, J. (2011). Deep defects in Cu_2ZnSnS_4 monograin solar cells. Energy Procedia, 10, 261 - 265.

29. Ganchev, M.; Iljina, J.; Kaupmees, L.; **Raadik, T.** ; Volobujeva, O.; Mere, A.; Altosaar, M.; Raudoja, J.; Mellikov, E. (2011). Phase composition of selenized $Cu_2ZnSnSe_4$ thin films determined by X-ray diffraction and Raman spectroscopy. Thin Solid Films, 519(21), 7394 - 7398.

30. Valdna, V.; Grossberg, M.; Hiie, J.; Kallavus, U.; Mikli, V.; **Raadik, T.**; Traksmaa, R.; Viljus, M. (2011). ZnCdSeTe Semiconductor Compounds: Preparation and Properties. In: Symposium U – Nuclear Radiation Detection Materials : MRS 2011 Spring Meeting, San Francisco, CA, April 25-29, 2011. (Eds.)Michael Fiederle. Cambridge University Press, (MRS Proceedings; 1341), 07 - 15.

31. Bereznev, S.; Adhikari, N.; Kois, J.; Volobujeva, O.; Laes, K.; Traksmaa, R.; **Raadik, T.**; Öpik, A. (2011). Hübriidsetes fototundlikes struktuurides rakendavate n-$CuIn_3Se_5$ fotoabsorberkilede valmistamine kõrgvaakumaurustamise meetodil. In: XXXII Eesti keemiapäevad :

teaduskonverentsi teesid = 32th Estonian Chemistry Days : abstracts of scientific conference : (Eds.)Eesti Keemia Selts.Tartu: Tartu Ülikooli Kirjastus, 15.

32. Grossberg, M.; Krustok, J.; Raudoja, J.; Timmo, K.; Altosaar, M.; **Raadik, T.** (2011). Photoluminescence and Raman study of $Cu_2ZnSn(Se_xS_{1-x})_4$ monograins for photovoltaic applications. Thin Solid Films, 519(21), 7403 - 7406.

33. Kärber, E.; **Raadik, T.**; Dedova, T.; Krustok, J.; Mere, A.; Mikli, V.; Krunks, M. (2011). Photoluminescence of spray pyrolysis deposited ZnO nanorods. Nanoscale Research Letters, 6(359/April), 1 - 7.

34. **Raadik, T**; Krustok, J; Yakushev, M, V. (2011). Photoreflectance study of $AgGaTe_2$ single crystals. Physica B: Condensed Matter, 406(3), 418 - 420.

35. Maticiuc, N.; Potlog, T.; Hiie, J.; Mikli, V.; Poldme, N.; **Raadik, T.**; Valdna, V.; Mere, A.; Gavrilov, A.; Quinci, F.; Lughi, V.; Sergo, V. (2010). Structural changes in chemically deposited CdS: effect of thermal annealing. Moldavian Journal of the Physical Sciences, 9(3 - 4), 275 - 279.

36. Adhikari, N.; Bereznev, S.; Laes, K.; Kois, J.; Volobujeva, O.; **Raadik, T.**; Traksmaa, R.; Tverjanovich, A.; Öpik, A. (2010). High vacuum evaporation of n-$CuIn_3Se_5$ photoabsorber films for hybrid PV structures with conductive polymers. In: Baltic Polymer Symposium 2010, September 8-11, 2010, Palanga, Lithuania, Programme and Abstracts: Baltic Polymer Symposium 2010, September 8-11, 2010, Palanga, Lithuania, 124.

37. Volobujeva, O.; Mellikov, E.; Bereznev, S.; **Raadik, T.**; Raudoja, J. (2010). Microscopic and Spectroscopic Study of Formation of $Cu_2ZnSnSe_4$ Thin Films from Binary Containing Precursors. International Microscopy Congress (IMC17) proceedings, september 19-24,2010, Rio, Brazil. Elsevier, xx - xx.

38. Laes, K.; Bereznev, S.; Land, R.; Tverjanovich, A.; Volobujeva, O.; Traksmaa, R.; **Raadik, T.**; Öpik, A. (2010). The impedance spectroscopy of $CuIn_3Se_5$ photoabsorber films prepared by high vacuum evaporation technique. Energy Procedia, 2(1), 119 - 131.

39. Volobujeva, O.; Mellikov, E.; Bereznev, S.; Raudoja, J.; Öpik, A; **Raadik, T.** (2010). $Cu_2ZnSnSe_4$ thin films produced by selenization of

Cu-Zn-Sn containing precursor films. George G. Wicks, Jack Simon, Ragaiy Zidan, Edgar Lara-Curzio, Thad Adams, Jose Zayas, Abhi Karkamkar (Eds.). Materials Challenges in Alternative and Renewable Energy (257 - 263).The American Ceramic Society, Wiley-Blackwell

40. Krustok, J.; Josepson, R.; **Raadik, T.**; Danilson, M. (2010). Potential fluctuations in $Cu_2ZnSnSe_4$ solar cells studied by temperature dependence of quantum efficiency curves. Physica B: Condensed Matter, 405(15), 3186 - 3189.

41. Põldme, N.; Hiie, J.; Mikli, V.; **Raadik, T.**; Valdna, V.; Mere, A.; Gavrilov, A.; Maticiuc, N.; Potlog, T.; Quinci, F.; Lughi, V.; Sergo, V. (2010). Keemiliselt sadestatud kaadmiumsulfiidi kilede lõõmutamisel toimuvad struktuursed muutused. In: Abstracts of Scientific Conference: XXXI Eesti Keemiapäevad, Tallinn, 28.04.2010. Eesti Keemia Selts, 65.

42. Bollero, A.; Grossberg, M.; **Raadik, T.**; Trigo, J. F.; Herrero, J.; Gutiérrez, M T. (2009). Growth of Cu-rich/poor $CuInS_2$ thin films by the sequential modulated flux deposition technique. In: Thin-Film Compound Semiconductor Photovoltaics — 2009: 2009 MRS Spring Meeting, San Francisco USA,13-17.04.2009. (Eds.)A. Yamada, C. Heske, M. Contreras, M. Igalson, S.J.C. Irvine . Warrendale, PA, USA: Materials Research Society, (MRS Proceedings; 1165), 1165-M02-06.

43. Laes, K.; Bereznev, S.; Tverjanovich, A.; Traksmaa, R.; **Raadik, T.**; Öpik, A. (2009). Morphology, electrical and optical characterization of oriented $CuIn_3Se_5$ films prepared by high vacuum evaporation technique. In: 3rd Nordic PV Conference, Catalogue of Abstracts: 3rd Nordic PV Conference, 18-19 May 2009, Tallinn, Estonia. (Eds.)TTÜ. Tallinn, 14 - 15.

44. Hiie, J.; Quinci, F.; Lughi, V.; Sergo, V.; Valdna, V.; Mikli, V.; Kärber, E.; **Raadik, T.** (2009). Chlorine Doping of Cadmium Sulfide on the Example of CBD CdS. In: Thin-Film Compound Semiconductor Photovoltaics — 2009: 2009 MRS Spring Meeting, San Francisco USA,13-17.04.2009. (Eds.)A. Yamada, C. Heske, M. Contreras, M. Igalson, S.J.C. Irvine. Warrendale, PA, USA: Materials Research Society, (MRS Proceedings; 1165), 1165-M08-17.

DISSERTATIONS DEFENDED AT
TALLINN UNIVERSITY OF TECHNOLOGY ON
NATURAL AND EXACT SCIENCES

1. **Olav Kongas**. Nonlinear Dynamics in Modeling Cardiac Arrhytmias. 1998.

2. **Kalju Vanatalu**. Optimization of Processes of Microbial Biosynthesis of Isotopically Labeled Biomolecules and Their Complexes. 1999.

3. **Ahto Buldas**. An Algebraic Approach to the Structure of Graphs. 1999.

4. **Monika Drews**. A Metabolic Study of Insect Cells in Batch and Continuous Culture: Application of Chemostat and Turbidostat to the Production of Recombinant Proteins. 1999.

5. **Eola Valdre**. Endothelial-Specific Regulation of Vessel Formation: Role of Receptor Tyrosine Kinases. 2000.

6. **Kalju Lott**. Doping and Defect Thermodynamic Equilibrium in ZnS. 2000.

7. **Reet Koljak**. Novel Fatty Acid Dioxygenases from the Corals *Plexaura homomalla* and *Gersemia fruticosa.* 2001.

8. **Anne Paju**. Asymmetric oxidation of Prochiral and Racemic Ketones by Using Sharpless Catalyst. 2001.

9. **Marko Vendelin**. Cardiac Mechanoenergetics *in silico*. 2001.

10. **Pearu Peterson**. Multi-Soliton Interactions and the Inverse Problem of Wave Crest. 2001.

11. **Anne Menert**. Microcalorimetry of Anaerobic Digestion. 2001.

12. **Toomas Tiivel**. The Role of the Mitochondrial Outer Membrane in *in vivo* Regulation of Respiration in Normal Heart and Skeletal Muscle Cell. 2002.

13. **Olle Hints**. Ordovician Scolecodonts of Estonia and Neighbouring Areas: Taxonomy, Distribution, Palaeoecology, and Application. 2002.

14. **Jaak Nõlvak**. Chitinozoan Biostratigrapy in the Ordovician of Baltoscandia. 2002.

15. **Liivi Kluge**. On Algebraic Structure of Pre-Operad. 2002.

16. **Jaanus Lass**. Biosignal Interpretation: Study of Cardiac Arrhytmias and Electromagnetic Field Effects on Human Nervous System. 2002.

17. **Janek Peterson**. Synthesis, Structural Characterization and Modification of PAMAM Dendrimers. 2002.

18. **Merike Vaher**. Room Temperature Ionic Liquids as Background Electrolyte Additives in Capillary Electrophoresis. 2002.

19. **Valdek Mikli**. Electron Microscopy and Image Analysis Study of Powdered Hardmetal Materials and Optoelectronic Thin Films. 2003.

20. **Mart Viljus**. The Microstructure and Properties of Fine-Grained Cermets. 2003.

21. **Signe Kask**. Identification and Characterization of Dairy-Related *Lactobacillus.* 2003

22. **Tiiu-Mai Laht**. Influence of Microstructure of the Curd on Enzymatic and Microbiological Processes in Swiss-Type Cheese. 2003.

23. **Anne Kuusksalu**. 2–5A Synthetase in the Marine Sponge *Geodia cydonium*. 2003.

24. **Sergei Bereznev**. Solar Cells Based on Polycristalline Copper-Indium Chalcogenides and Conductive Polymers. 2003.

25. **Kadri Kriis**. Asymmetric Synthesis of C_2-Symmetric Bimorpholines and Their Application as Chiral Ligands in the Transfer Hydrogenation of Aromatic Ketones. 2004.

26. **Jekaterina Reut**. Polypyrrole Coatings on Conducting and Insulating Substracts. 2004.

27. **Sven Nõmm**. Realization and Identification of Discrete-Time Nonlinear Systems. 2004.

28. **Olga Kijatkina**. Deposition of Copper Indium Disulphide Films by Chemical Spray Pyrolysis. 2004.

29. **Gert Tamberg**. On Sampling Operators Defined by Rogosinski, Hann and Blackman Windows. 2004.

30. **Monika Übner**. Interaction of Humic Substances with Metal Cations. 2004.

31. **Kaarel Adamberg**. Growth Characteristics of Non-Starter Lactic Acid Bacteria from Cheese. 2004.

32. **Imre Vallikivi**. Lipase-Catalysed Reactions of Prostaglandins. 2004.

33. **Merike Peld**. Substituted Apatites as Sorbents for Heavy Metals. 2005.

34. **Vitali Syritski**. Study of Synthesis and Redox Switching of Polypyrrole and Poly(3,4-ethylenedioxythiophene) by Using *in-situ* Techniques. 2004.

35. **Lee Põllumaa**. Evaluation of Ecotoxicological Effects Related to Oil Shale Industry. 2004.

36. **Riina Aav**. Synthesis of 9,11-Secosterols Intermediates. 2005.

37. **Andres Braunbrück**. Wave Interaction in Weakly Inhomogeneous Materials. 2005.

38. **Robert Kitt**. Generalised Scale-Invariance in Financial Time Series. 2005.

39. **Juss Pavelson**. Mesoscale Physical Processes and the Related Impact on the Summer Nutrient Fields and Phytoplankton Blooms in the Western Gulf of Finland. 2005.

40. **Olari Ilison**. Solitons and Solitary Waves in Media with Higher Order Dispersive and Nonlinear Effects. 2005.

41. **Maksim Säkki**. Intermittency and Long-Range Structurization of Heart Rate. 2005.

42. **Enli Kiipli**. Modelling Seawater Chemistry of the East Baltic Basin in the Late Ordovician–Early Silurian. 2005.

43. **Igor Golovtsov**. Modification of Conductive Properties and Processability of Polyparaphenylene, Polypyrrole and polyaniline. 2005.

44. **Katrin Laos**. Interaction Between Furcellaran and the Globular Proteins (Bovine Serum Albumin β-Lactoglobulin). 2005.

45. **Arvo Mere**. Structural and Electrical Properties of Spray Deposited Copper Indium Disulphide Films for Solar Cells. 2006.

46. **Sille Ehala**. Development and Application of Various On- and Off-Line Analytical Methods for the Analysis of Bioactive Compounds. 2006.

47. **Maria Kulp**. Capillary Electrophoretic Monitoring of Biochemical Reaction Kinetics. 2006.

48. **Anu Aaspõllu.** Proteinases from *Vipera lebetina* Snake Venom Affecting Hemostasis. 2006.

49. **Lyudmila Chekulayeva**. Photosensitized Inactivation of Tumor Cells by Porphyrins and Chlorins. 2006.

50. **Merle Uudsemaa**. Quantum-Chemical Modeling of Solvated First Row Transition Metal Ions. 2006.

51. **Tagli Pitsi**. Nutrition Situation of Pre-School Children in Estonia from 1995 to 2004. 2006.

52. **Angela Ivask**. Luminescent Recombinant Sensor Bacteria for the Analysis of Bioavailable Heavy Metals. 2006.

53. **Tiina Lõugas**. Study on Physico-Chemical Properties and Some Bioactive Compounds of Sea Buckthorn (*Hippophae rhamnoides* L.). 2006.

54. **Kaja Kasemets**. Effect of Changing Environmental Conditions on the Fermentative Growth of *Saccharomyces cerevisae* S288C: Auxo-accelerostat Study. 2006.

55. **Ildar Nisamedtinov**. Application of ^{13}C and Fluorescence Labeling in Metabolic Studies of *Saccharomyces* spp. 2006.

56. **Alar Leibak**. On Additive Generalisation of Voronoï's Theory of Perfect Forms over Algebraic Number Fields. 2006.

57. **Andri Jagomägi**. Photoluminescence of Chalcopyrite Tellurides. 2006.

58. **Tõnu Martma**. Application of Carbon Isotopes to the Study of the Ordovician and Silurian of the Baltic. 2006.

59. **Marit Kauk**. Chemical Composition of $CuInSe_2$ Monograin Powders for Solar Cell Application. 2006.

60. **Julia Kois**. Electrochemical Deposition of $CuInSe_2$ Thin Films for Photovoltaic Applications. 2006.

61. **Ilona Oja Açik**. Sol-Gel Deposition of Titanium Dioxide Films. 2007.

62. **Tiia Anmann**. Integrated and Organized Cellular Bioenergetic Systems in Heart and Brain. 2007.

63. **Katrin Trummal**. Purification, Characterization and Specificity Studies of Metalloproteinases from *Vipera lebetina* Snake Venom. 2007.

64. **Gennadi Lessin**. Biochemical Definition of Coastal Zone Using Numerical Modeling and Measurement Data. 2007.

65. **Enno Pais**. Inverse problems to determine non-homogeneous degenerate memory kernels in heat flow. 2007.

66. **Maria Borissova**. Capillary Electrophoresis on Alkylimidazolium Salts. 2007.

67. **Karin Valmsen**. Prostaglandin Synthesis in the Coral *Plexaura homomalla*: Control of Prostaglandin Stereochemistry at Carbon 15 by Cyclooxygenases. 2007.

68. **Kristjan Piirimäe**. Long-Term Changes of Nutrient Fluxes in the Drainage Basin of the Gulf of Finland – Application of the PolFlow Model. 2007.

69. **Tatjana Dedova**. Chemical Spray Pyrolysis Deposition of Zinc Sulfide Thin Films and Zinc Oxide Nanostructured Layers. 2007.

70. **Katrin Tomson**. Production of Labelled Recombinant Proteins in Fed-Batch Systems in *Escherichia coli*. 2007.

71. **Cecilia Sarmiento**. Suppressors of RNA Silencing in Plants. 2008.

72. **Vilja Mardla**. Inhibition of Platelet Aggregation with Combination of Antiplatelet Agents. 2008.

73. **Maie Bachmann**. Effect of Modulated Microwave Radiation on Human Resting Electroencephalographic Signal. 2008.

74. **Dan Hüvonen**. Terahertz Spectroscopy of Low-Dimensional Spin Systems. 2008.

75. **Ly Villo**. Stereoselective Chemoenzymatic Synthesis of Deoxy Sugar Esters Involving *Candida antarctica* Lipase B. 2008.

76. **Johan Anton**. Technology of Integrated Photoelasticity for Residual Stress Measurement in Glass Articles of Axisymmetric Shape. 2008.

77. **Olga Volobujeva**. SEM Study of Selenization of Different Thin Metallic Films. 2008.

78. **Artur Jõgi**. Synthesis of 4'-Substituted 2,3'-dideoxynucleoside Analogues. 2008.

79. **Mario Kadastik**. Doubly Charged Higgs Boson Decays and Implications on Neutrino Physics. 2008.

80. **Fernando Pérez-Caballero**. Carbon Aerogels from 5-Methylresorcinol-Formaldehyde Gels. 2008.

81. **Sirje Vaask**. The Comparability, Reproducibility and Validity of Estonian Food Consumption Surveys. 2008.

82. **Anna Menaker**. Electrosynthesized Conducting Polymers, Polypyrrole and Poly(3,4-ethylenedioxythiophene), for Molecular Imprinting. 2009.

83. **Lauri Ilison**. Solitons and Solitary Waves in Hierarchical Korteweg-de Vries Type Systems. 2009.

84. **Kaia Ernits**. Study of In_2S_3 and ZnS Thin Films Deposited by Ultrasonic Spray Pyrolysis and Chemical Deposition. 2009.

85. **Veljo Sinivee**. Portable Spectrometer for Ionizing Radiation "Gammamapper". 2009.

86. **Jüri Virkepu**. On Lagrange Formalism for Lie Theory and Operadic Harmonic Oscillator in Low Dimensions. 2009.

87. **Marko Piirsoo**. Deciphering Molecular Basis of Schwann Cell Development. 2009.

88. **Kati Helmja**. Determination of Phenolic Compounds and Their Antioxidative Capability in Plant Extracts. 2010.

89. **Merike Sõmera**. Sobemoviruses: Genomic Organization, Potential for Recombination and Necessity of P1 in Systemic Infection. 2010.

90. **Kristjan Laes**. Preparation and Impedance Spectroscopy of Hybrid Structures Based on $CuIn_3Se_5$ Photoabsorber. 2010.

91. **Kristin Lippur**. Asymmetric Synthesis of 2,2'-Bimorpholine and its 5,5'-Substituted Derivatives. 2010.

92. **Merike Luman**. Dialysis Dose and Nutrition Assessment by an Optical Method. 2010.

93. **Mihhail Berezovski**. Numerical Simulation of Wave Propagation in Heterogeneous and Microstructured Materials. 2010.

94. **Tamara Aid-Pavlidis**. Structure and Regulation of BDNF Gene. 2010.

95. **Olga Bragina**. The Role of Sonic Hedgehog Pathway in Neuro- and Tumorigenesis. 2010.

96. **Merle Randrüüt**. Wave Propagation in Microstructured Solids: Solitary and Periodic Waves. 2010.

97. **Marju Laars**. Asymmetric Organocatalytic Michael and Aldol Reactions Mediated by Cyclic Amines. 2010.

98. **Maarja Grossberg**. Optical Properties of Multinary Semiconductor Compounds for Photovoltaic Applications. 2010.

99. **Alla Maloverjan**. Vertebrate Homologues of Drosophila Fused Kinase and Their Role in Sonic Hedgehog Signalling Pathway. 2010.

100. **Priit Pruunsild**. Neuronal Activity-Dependent Transcription Factors and Regulation of Human *BDNF* Gene. 2010.

101. **Tatjana Knjazeva**. New Approaches in Capillary Electrophoresis for Separation and Study of Proteins. 2011.

102. **Atanas Katerski**. Chemical Composition of Sprayed Copper Indium Disulfide Films for Nanostructured Solar Cells. 2011.

103. **Kristi Timmo.** Formation of Properties of $CuInSe_2$ and $Cu_2ZnSn(S,Se)_4$ Monograin Powders Synthesized in Molten KI. 2011.
104. **Kert Tamm**. Wave Propagation and Interaction in Mindlin-Type Microstructured Solids: Numerical Simulation. 2011.
105. **Adrian Popp**. Ordovician Proetid Trilobites in Baltoscandia and Germany. 2011.
106. **Ove Pärn**. Sea Ice Deformation Events in the Gulf of Finland and This Impact on Shipping. 2011.
107. **Germo Väli**. Numerical Experiments on Matter Transport in the Baltic Sea. 2011.
108. **Andrus Seiman**. Point-of-Care Analyser Based on Capillary Electrophoresis. 2011.
109. **Olga Katargina**. Tick-Borne Pathogens Circulating in Estonia (Tick-Borne Encephalitis Virus, *Anaplasma phagocytophilum*, *Babesia* Species): Their Prevalence and Genetic Characterization. 2011.
110. **Ingrid Sumeri**. The Study of Probiotic Bacteria in Human Gastrointestinal Tract Simulator. 2011.
111. **Kairit Zovo**. Functional Characterization of Cellular Copper Proteome. 2011.
112. **Natalja Makarytsheva**. Analysis of Organic Species in Sediments and Soil by High Performance Separation Methods. 2011.
113. **Monika Mortimer**. Evaluation of the Biological Effects of Engineered Nanoparticles on Unicellular Pro- and Eukaryotic Organisms. 2011.
114. **Kersti Tepp**. Molecular System Bioenergetics of Cardiac Cells: Quantitative Analysis of Structure-Function Relationship. 2011.
115. **Anna-Liisa Peikolainen**. Organic Aerogels Based on 5-Methylresorcinol. 2011.
116. **Leeli Amon**. Palaeoecological Reconstruction of Late-Glacial Vegetation Dynamics in Eastern Baltic Area: A View Based on Plant Macrofossil Analysis. 2011.
117. **Tanel Peets**. Dispersion Analysis of Wave Motion in Microstructured Solids. 2011.
118. **Liina Kaupmees**. Selenization of Molybdenum as Contact Material in Solar Cells. 2011.
119. **Allan Olspert**. Properties of VPg and Coat Protein of Sobemoviruses. 2011.
120. **Kadri Koppel**. Food Category Appraisal Using Sensory Methods. 2011.
121. **Jelena Gorbatšova**. Development of Methods for CE Analysis of Plant Phenolics and Vitamins. 2011.
122. **Karin Viipsi**. Impact of EDTA and Humic Substances on the Removal of Cd and Zn from Aqueous Solutions by Apatite. 2012.
123. **David Schryer**. Metabolic Flux Analysis of Compartmentalized Systems Using Dynamic Isotopologue Modeling. 2012.
124. **Ardo Illaste**. Analysis of Molecular Movements in Cardiac Myocytes. 2012.
125. **Indrek Reile**. 3-Alkylcyclopentane-1,2-Diones in Asymmetric Oxidation and Alkylation Reactions. 2012.
126. **Tatjana Tamberg**. Some Classes of Finite 2-Groups and Their Endomorphism Semigroups. 2012.

127. **Taavi Liblik**. Variability of Thermohaline Structure in the Gulf of Finland in Summer. 2012.
128. **Priidik Lagemaa**. Operational Forecasting in Estonian Marine Waters. 2012.
129. **Andrei Errapart**. Photoelastic Tomography in Linear and Non-linear Approximation. 2012.
130. **Külliki Krabbi**. Biochemical Diagnosis of Classical Galactosemia and Mucopolysaccharidoses in Estonia. 2012.
131. **Kristel Kaseleht**. Identification of Aroma Compounds in Food using SPME-GC/MS and GC-Olfactometry. 2012.
132. **Kristel Kodar**. Immunoglobulin G Glycosylation Profiling in Patients with Gastric Cancer. 2012.
133. **Kai Rosin**. Solar Radiation and Wind as Agents of the Formation of the Radiation Regime in Water Bodies. 2012.
134. **Ann Tiiman**. Interactions of Alzheimer's Amyloid-Beta Peptides with Zn(II) and Cu(II) Ions. 2012.
135. **Olga Gavrilova**. Application and Elaboration of Accounting Approaches for Sustainable Development. 2012.
136. **Olesja Bondarenko**. Development of Bacterial Biosensors and Human Stem Cell-Based *In Vitro* Assays for the Toxicological Profiling of Synthetic Nanoparticles. 2012.
137. **Katri Muska**. Study of Composition and Thermal Treatments of Quaternary Compounds for Monograin Layer Solar Cells. 2012.
138. **Ranno Nahku**. Validation of Critical Factors for the Quantitative Characterization of Bacterial Physiology in Accelerostat Cultures. 2012.
139. **Petri-Jaan Lahtvee**. Quantitative Omics-level Analysis of Growth Rate Dependent Energy Metabolism in *Lactococcus lactis*. 2012.
140. **Kerti Orumets**. Molecular Mechanisms Controlling Intracellular Glutathione Levels in Baker's Yeast *Saccharomyces cerevisiae* and its Random Mutagenized Glutathione Over-Accumulating Isolate. 2012.
141. **Loreida Timberg**. Spice-Cured Sprats Ripening, Sensory Parameters Development, and Quality Indicators. 2012.
142. **Anna Mihhalevski**. Rye Sourdough Fermentation and Bread Stability. 2012.
143. **Liisa Arike**. Quantitative Proteomics of *Escherichia coli*: From Relative to Absolute Scale. 2012.
144. **Kairi Otto**. Deposition of In_2S_3 Thin Films by Chemical Spray Pyrolysis. 2012.
145. **Mari Sepp**. Functions of the Basic Helix-Loop-Helix Transcription Factor TCF4 in Health and Disease. 2012.
146. **Anna Suhhova**. Detection of the Effect of Weak Stressors on Human Resting Electroencephalographic Signal. 2012.
147. **Aram Kazarjan**. Development and Production of Extruded Food and Feed Products Containing Probiotic Microorganisms. 2012.
148. **Rivo Uiboupin**. Application of Remote Sensing Methods for the Investigation of Spatio-Temporal Variability of Sea Surface Temperature and Chlorophyll Fields in the Gulf of Finland. 2013.
149. **Tiina Kriščiunaite**. A Study of Milk Coagulability. 2013.

150. **Tuuli Levandi**. Comparative Study of Cereal Varieties by Analytical Separation Methods and Chemometrics. 2013.
151. **Natalja Kabanova**. Development of a Microcalorimetric Method for the Study of Fermentation Processes. 2013.
152. **Himani Khanduri**. Magnetic Properties of Functional Oxides. 2013.
153. **Julia Smirnova**. Investigation of Properties and Reaction Mechanisms of Redox-Active Proteins by ESI MS. 2013.
154. **Mervi Sepp**. Estimation of Diffusion Restrictions in Cardiomyocytes Using Kinetic Measurements. 2013.
155. **Kersti Jääger**. Differentiation and Heterogeneity of Mesenchymal Stem Cells. 2013.
156. **Victor Alari**. Multi-Scale Wind Wave Modeling in the Baltic Sea. 2013.
157. **Taavi Päll**. Studies of CD44 Hyaluronan Binding Domain as Novel Angiogenesis Inhibitor. 2013.
158. **Allan Niidu**. Synthesis of Cyclopentane and Tetrahydrofuran Derivatives. 2013.
159. **Julia Geller**. Detection and Genetic Characterization of *Borrelia* Species Circulating in Tick Population in Estonia. 2013.
160. **Irina Stulova**. The Effects of Milk Composition and Treatment on the Growth of Lactic Acid Bacteria. 2013.
161. **Jana Holmar**. Optical Method for Uric Acid Removal Assessment During Dialysis. 2013.
162. **Kerti Ausmees**. Synthesis of Heterobicyclo[3.2.0]heptane Derivatives *via* Multicomponent Cascade Reaction. 2013.
163. **Minna Varikmaa**. Structural and Functional Studies of Mitochondrial Respiration Regulation in Muscle Cells. 2013.
164. **Indrek Koppel**. Transcriptional Mechanisms of BDNF Gene Regulation. 2014.
165. **Kristjan Pilt**. Optical Pulse Wave Signal Analysis for Determination of Early Arterial Ageing in Diabetic Patients. 2014.
166. **Andres Anier**. Estimation of the Complexity of the Electroencephalogram for Brain Monitoring in Intensive Care. 2014.
167. **Toivo Kallaste**. Pyroclastic Sanidine in the Lower Palaeozoic Bentonites – A Tool for Regional Geological Correlations. 2014.
168. **Erki Kärber**. Properties of ZnO-nanorod/In_2S_3/$CuInS_2$ Solar Cell and the Constituent Layers Deposited by Chemical Spray Method. 2014.
169. **Julia Lehner**. Formation of Cu_2ZnSnS_4 and $Cu_2ZnSnSe_4$ by Chalcogenisation of Electrochemically Deposited Precursor Layers. 2014.
170. **Peep Pitk**. Protein- and Lipid-rich Solid Slaughterhouse Waste Anaerobic Co-digestion: Resource Analysis and Process Optimization. 2014.
171. **Kaspar Valgepea**. Absolute Quantitative Multi-omics Characterization of Specific Growth Rate-dependent Metabolism of *Escherichia coli*. 2014.
172. **Artur Noole**. Asymmetric Organocatalytic Synthesis of 3,3'-Disubstituted Oxindoles. 2014.
173. **Robert Tsanev**. Identification and Structure-Functional Characterisation of the Gene Transcriptional Repressor Domain of Human Gli Proteins. 2014.

174. **Dmitri Kartofelev**. Nonlinear Sound Generation Mechanisms in Musical Acoustic. 2014.
175. **Sigrid Hade**. GIS Applications in the Studies of the Palaeozoic Graptolite Argillite and Landscape Change. 2014.
176. **Agne Velthut-Meikas**. Ovarian Follicle as the Environment of Oocyte Maturation: The Role of Granulosa Cells and Follicular Fluid at Pre-Ovulatory Development. 2014.
177. **Kristel Hälvin**. Determination of B-group Vitamins in Food Using an LC-MS Stable Isotope Dilution Assay. 2014.
178. **Mailis Päri**. Characterization of the Oligoadenylate Synthetase Subgroup from Phylum Porifera. 2014.
179. **Jekaterina Kazantseva**. Alternative Splicing of *TAF4*: A Dynamic Switch between Distinct Cell Functions. 2014.
180. **Jaanus Suurväli**. Regulator of G Protein Signalling 16 (RGS16): Functions in Immunity and Genomic Location in an Ancient MHC-Related Evolutionarily Conserved Synteny Group. 2014.
181. **Ene Viiard**. Diversity and Stability of Lactic Acid Bacteria During Rye Sourdough Propagation. 2014.
182. **Kristella Hansen**. Prostaglandin Synthesis in Marine Arthropods and Red Algae. 2014.
183. **Helike Lõhelaid**. Allene Oxide Synthase-lipoxygenase Pathway in Coral Stress Response. 2015.
184. **Normunds Stivrinš**. Postglacial Environmental Conditions, Vegetation Succession and Human Impact in Latvia. 2015.
185. **Mary-Liis Kütt**. Identification and Characterization of Bioactive Peptides with Antimicrobial and Immunoregulating Properties Derived from Bovine Colostrum and Milk. 2015.